2006

# Wide Viewing Angle Liquid Crystal Displays

Qi Hong
*University of Central Florida*

# WIDE VIEWING ANGLE LIQUID CRYSTAL DISPLAYS

By

QI HONG
B.S. Nanjing University of Aerospace and Astronautics, 1992
M.S.E.E. University of Central Florida, 2002

A dissertation submitted in partial fulfillment of the requirements
for the degree of Doctor of Philosophy in Electrical Engineering
in the College of Engineering and Computer Science
at the University of Central Florida
Orlando, Florida

Fall Term
2006

Major Professors: Shin-Tson Wu
Thomas Xinzhang Wu

# ABSTRACT

In this dissertation, novel phase compensation technologies are applied to the designs of wide viewing angle and high transmittance liquid crystal displays. First, a design of wide viewing angle liquid crystal displays utilizing crossed linear polarizers is proposed. The designed multi-domain vertical-alignment liquid crystal display predicts superb contrast ratio over wide viewing angles. Next, to increase the bright state transmittance while maintain the high contrast ratio, wide viewing angle circular polarizers are developed. The produced states of polarization are very close to the ideal circular state of polarization over a wide range of incident angles within the visual spectrum. This guarantees not only high contrast ratio but also high and uniform transmittance.

Finally, to reduce the cost and improve the applicability of the broadband and wide-view circular polarizer, the device configuration of the broadband and wide-view circular polarizer is significantly simplified by the application of biaxial compensation films. The produced states of polarization remain close to the ideal circular polarization over a wide range of incident angles within the visual spectrum. With this circular polarizer, the presented wide-view liquid crystal display predicts high contrast ratio as well as high and uniform transmittance over wide viewing angles within the visual spectrum.

To my wife, my parents, and my brother

# ACKNOWLEDGMENTS

I would like to express my sincerest gratitude to my advisors, Prof. Shin-Tson Wu and Prof. Thomas X. Wu, for their patient guidance, inspiration, and support throughout my studies at the University of Central Florida. I believe that my future professional career and my personal life will benefit from my advisors, both of whom are diligent and knowledgeable researchers.

I would also like to sincerely thank my dissertation committee members Prof. Parveen F. Wahid, Prof. Donald C. Malocha, and Prof. M. G. "Jim" Moharam for evaluating my dissertation and for their invaluable suggestions.

Appreciations also go to all of my colleagues and friends, especially to Dr. Ruibo Lu, Dr. Yuhua Huang, Dr. Qiong-Hua Wang, Dr. Wing Kit Choi, Dr. Bounds Huang, Ying Zhou, Zhibing Ge, and Xiangyi Nie. I want to thank them for their invaluable suggestion and constant support.

This work was funded by TOPPOLY Optoelectronics (Taiwan) and CHI-MEI Optoelectronics (Taiwan). I sincerely appreciate their financial supports.

Last and forever, I am profoundly indebted to my parents and my brother, for their constant unwavering support and encouragement throughout my life. I am deeply indebted to my lovely wife for her understanding and patience during my graduate studies.

# TABLE OF CONTENTS

# LIST OF FIGURES

# CHAPTER ONE: INTRODUCTION

Liquid crystal is such a kind of material that it is strongly anisotropic in some properties and has a certain degree of fluidity [1-3]. The molecules of liquid crystal are aligned approximately parallel to each other in the neighborhood. The preferred direction of liquid crystal molecules in the neighborhood is called director. Liquid crystal directors reorient if an external applied voltage is greater than a certain value, which is called the threshold voltage. Because of its fluidity and the strong anisotropies in some electrical and optical properties, liquid crystal plays important roles in many applications, including display applications and non-display applications. Typical display applications include handheld electronics, cell phones, computer monitors, instrument monitors, televisions, and so on. Non-display applications include electrical tunable lenses, optical phase arrays, and otherwise. Currently display applications are the major applications of liquid crystal. The markets of liquid crystal displays are growing fast and steadily due to the improved performance and the reduced cost.

Liquid crystal displays are non-emissive display devices where each display pixel performs as a light modulator [1-3]. Figure 1.1 depicts the schematic diagram of a transmissive mode thin-film-transistor liquid crystal display (TFT-LCD). As Figure 1.1 illustrates, to render full color images, each display pixel is divided into Red, Green, and Blue (RGB) sub-pixels, in which the red, green, and blue spectra are produced from the white color backlight by the corresponding red, green, and blue color filters, respectively.

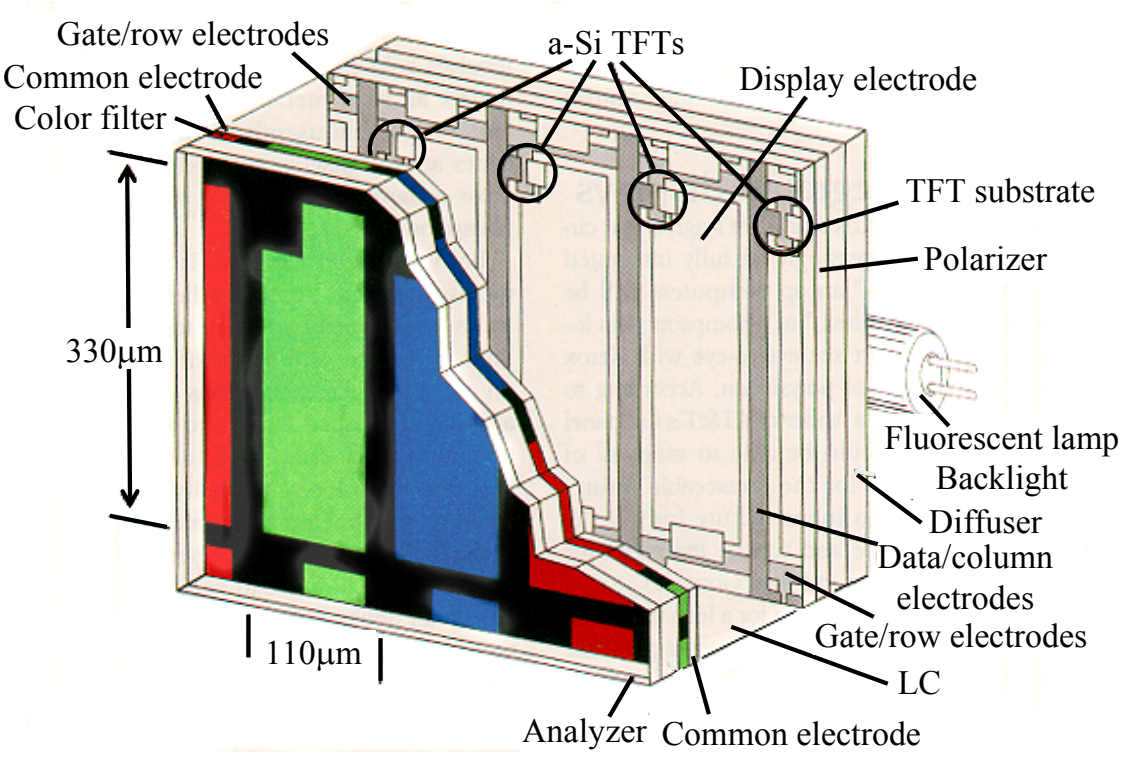


Figure 1.1: Schematic diagram of a transmissive mode liquid crystal display [1].

As drafted in Figure 1.1, an aligned liquid crystal cell is laminated between two linear polarizers. Liquid crystal is filled into the gap between two glass substrates to compose the liquid crystal cell. Alignment layers on the substrate-LC interfaces provide a certain kind of boundary condition so that the liquid crystal directors are aligned uniformly. The unpolarized white light emitting from the backlight unit is converted into the linearly polarized light after it passes through the linear polarizer (polarizer). Due to the anisotropic characteristics of liquid crystal, the polarization state of the incident light deviates from the linear polarization when the light passes thorough the liquid crystal layer. If the emerging state of polarization is linear and vibrates along the absorption direction of the other linear polarizer (analyzer), which is laminated

on the other side of the liquid crystal cell, then the most of light is absorbed. This results in the dark state. If the emerging state of polarization is other than the linear polarization, then some of the light can be transmitted. This gives the gray levels. If the emerging state of polarization is still linear but vibrates perpendicular to the absorption direction of the analyzer, then the most of the light is transmitted. This produces the bright state.

To produce different states of polarization, various voltages are applied to the liquid crystal so that the liquid crystal directors are reoriented and the phase retardations of the liquid crystal layer are different. Common electrodes and display electrodes are deposited on the glass substrates adjacent to the liquid crystal, which is illustrated in Figure 1.1. The display electrodes are connected to the corresponding thin-film-transistor. Alignment layers are deposited on the surfaces of the electrodes. For the twisted-nematic liquid crystal (TN-LC) cell and vertical-alignment liquid crystal (VA-LC) cell, the common electrodes and display electrodes are on the other sides of the liquid crystal layer. For the in-plane-switching liquid crystal (IPS-LC) cell, the common electrodes and display electrodes are interlaced on the same side of the liquid crystal layer.

The majority of liquid crystal displays operate in the normally black mode, i.e., the liquid crystal displays are dark without applied voltage and become brighter when the applied voltage increases [1-3]. Comparing with the normally white mode, normally black mode has the advantage of intrinsically high contrast ratio, because the liquid crystal displays are designed and optimized for the dark state. Inside most of these liquid crystal displays, the linear polarizers are crossed to each other to produce normally back mode.

Currently liquid crystal displays are dominating the flat panel display markets and the sharing of large screen television markets is growing fast [1-3]. Wide viewing angle, high

contrast ratio, small color shift, deep color saturation, fast response time, and low power consumption are the major technical challenges for the next generation liquid crystal displays in addition to lower production cost [1, 3-6]. Driven by the growing demands on the markets, wide viewing angle becomes increasingly important when the screen size of liquid crystal televisions becomes larger and larger.

The viewing angle characteristics of liquid crystal displays strongly depend on the employed liquid crystal modes. From the viewpoint of the applied electric field, these liquid crystal modes can be categorized into two groups: longitudinal and transversal (or fringing) electric fields. In the voltage-on state, if the liquid crystal directors are tilted out-of-the-plane under the longitudinal electric fields, e.g., the $90^{o}$ twisted-nematic liquid crystal cell [7], vertical-alignment liquid crystal [8-9], and bend cell [10], then their intrinsic viewing angle is narrow and asymmetric, because the polarization produced from the liquid crystal layer changes dramatically with the viewing angle so that the light leakage becomes significant at oblique viewing angles. To reduce the light leakage and widen the viewing angle, optical phase compensation films are applied so that the polarization state emerging from the liquid crystal layer is less sensitive to the viewing angle. If the liquid crystal directors are reoriented in the same plane under the transversal electric fields, e.g., the in-plane-switching liquid crystal cell [11-12], then the intrinsic viewing angle is wider. However, the light leakage of the crossed polarizers at oblique viewing angles puts an ultimate limitation to the viewing angle. To suppress this kind of light leakage, additional phase compensation films are laminated to the crossed polarizers. Therefore, the designs of the optical phase compensation films are critical for the wide viewing angle liquid crystal displays.

Several designs were proposed to reduce the dark state light leakage [6-9, 11-15]. Higher than 300:1 contrast ratio over the $\pm 80^{o}$ viewing cone was reported for an in-plane-switching liquid crystal display (IPS-LCD) [11-12]. However, for the vertical-alignment liquid crystal display (VA-LCD), the reported ~100:1 iso-contrast ratio is limited to the $\pm 50^{o}$ viewing cone [13-15]. This is insufficient for television applications, although the vertical alignment mode liquid crystal displays have the advantages of excellent contrast ratio at normal viewing direction, weak color dispersion, and fast response time. There is an urgent need to extend the high contrast ratio to a wider viewing cone.

This dissertation researches on the designs of wide viewing angle liquid crystal displays. Different novel wide-view and high contrast liquid crystal displays using linear polarizers and circular polarizers are proposed.

After an introduction of wide-view technologies in Chapter 1, Chapter 2 discusses the applied numerical simulation methods. Finite difference method is employed to simulate the liquid crystal director distributions. The extended Jones matrix method and the four-by-four matrix method are applied to evaluate the light transmittance and calculate the states of polarization for the liquid crystal displays.

Chapter 3 presents a wide viewing angle and high contrast ratio vertical-alignment liquid crystal display utilizing crossed linear polarizers [16]. Phase compensation films are applied to reduce the dark state light leakage. After analyzing the polarization states inside this VA-LCD, the design of compensation films is optimized using the oblique angle Jones matrix. With the proposed design, the dark state light leakages are minimized and high contrast ratio is achieved over wide viewing angles for a multi-domain VA-LCD.

Chapter 4 proposes the designs of wide-view and broadband circular polarizers using a linear polarizer and the combinations of uniaxial phase retardation films [26]. In addition to high contrast ratio, high transmittance and low color shift over wide viewing angles are also highly desired for high performance liquid crystal televisions (LCD TVs). It was shown that the transmittance of a multi-domain VA-LCD can be significantly improved using crossed circular polarizers [17-25]. Using the combinations of phase retardation films, the linear polarization emerging from the linear polarizer is converted into circular polarization. At oblique viewing angles, the polarizations are subtly modified in the retardation films so that the viewing angle sensitivity of the circular polarizer is significantly reduced. The produced states of polarization are very close to the ideal circular state of polarization over wide viewing angles for the visual spectrum. This guarantees not only high contrast ratio but also high and uniform transmittance over wide viewing angles for wide-view liquid crystal display.

Chapter 5 applies the designed wide-view and broadband circular polarizer to a multi-domain VA-LCD [26]. Both the transmittance and the angular uniformity of the presented wide-view multi-domain VA-LCD are significantly improved and the high contrast ratio is maintained.

Chapter 6 proposes a broadband and wide-view circular polarizer consisting of a linear polarizer and two biaxial phase retardation films [27]. The device configuration of the broadband and wide-view circular polarizer is significantly simplified while the produced states of polarization remain close to the circular polarization over wide viewing angles for the visual white light. This reduces the cost and improves the applicability of the broadband and wide-view circular polarizer.

Chapter 7 applies the wide-view circular polarize introduced in Chapter 6 to a vide-view liquid crystal display [28]. The proposed wide-view LCD demonstrates high contrast ratio as

well as high and uniform transmittance over wide viewing angles for the visual spectrum. Finally, a conclusion is given in Chapter 8.

# CHAPTER TWO: NUMERICAL SIMULATIONS FOR LIQUID CRYSTAL DISPLAYS

The knowledge of the liquid crystal (LC) director distribution and the light transmittance is important in the design and optimization of wide viewing angle liquid crystal displays. Both the director distribution and the light transmittance can be numerically simulated [29-40]. In this dissertation, the director distribution is simulated using the finite difference method and the light transmittance is evaluated using the extended Jones matrix method or the four-by-four matrix method.

## 2.1. Numerical modeling of the liquid crystal director distributions

To analyze the electro-optical characteristics of liquid crystal devices, the liquid crystal director distributions under the applied voltage must be known. We use two steps approach to solve the director distributions: solve the voltage distributions using the finite element method (FEM) [34-35], and then obtain the liquid crystal director distributions using the finite difference method (FDM) [31-35].

The electric energy under applied voltage is [2, 32-34]

$$f_{Electric} = \iiint\left(\frac{1}{2}\mathbf{D}\cdot\mathbf{E}\right)dv = \iiint\left(\frac{1}{2}\mathbf{E}\cdot\mathbf{E}\right)dv = \iiint\left(\frac{1}{2}\varepsilon\nabla V\cdot\nabla V\right)dv\,, \tag{2.1}$$

where $V$ is voltage distribution, and $\boldsymbol{\varepsilon}$ is the dielectric tensor of the liquid crystal. Applying the variational method, the liquid crystal device is discretized by the first order uniform rectangular mesh so that there are eight nodes in each rectangular element. The voltage distribution is expressed as a set of linear equations [34]

$$V(x,y,z)=\sum_{e=1}^{Ne}\sum_{i=1}^{8}V_i^e(x,y,z)N_i^e(x,y,z), \tag{2.2}$$

where $V_i^e$ is the unknown voltage at the node $i$ of element $e$, $N_e$ is the total number of elements, and $N_i^e(x,y,z)$ is the shape function.

The variation of the electric energy $F_{Electric}$ on the voltage $V_m$ of node $m$ is equal to 0, which gives the voltage distributions after solving the following linear algebraic equation [34]

$$\begin{pmatrix} A_{11} & A_{12} & \cdots & A_{1N_{node}} \\ A_{21} & A_{22} & \cdots & A_{2N_{node}} \\ \vdots & \vdots & \ddots & \vdots \\ A_{N_{node}1} & A_{N_{node}2} & \cdots & A_{N_{node}N_{node}} \end{pmatrix}\begin{pmatrix} V_1 \\ V_1 \\ \vdots \\ V_{N_{node}} \end{pmatrix}=0, \tag{2.3}$$

where

$$A_{mn}=\frac{\partial^2 F_{Electric}^e}{\partial V_m \partial V_n}.$$

In the following, we will discuss the solution of liquid crystal director distributions. Using Euler-Lagrangian equation together with a Rayleigh dissipation function we have [31-33]

$$\gamma_1\frac{dn_i}{dt}=-\left[f_g\right]_{n_i}+\lambda n_i,\quad i=x,y,z. \tag{2.4}$$

Here $\gamma_1$, $n_i$, and $\lambda$ are the rotational viscosity, Cartesian component of liquid crystal director, a Lagrange multiplier to keep the liquid crystal director as a unit vector, respectively. $\left[f_g\right]_{n_i}$ in Equation 2.4 is [31-33]

$$\left[f_g\right]_{n_i} = \frac{\partial f_g}{\partial n_i} - \frac{d}{dx}\left(\frac{\partial f_g}{\partial(d\, n_i/dx)}\right) - \frac{d}{dy}\left(\frac{\partial f_g}{\partial(d\, n_i/dy)}\right) - \frac{d}{dz}\left(\frac{\partial f_g}{\partial(d\, n_i/dz)}\right), \quad i = x, y, z\,. \tag{2.5}$$

Here $f_g$ is the Gibbs free energy density given by

$$f_g = f_S - f_E\,, \tag{2.6}$$

where $f_s$ and $f_E$ are the elastic free energy and the electric energy, respectively.

The elastic free energy of liquid crystal can be expressed as [31-33]

$$f_{Elastic} = \frac{1}{2}k_{11}\left(\nabla\cdot\mathbf{n}\right)^2 + \frac{1}{2}k_{22}\left(\mathbf{n}\cdot\nabla\times\mathbf{n}\right)^2 + \frac{1}{2}k_{33}\left(\mathbf{n}\times\nabla\times\mathbf{n}\right)^2, \tag{2.7}$$

where **n** is the director vector, and $K_{11}$, $K_{22}$, and $K_{33}$ are and the elastic constants associated with spray, twist and bend, respectively.

With the known electric energy and the elastic free energy, the update equation of the liquid crystal directors after each time step $dt$ can be derived from Equation 2.5 as

$$n_i = \frac{1}{\lambda}\left(\left[f_g\right]_{n_i} + \gamma_1\frac{dn_i}{dt}\right), \quad i = x, y, z\,. \tag{2.8}$$

Inside a multi-domain vertical-alignment liquid crystal display (VA-LCD), initially the liquid crystal directors are perpendicular to the substrates. After applying the external voltage, the electric field is built up and the liquid crystal directors start to reorient so that the liquid

crystal director distributions are changed. The changes in the liquid crystal director distributions result in the changes of the voltage distributions and the electric energy distributions. This process continues until the total free energy is uniform [31-33].

In the simulation of a vertical alignment liquid crystal (VA-LC) device, the liquid crystal directors are initialized as perpendicular to the substrates. After the voltage is applied, the voltage distributions can be solved using the above mentioned simulation method. With the known voltage distributions, the liquid crystal director distributions are updated using Equations 2.6 to 2.8 with a time step less than the maximum time step, which is defined as [31-33]

$$\Delta t_{\max} = \frac{\Delta x^2 \gamma_1}{2K_{33}}, \tag{2.9}$$

where $\Delta x$ is the minimum meshing size of the $x$, $y$, $z$ direction. At each time step, the director distributions are recorded and later will be used in the simulation of the light transmittance of liquid crystal device. After the liquid crystal director distributions are updated, the voltage distributions and the electric energy distributions must be updated to represent the changes in the voltage distributions. This iteration continues till an arbitrary number of iteration is reached or the variation in the liquid crystal director distributions is smaller than a threshold.

## 2.2. Numerical modeling of optical characteristics of liquid crystal displays

With the known liquid crystal director distributions, the light transmittance can be solved using the extended Jones matrix method or the four-by-four matrix method [36-39]. Applying either the extended Jones matrix method or the four-by-four matrix method, the liquid crystal

device including the two polarizers is discretized into N layers in the direction perpendicular to the substrates, as shown in Figure 2.1. A Cartesian coordinate system can be chosen such that the x-y plane is parallel to the substrates and the wavevector **k** of the incident plane wave is inside the x-z plane. The direction of z-axis is pointing from the entrance polarizer to the exit polarizer. The wavevector of the incident wave in this coordinate system is given by [37-39]

$$\mathbf{k}_{\mathbf{in}} = \mathbf{x}k_o \sin\theta_k + \mathbf{y}0 + \mathbf{z}k_o \cos\theta_k \tag{2.10}$$

where $k_0$ is the wavenumber in free space, $\theta_k$ is elevation angle of the incident plane wave, and **x**, **y**, and **z** are and the unit vector in the x, y, z direction, respectively.

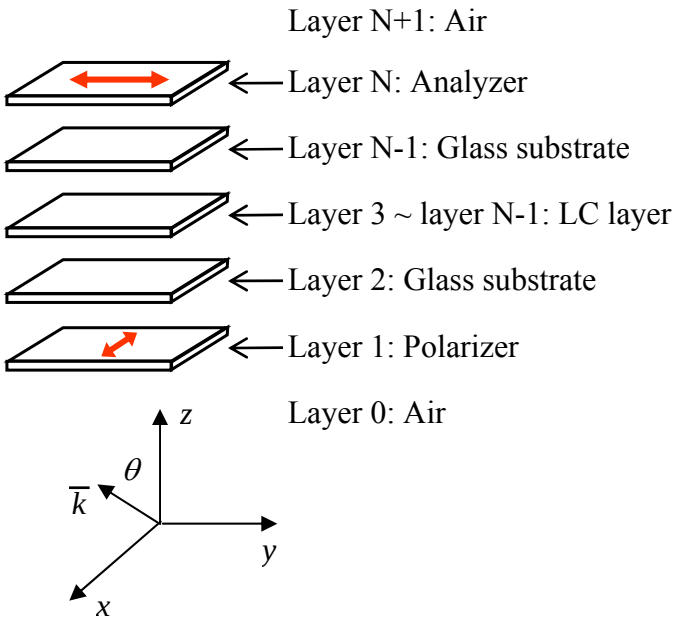


Figure 2.1: Schematic diagram of a VA-LCD, which is divided into N layers.

If we define a normalized magnetic field intensity [39]

$$\widehat{\mathbf{H}} = \eta_0 \mathbf{H} = \sqrt{\frac{\mu_0}{\varepsilon_0}}\mathbf{H}, \tag{2.11}$$

Maxwell's equations become

$$\begin{aligned} \nabla \times \mathbf{E} &= ik_0 \widehat{\mathbf{H}} \\ \nabla \times \widehat{\mathbf{H}} &= -ik_0 \varepsilon\ \mathbf{E}\ . \end{aligned} \tag{2.12}$$

After the expansion of Maxwell's equations, we have

$$\frac{\partial}{\partial z}\begin{bmatrix} E_x \\ E_y \\ \widehat{H}_x \\ \widehat{H}_y \end{bmatrix} = ik_0 \mathbf{Q} \begin{bmatrix} E_x \\ E_y \\ \widehat{H}_x \\ \widehat{H}_y \end{bmatrix}, \tag{2.13}$$

where **Q** is a coupling matrix defined by

$$\mathbf{Q} = \begin{bmatrix} -\frac{\varepsilon_{zx}}{\varepsilon_{zz}}\sin\theta_k & -\frac{\varepsilon_{zy}}{\varepsilon_{zz}}\sin\theta_k & 0 & 1--\frac{\sin^2\theta_k}{\varepsilon_{zz}} \\ 0 & 0 & -1 & 0 \\ -\varepsilon_{yx}+\varepsilon_{yz}\frac{\varepsilon_{zx}}{\varepsilon_{zz}} & -\varepsilon_{yy}+\varepsilon_{yz}\frac{\varepsilon_{zy}}{\varepsilon_{zz}}+\sin^2\theta_k & 0 & \frac{\varepsilon_{yz}}{\varepsilon_{zz}}\sin\theta_k \\ \varepsilon_{xx}-\varepsilon_{xz}\frac{\varepsilon_{zx}}{\varepsilon_{zz}} & \varepsilon_{xy}-\varepsilon_{xz}\frac{\varepsilon_{zy}}{\varepsilon_{zz}} & 0 & -\frac{\varepsilon_{xz}}{\varepsilon_{zz}}\sin\theta_k \end{bmatrix}. \tag{2.14}$$

For each layer, the matrix **Q** can be diagonalized as

$$\mathbf{Q} = \mathbf{T}\begin{bmatrix} q_1 & & & \\ & q_2 & & \\ & & q_3 & \\ & & & q_4 \end{bmatrix}\mathbf{T}^{-1}, \tag{2.15}$$

where $q_1$, $q_2$, $q_3$ and $q_4$ are the four eigenvalues given by

$$
\begin{aligned}
q_1 &= \left(n_o^2 - \sin^2\theta_k\right)^{1/2}, \\
q_2 &= -\frac{\varepsilon_{xz}}{\varepsilon_{zz}}\sin\theta_k + \frac{n_o n_e}{\varepsilon_{zz}}\left[\varepsilon_{zz} - \left(1 - \frac{n_e^2 - n_o^2}{n_e^2}\cos^2\theta\sin^2\phi\right)\sin^2\theta_k\right]^{1/2}, \\
q_3 &= -q_1, \\
q_4 &= -q_2,
\end{aligned}
\tag{2.16}
$$

where $q_1$ and $q_2$ correspond to two forward eigenwaves, and $q_3$ and $q_4$ correspond to two backward eigenwaves.

If we define [39]

$$
\begin{bmatrix} E_x \\ E_y \\ \widehat{H}_x \\ \widehat{H}_y \end{bmatrix} = \mathbf{T}\begin{bmatrix} U_1 \\ U_2 \\ U_3 \\ U_4 \end{bmatrix} = \begin{bmatrix} \mathbf{T}_{11} & \mathbf{T}_{12} \\ \mathbf{T}_{21} & \mathbf{T}_{22} \end{bmatrix}\begin{bmatrix} U_1 \\ U_2 \\ U_3 \\ U_4 \end{bmatrix}, \tag{2.17}
$$

applying Equations 2.15 and 2.17 to Equation 2.13, we have the decoupled equation

$$
\frac{\partial}{\partial z}\begin{bmatrix} U_1 \\ U_2 \\ U_3 \\ U_4 \end{bmatrix} = ik_0\begin{bmatrix} q_1 & & & \\ & q_2 & & \\ & & q_3 & \\ & & & q_4 \end{bmatrix}\begin{bmatrix} U_1 \\ U_2 \\ U_3 \\ U_4 \end{bmatrix}. \tag{2.18}
$$

For the nth layer, the solution of Equation 2.18 is

$$
\begin{bmatrix} U_1 \\ U_2 \\ U_3 \\ U_4 \end{bmatrix}_{n,d_n} = \mathbf{H}_n\begin{bmatrix} U_1 \\ U_2 \\ U_3 \\ U_4 \end{bmatrix}_{n,0}, \tag{2.19}
$$

where $\begin{bmatrix} U_1 \\ U_2 \\ U_3 \\ U_4 \end{bmatrix}_{n,0}$ and $\begin{bmatrix} U_1 \\ U_2 \\ U_3 \\ U_4 \end{bmatrix}_{n,d_n}$ are the eigenwaves on the input and output boundary of layer n, respectively. The matrix $\mathbf{H}_n$ is

$$\mathbf{H}_n = \begin{bmatrix} \exp\left(ik_{z_1} d_n\right) & & & \\ & \exp\left(ik_{z_2} d_n\right) & & \\ & & \exp\left(ik_{z_3} d_n\right) & \\ & & & \exp\left(ik_{z_4} d_n\right) \end{bmatrix}, \tag{2.20}$$

where

$$\begin{aligned} k_{z_1} &= k_0 q_1, \\ k_{z_1} &= k_0 q_2, \\ k_{z_1} &= k_0 q_3, \\ k_{z_1} &= k_0 q_4. \end{aligned} \tag{2.21}$$

Applying Equation 2.19 to Equation 2.17, the electric field on the output boundary of the nth layer is related to the electric field on the input boundary of the same layer by

$$\begin{bmatrix} E_x \\ E_y \\ \widehat{H}_x \\ \widehat{H}_y \end{bmatrix}_{n,d_n} = \mathbf{P}_n \begin{bmatrix} E_x \\ E_y \\ \widehat{H}_x \\ \widehat{H}_y \end{bmatrix}_{n,0}, \tag{2.22}$$

where $\mathbf{P}_n$ is the 4-by-4 matrix of the nth layer,

$$\mathbf{P}_n = \mathbf{T}_n \mathbf{H}_n \mathbf{H}_n^{-1}. \tag{2.23}$$

Thus the 4-by-4 matrix of the simulated LC device is

$$\mathbf{P} = \mathbf{P}_N \mathbf{P}_{N-1} \cdots \mathbf{P}_2 \mathbf{P}_1. \tag{2.24}$$

For the extended Jones matrix method, we assume the reflections inside the LC device are neglectable and consider only the forward eigenwaves. Equation 2.17 becomes

$$\begin{bmatrix} E_x \\ E_y \end{bmatrix} = \mathbf{T}_{11} \begin{bmatrix} U_1 \\ U_2 \end{bmatrix} = \mathbf{S} \begin{bmatrix} U_1 \\ U_2 \end{bmatrix}. \tag{2.25}$$

For the eigenwave in the nth layer, we have

$$\begin{bmatrix} U_1 \\ U_2 \end{bmatrix}_{n,d_n} = \mathbf{G}_n \begin{bmatrix} U_1 \\ U_2 \end{bmatrix}_{n,0}, \tag{2.26}$$

where

$$\mathbf{G}_n = \begin{bmatrix} \exp\left(ik_{z_1} d_n\right) & \\ & \exp\left(ik_{z_2} d_n\right) \end{bmatrix}. \tag{2.27}$$

Applying Equation 2.25 to Equation 2.24, the extended Jones matrix of the nth layer is

$$\mathbf{J}_n = \mathbf{S}_n \mathbf{G}_n \mathbf{S}_n^{-1}, \tag{2.28}$$

from which we can obtain the extended Jones matrix of the simulated LC device as

$$\mathbf{J} = \mathbf{J}_N \mathbf{J}_{N-1} \cdots \mathbf{J}_2 \mathbf{J}_1. \tag{2.29}$$

Considering the transmission loss in the air-LCD interface, the transmitted electric field is related to the incident electric field by [37-39]

$$\begin{bmatrix} E_x \\ E_y \end{bmatrix}_{N+1} = \mathbf{J} \begin{bmatrix} E_x \\ E_y \end{bmatrix}_1 = \mathbf{J}_{Ext} \mathbf{J}_N \mathbf{J}_{N-1} \cdots \mathbf{J}_2 \mathbf{J}_1 \mathbf{J}_{Ent} \begin{bmatrix} E_x \\ E_y \end{bmatrix}_1, \tag{2.30}$$

where $\mathbf{J}_{Ext}$ and $\mathbf{J}_{Ent}$ are the matrices considering the surface reflections on the air-LCD interfaces, which are governed by [37-39]

$$\boldsymbol{J}_{Ent} = \begin{bmatrix} \dfrac{2\cos\theta_p}{\cos\theta_p + n_p\cos\theta_k} & 0 \\ 0 & \dfrac{2\cos\theta_k}{\cos\theta_k + n_p\cos\theta_p} \end{bmatrix},$$
$$\boldsymbol{J}_{Ext} = \begin{bmatrix} \dfrac{2n_p\cos\theta_k}{\cos\theta_p + n_p\cos\theta_k} & 0 \\ 0 & \dfrac{2n_p\cos\theta_p}{\cos\theta_k + n_p\cos\theta_p} \end{bmatrix}, \tag{2.31}$$

where $n_p$ is the index of refraction of the polarizer, and $\theta_p$ is defined as

$$\theta_p = \sin^{-1}\left[\sin\theta_k \,/\, \mathrm{Re}\left(\left(n_{e,p} + n_{o,p}\right)/2\right)\right], \tag{2.32}$$

here $n_{e,p}$ and $n_{o,p}$ are the refractive indices of the polarizer.

Thus, the overall optical transmittance $t_{op}$ is

$$t_{op} = \frac{\left|E_{x,N+1}\right|^2 + \cos^2\theta_p\left|E_{y,N+1}\right|^2}{\left|E_{x,1}\right|^2 + \cos^2\theta_p\left|E_{y,1}\right|^2}. \tag{2.33}$$

## 2.3. Summary

To analyze the electro-optical characteristics of liquid crystal displays, we first use the finite difference method to simulate the liquid crystal director distributions under the applied voltages. With the known liquid crystal director distributions, we use the extended Jones matrix method or the four-by-four matrix method to solve the transmittance or the reflectance of liquid crystal displays as well as the polarization states of the light.

# CHAPTER THREE: WIDE VIEW AND HIGH CONTRAST LIQUID CRYSTAL DISPLAYS USING CROSSED LINEAR POLARIZERS

High contrast ratio and wide viewing angle are critical requirements for liquid crystal televisions. Presently, the view angle of a liquid crystal display (LCD) is defined at iso-contrast ratio greater than 10:1. A low contrast ratio implies a poor color rendering. Vertical alignment liquid crystal (VA-LCD) exhibits an excellent contrast ratio at normal viewing direction, weak color dispersion, and fast response time [1, 5-6, 8-9, 11-13], however, its dark state light leakage at oblique angles is relatively large resulting in a degraded contrast ratio. Several analyses indicate that the dark state light leakage is determined by the polarization state of the outgoing light beam before reaching the analyzer [1, 3, 6-9, 11-15]. To reduce the dark state light leakage, different liquid crystal operation modes and compensation films have been proposed. For examples, the in-plane-switching (IPS) and optically compensated bend (OCB) mode could exhibit a 300:1 contrast ratio over the $\pm 80^{o}$ viewing cone [11-12]. However, for vertical-alignment (VA) mode the reported ~100:1 iso-contrast ratio is limited to the $\pm 50^{o}$ viewing cone [14-15]. This is insufficient for television applications. There is an urgent need to extend the high contrast ratio to a wider viewing cone.

In this chapter, we optimize the design of a four-domain VA-LCD which shows an extraordinarily high contrast ratio over the entire $\pm 85^{o}$ viewing cone [16]. We begin with analyzing the polarization states inside the VA-LCD, and then optimizing the design of the

compensation films using the oblique angle Jones matrix so that the dark state light leakages are minimized. Finally, we are able to obtain a VA-LCD with iso-contrast ratio higher than 10,000:1 over the ±85$^{o}$ viewing cone.

## 3.1. State of polarization inside the VA-LCD

Figure 3.1 depicts the device configuration of a four-domain VA-LCD with A-plate and C-plate compensation films. The absorption axes of polarizer and analyzer are in 0$^{o}$ and 90$^{o}$, respectively. Two A-plate films with equal thickness are laminated on the inner side of the crossed linear polarizers with their slow axes perpendicular to the absorption axes of the corresponding polarizers. Two equal thickness C-plate films are inserted between A-plate films and glass substrates. In the bright state, four domains are formed at 45$^{o}$, 135$^{o}$, 225$^{o}$, and 315$^{o}$. We use the finite difference method to simulate the bright state LC director distributions [31-33].

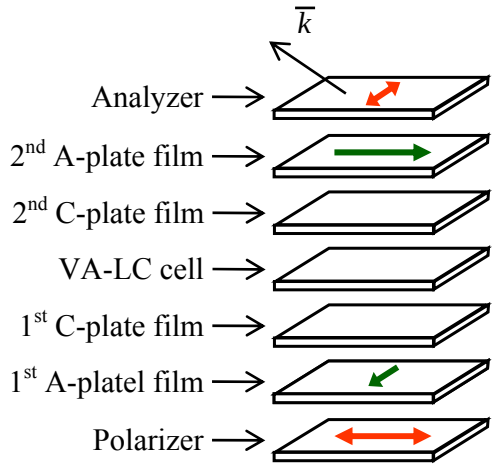


Figure 3.1: Structure of a VA-LCD for the optimized design. The slow axis of each A-plate film is perpendicular to the absorption axis of the adjacent polarizer.

The entire LCD is treated as multi-layer device with each layer approximated by uniaxial anisotropic media [38-39]. Assuming the reflections between internal layers are negligible, the transmitted wave after the m$^{th}$ layer is related to the incident wave as [37-39]

$$\begin{bmatrix} E_{//} \\ E_{\perp} \end{bmatrix}_m = J_m \cdot J_{m-1} \cdots J_2 \cdot J_1 \cdot J_{ent} \cdot \begin{bmatrix} E_{//} \\ E_{\perp} \end{bmatrix}_{in}, \tag{3.1}$$

where $J_m$ is the Jones matrix of the m$^{th}$ layer and $J_{ent}$ is the correction matrix considering reflections on the air-polarizer interface. Approximating the propagating light inside LCD by plane wave, at viewing angle $\theta$ and azimuthal angle of incident plane $\phi$, $J_m$ is obtained as [41-42]

$$J_m = \begin{bmatrix} \cos\Psi & -\sin\Psi \\ \sin\Psi & \cos\Psi \end{bmatrix} \cdot \begin{bmatrix} e^{-j\frac{2\pi}{\lambda}\frac{d}{\cos\theta_m}n'_e} & 0 \\ 0 & e^{-j\frac{2\pi}{\lambda}\frac{d}{\cos\theta_m}n'_o} \end{bmatrix} \cdot \begin{bmatrix} \cos\Psi & \sin\Psi \\ -\sin\Psi & \cos\Psi \end{bmatrix}, \tag{3.2}$$

where $\lambda$ is the wavelength, $d$ is the thickness of the m$^{th}$ layer, $\theta_m$ is the angle of light inside the m$^{th}$ layer, and $n'_e$ and $n'_o$ are the refractive indices of the m$^{th}$ layer media on the wave plane.[1, 13] As shown in Figure 3.2, $\overline{O'L}$ denotes the projection of the optical axis of the m$^{th}$ layer ($\overline{OL}$) on the wave plane and $\Psi$ is the angle between $E_{//}$ and $\overline{O'L}$, which is found to be

$$\Psi = sign\left(\sin\theta_{ne} - \frac{\cos\theta_{ne}\cos(\phi-\phi_{ne})}{\tan\theta_m}\right) \cdot \left[\arcsin\left(\frac{\cos\theta_{ne}\sin(\phi-\phi_{ne})}{\sin\Theta}\right)\right], \tag{3.3}$$

where *sign*() is the sign function to distinguish angles greater than 90$^o$, and $\theta_{ne}$ and $\phi_{ne}$ are the tilt and twist angles of $\overline{OL}$, respectively. In Figure 3.2, $\Theta$ is the angle between $\overline{OL}$ and wave vector ($\bar{k}$), which can be obtained from the dot product of $\overline{OL}$ and $\bar{k}$.

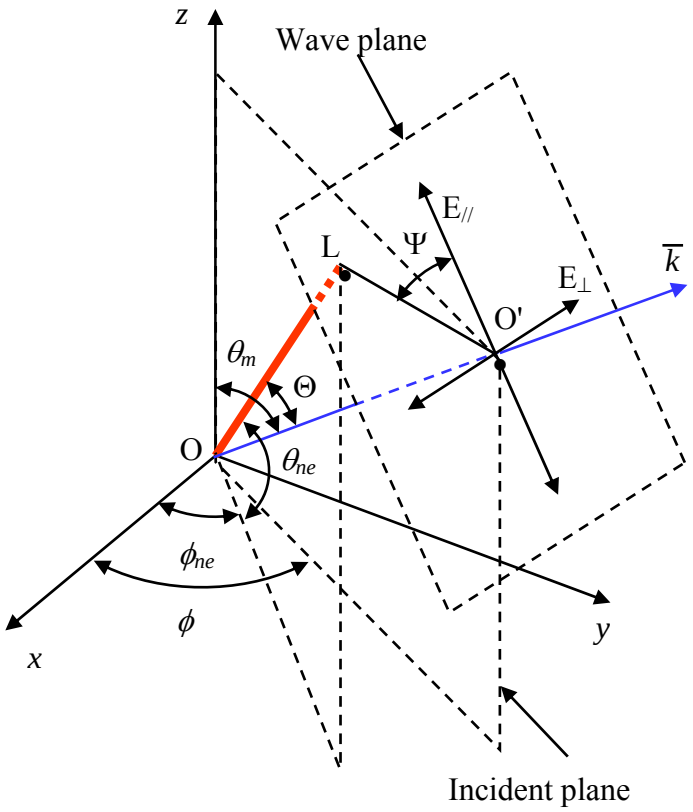


Figure 3.2: The principal optical axis of the m$^{th}$ layer ($\overline{OL}$) and its projection on the wave plane ($\overline{O'L}$).

State of polarization can be represented by Stokes parameters and plotted on Poincaré sphere, as shown in Figure 3.3, after $E_{//}$ and $E_{\perp}$ are solved [41-42]. Coordinates of Poincaré sphere are the standard Stokes parameters $S_1$, $S_2$ and $S_3$. Due to the symmetry of VA-LCD in the dark state, we only investigate the states of polarization when $0^o \leq \phi \leq 90^o$. Results are applicable to $90^o \leq \phi \leq 360^o$. With the known $E_{//}$ and $E_{\perp}$, the bright and dark state transmittance can be obtained [37-39]. Contrast ratio is defined as the ratio of bright state transmittance over dark state light leakage.

In Figure 3.3, **A** denotes the state of polarization absorbed by the analyzer, **B** denotes the state of polarization in front of the analyzer, **D** denotes the state of polarization emerging from the VA LC layer, **G** denotes the state of polarization emerging behind the first A-plate film, and **P** denotes the state of polarization passing through the polarizer.

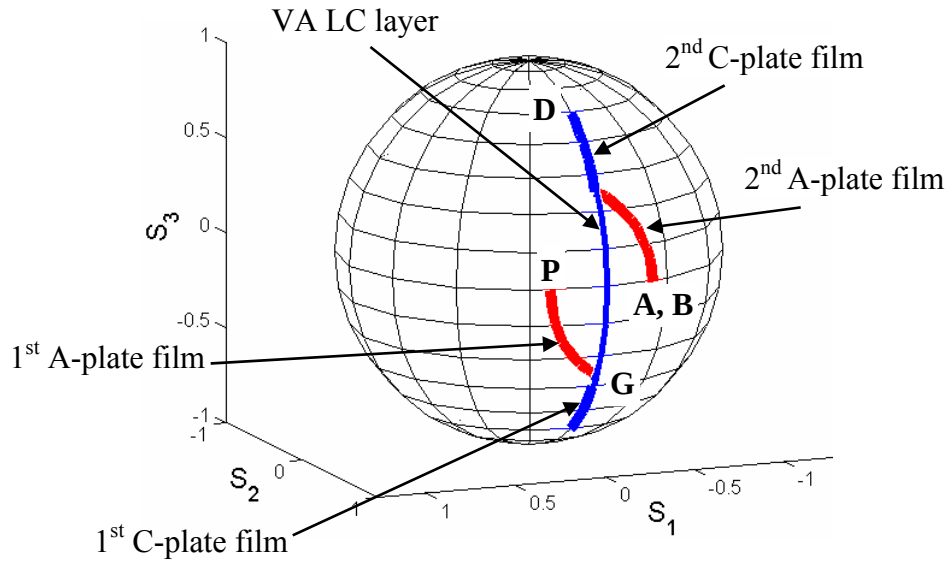


Figure 3.3: States of polarization inside a VA-LCD with optimized designed compensation films at $\theta = 70^{o}$, $\phi = 45^{o}$ and $\lambda = 550$ nm. **P**, **G**, **D**, **B**, and **A** denote the state of polarization passing through polarizer, emerging from 1st A-plate film, emerging from the VA LC layer, in front of the analyzer, and absorbed by the analyzer, respectively.

## 3.2. Effects of viewing angle on the states of polarization inside the VA-LCD

To analyze the effects of viewing angle on the states of polarization inside VA-LCD, we first obtain the Jones matrix of VA LC layer from Equation 3.2 as

$$J = e^{-j\frac{\pi}{\lambda}\frac{d}{\cos\theta_{LC}}(n'_e+n'_o)}\begin{bmatrix} e^{-j\frac{\pi}{\lambda}\frac{d}{\cos\theta_{LC}}(n'_e-n'_o)} & 0 \\ 0 & e^{j\frac{\pi}{\lambda}\frac{d}{\cos\theta_{LC}}(n'_e-n'_o)} \end{bmatrix}. \tag{3.4}$$

As Equation 3.4 shows, there is no coupling between $E_{//}$ and $E_{\perp}$ so that $S_1$ is not changed when light passes through LC layer. However, the phase of $E_{\perp}$ leads the phase of $E_{//}$ for a positive LC ($n_e > n_o$) and the difference increases with viewing angle $\theta$. Therefore, at oblique viewing angle, $S_3$ of **D** is greater than zero and increases with viewing angle for a linearly polarized input light. If there is no anisotropic media between LC layer and analyzer, **B** equals **D**. Next, we model linear polarizer as lossy uniaxial anisotropic media. As Figure 3.4 illustrates, on the wave plane, the maximum absorption direction of analyzer is along $\overline{O'L_{ana}}$ and the maximum transmission direction of polarizer is along $\overline{O'Q_{pol}}$. Therefore, the difference between $S_1$ of **P** and $S_1$ of **A** depends on the angle between $\overline{O'Q_{pol}}$ and $\overline{O'L_{ana}}$, which is related to viewing angle $\theta$ and azimuthal angle $\phi$ as

$$\Phi = \arctan\left(\frac{\cos\phi}{\sin\phi\cos\theta_{pol}}\right) + \arctan\left(\frac{\sin\phi}{\cos\phi\cos\theta_{pol}}\right) - 90^0. \tag{3.5}$$

Taking the derivative of $\Phi$ with respect to $\phi$ reveals that $\Phi$ reaches maximum at $\phi = 45^o$. Next, taking the derivative of $\Phi$ with respect to $\theta_{pol}$ at $\phi = 45^o$ shows that $\Phi$ increases with viewing angle $\theta$. Therefore, the maximum of the difference between $S_1$ of **A** and $S_1$ of **P** occurs at

maximal viewing angle when $\phi$ = 45°. For a conventional VA-LCD, $S_1$ of **P** is not changed before the light reaches analyzer. Therefore, the $S_1$ of **B** equals the $S_1$ of **P**.

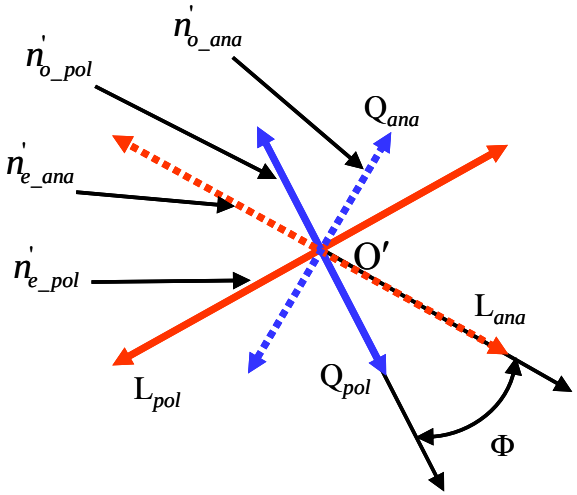


Figure 3.4: Angle between the maximum transmission direction of the polarizer ($\overline{O'Q_{pol}}$) and the maximum absorption direction of the analyzer ($\overline{O'L_{ana}}$). $\overline{O'Q_{pol}}$ is perpendicular to the maximum absorption direction of the polarizer ($\overline{O'L_{pol}}$).

For a conventional VA-LCD, the difference between **B** and **A** increases with viewing angle. If **B** and **A** are equal at a large oblique viewing angle when $\phi$ = 45°, then the dark state light leakage would be greatly reduced at other viewing angles as well. Due to the symmetry of the device configuration shown in Figure 3.1, the $S_1$ of **G** should satisfy the following condition

$$S_{1\_G} = \left(S_{1\_P} + S_{1\_A}\right)/2 . \tag{3.6}$$

Figure 3.3 illustrates the above relationship.

## 3.3. Optimization design of the phase compensation films

To design A-plate film, we first find $E_{//\_G}$ and $E_{\perp\_G}$ (after the 1st A-plate film) in terms of the A-plate film thickness ($d_{A\text{-}plate}$) using Equation 3.1, provided that the polarizer thickness and refractive index and the A-plate refractive index are known. Next, after $S_1$ of **A** and $S_1$ of **P** are solved, Equation 3.6 can be expressed as

$$S_{1\_G} = \frac{\left(\left|E_{//\_G}\right|^2 - \left|E_{\perp\_G}\right|^2\right)}{\left(\left|E_{//\_G}\right|^2 + \left|E_{\perp\_G}\right|^2\right)} = \frac{\left(S_{1\_P} + S_{1\_A}\right)}{2}. \tag{3.7}$$

Simplification of Equation 3.7 results in

$$H_1 \cdot \cos\left(K_1 \cdot d_{A-plate}\right) - L_1 = \left(S_{1\_P} + S_{1\_A}\right)/2, \tag{3.8}$$

where constants $H_1$, $K_1$, and $L_1$ depend on the polarizer thickness and the refractive indices of the polarizer and A-plate film. Finally, from Equation 3.8 we obtain $d_{A\text{-}plate}$ in the form of

$$d_{A-plate} = \frac{1}{K_1} \cdot \arccos\left(\frac{\left(S_{1\_P} + S_{1\_A}\right)/2 + L_1}{H_1}\right). \tag{3.9}$$

To design C-plate film, we first note that for the optimum design, **B** satisfies conditions $S_{1\_B} = S_{1\_A}$ and $S_{3\_B} = S_{3\_A}$. Similarly, we can find $E_{//\_B}$ and $E_{\perp\_B}$ (after the 2nd A-plate film) in terms of the C-plate thickness ($d_{C\text{-}plate}$). Next, applying $S_{1\_B} = S_{1\_A}$ yields

$$\frac{\left(\left|E_{//\_B}\right|^2 - \left|E_{\perp\_B}\right|^2\right)}{\left(\left|E_{//\_B}\right|^2 + \left|E_{\perp\_B}\right|^2\right)} = S_{1\_A}. \tag{3.10}$$

After simplifying Equation 3.10 we derive the following expression

$$H_2 \cdot \cos\left(K_2 \cdot d_{C-plate}\right) + L_2 \cdot \sin\left(K_2 \cdot d_{C-plate}\right) = S_{1\_A}, \tag{3.11}$$

where constants $H_2$, $K_2$, and $L_2$ depend on the thickness of polarizer, A-plate film, LC cell gap and the refractive indices of polarizer, A-plate film, C-plate film, and LC material. Finally, from Equation 3.11 we can find the thickness of each C-plate film $d_{C\text{-}plate}$.

Now we apply the above methodology to design a VA-LCD shown in Figure 3.1. The employed refractive indices of the polarizers, liquid crystal, A-plate, and C-plate are as follows: $n_{e\_pol} = 1.5 + i\times 3.251\times 10^{-3}$ and $n_{o\_pol} = 1.5 + i\times 2.86\times 10^{-5}$, $n_{e\_LC} = 1.5514$ and $n_{o\_LC} = 1.4737$ at $\lambda = 550$ nm, $n_{e\_A\text{-}plate} = 1.5124$ and $n_{o\_A\text{-}plate} = 1.5089$, and $n_{e\_C\text{-}plate} = 1.5089$ and $n_{o\_C\text{-}plate} = 1.5124$. The thickness of the polarizer is 150 μm and LC cell gap is 4 μm.

We designed the compensation films at $\theta = 70^o$, $\phi = 45^o$, and $\lambda = 550$ nm. From Equation 3.9 we find the A-plate thickness $d_{A\text{-}plate}$ =26.62 μm and the $d\Delta n$ of each A-plate film is 93.17 nm. Using Equation 3.11, we find the thickness of each C-plate film $d_{C\text{-}plate} = 21.54$ μm. Therefore, the $d\Delta n$ of each C-plate film is −75.39 nm. With this design, in the dark state the polarization state in front of the analyzer equals to the polarization state absorbed by the analyzer at $\theta = 70^o$ and $\phi = 45^o$. Therefore, contrast ratio higher than 10,000:1 over ±85° viewing cone is achieved, as shown in Figure 3.5. The above ideal simulation results are obtained using the four-by-four matrix method [39]. In a real display panel, the actual contrast ratio could be lowered because the abovementioned ideal parameters may not be controlled precisely. Moreover, the compensation film thickness variation and nonuniformity, LC alignment distortion near spacer balls, stress birefringence from films and substrates, and interface reflections between layers could also reduce the contrast ratio.

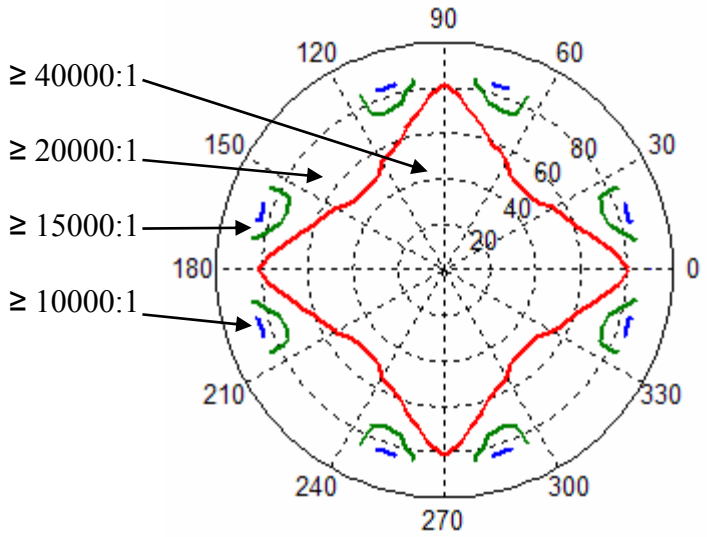


Figure 3.5: Iso-contrast ratio plot of the four-domain VA LCD with optimal compensation films optimized at $\theta = 70^{o}$ and $\phi = 45^{o}$.

## 3.4. Design tolerance

Design tolerance is an important concern for display manufacturing. Figure 3.6 plots the minimum contrast ratio over the entire $\pm 85^{o}$ viewing cone if the $d\Delta n$ of A-plate film, C-plate film, and LC cell varies by ±5%, assuming the compensation films are optimized at $\theta = 70^{o}$ and $\phi = 45^{o}$. From Figure 3.6, the proposed VA-LCD is less sensitive to the $d\Delta n$ variation of the C-plate but more sensitive to the $d\Delta n$ variation of the LC cell. In the least favorable case (i.e., the LC $d\Delta n$ is 5% higher than the optimal value), the minimum contrast ratio is still higher than 100:1.

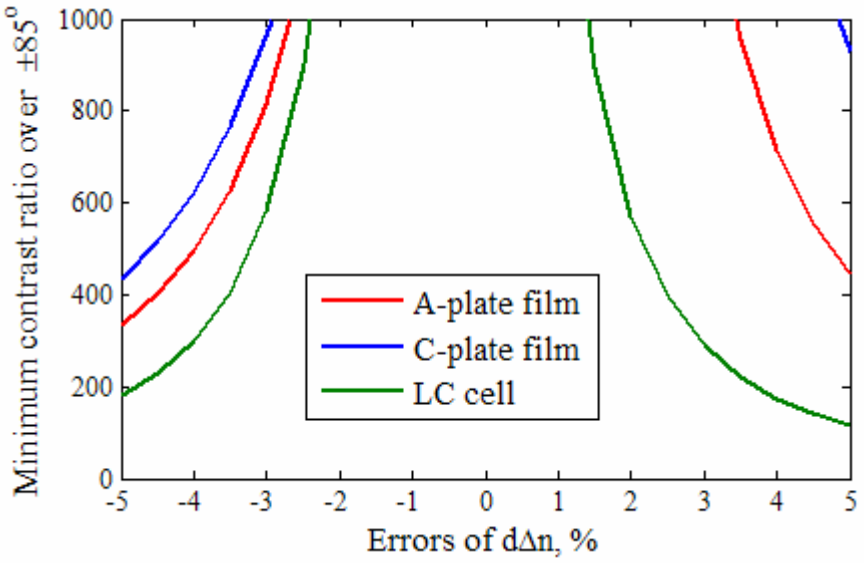


Figure 3.6: Tolerance in the errors of $d\Delta n$ of A-plate film, C-plate film, and LC cell when the compensation films are optimized at $\theta = 70^{o}$ and $\phi = 45^{o}$.

## 3.5. Summary

In this chapter, we demonstrate a wide view VA LCD with a superb contrast ratio. We use Poincaré sphere method to obtain the optimal compensation film parameters and then use 4-by-4 matrix method to calculate and plot the iso-contrast contours. In the proposed design, a contrast ratio higher than 10,000:1 is predicted over the entire ±85° viewing cone for the film-compensated four-domain VA LCD. The tolerance of the design is also investigated. Within ±5% manufacturing margin, the contrast ratio maintains higher than 100:1.

# CHAPTER FOUR: WIDE VIEW AND BROAD BAND CIRCULAR POLARIZERS CONSISTING OF UNIAXIAL PHASE RETARDATION FILMS

Circular polarizer is an important optical component with many useful applications, such as optical communications, optical remote sensors, and liquid crystal displays (LCDs) [23-25]. Two methods have been commonly applied to generate a circularly polarized light: Bragg reflection using a cholesteric liquid crystal (CLC) film and a linear polarizer laminated with a quarter-wave film. In the former approach, a right-handed CLC film would reflect the right-handed circularly polarized light and transmit the left-handed component [1-2, 43]. A drawback is that blue shift occurs at oblique incident angles. In the latter approach a quarter-wave film is laminated to a linear polarizer [41-42]. In the normal incidence, a very good circular polarization is produced. However, at oblique angles the produced state of polarization becomes elliptical resulting in light leakage through the crossed circular polarizers. Wide-view circular polarizers using biaxial retardation films have been proposed for improving the light efficiency of LCDs [24-25]. However, the reported contrast ratio is limited to ~10:1 at $60^{o}$ viewing cone because of the still large light leakage. In addition, broad bandwidth is as important as wide viewing angle for direct-view LCDs.

Phase compensation methods have been widely applied in liquid crystal displays for reducing the dark state light leakage and thus increasing the contrast ratio at wide viewing angles [1, 6-9, 11-15]. To obtain a wide-view circular polarizer, a straightforward approach is to

combine a wide-view linear polarizer [11-15] with a wide-view quarter-wave film [24-25]. However, this approach is difficult to obtain a pure circular polarization state, especially at a large incident angle. In this chapter, we apply the phase compensation methods to develop wide-view circular polarizers for both single wavelength and broadband white light [26]. The produced state of polarization is very close to the ideal circular state of polarization over a wide range of incident angles. Over the entire ±85$^{o}$ viewing cone, after reducing the air-interface surface reflection, the light leakage from the crossed single-wavelength circular polarizers is less than $2.87\times10^{-4}$ at $\lambda$ = 550 nm and less than $1.7\times10^{-3}$ over the 450~650 nm spectrum for the crossed broadband circular polarizers. This device is particularly useful for enhancing the optical efficiency of direct-view LCDs.

## 4.1. Stokes parameters

The state of polarization can be represented by Stokes parameters ($S_1$, $S_2$, and $S_3$) and plotted on Poincaré sphere [41-42] after the parallel and perpendicular components of the electric field are solved using the 4-by-4 matrix method [39]. If the state of polarization is represented by vector $\mathbf{P} = (S_1, S_2, S_3)$, then the polarization difference between two states of polarization $\mathbf{P}_{(1)}$ and $\mathbf{P}_{(2)}$ can be described by

$$\Delta\mathbf{P}_{(1)-(2)} = \sqrt{\left(S_{1\_(1)} - S_{1\_(2)}\right)^2 + \left(S_{2\_(1)} - S_{2\_(2)}\right)^2 + \left(S_{3\_(1)} - S_{3\_(2)}\right)^2}\,, \tag{4.1}$$

where $S_{1\_(1)}$, $S_{2\_(1)}$, $S_{3\_(1)}$, $S_{1\_(2)}$, $S_{2\_(2)}$, and $S_{3\_(2)}$ are the Stokes parameters of $\mathbf{P}_{(1)}$ and $\mathbf{P}_{(2)}$, respectively. $\mathbf{P}_{(LCP)} = (0, 0, 1)$ denotes the left-handed circular polarization and $\mathbf{P}_{(RCP)} = (0, 0, -1)$

gives the right-handed circular polarization. $S_3$ equals to zero for the linear polarization and $|S_3|$ is neither zero nor one for the elliptical polarization. Since $S_1$, $S_2$ and $S_3$ satisfy the relationship that $S_1^2 + S_2^2 + S_3^{\,2} = 1$, Equation 4.1 can be simplified so that the polarization difference between $\mathbf{P}_{(X)}$ and $\mathbf{P}_{(RCP)}$ is related to the $S_3$ of $\mathbf{P}_{(X)}$ by

$$\Delta\mathbf{P}_{(X)-(RCP)} = \mathbf{P}_{(X)} - \mathbf{P}_{(RCP)} = \sqrt{2\left(1 + S_{3\_(X)}\right)}, \tag{4.2}$$

where $\mathbf{P}_{(X)} = (S_{1\_(X)}, S_{2\_(X)}, S_{3\_(X)})$. Once $S_{3\_(X)}$ descents to $-1$, $\Delta\mathbf{P}_{(X)-(RCP)}$ approaches zero and $\mathbf{P}_{(X)}$ becomes $\mathbf{P}_{(RCP)}$.

In this chapter, the linear polarizer is modeled as a lossy uniaxial material. The employed refractive indices of the polarizer, positive birefringence uniaxial A-plate and C-plate, and negative birefringence uniaxial A-plate and C-plate are as follows: $n_{e\_pol} = 1.5 + i\times3.251\times10^{-3}$, $n_{o\_pol} = 1.5 + i\times2.86\times10^{-5}$, $n_{e\_p\_A\text{-}plate} = 1.\ 5124$, $n_{o\_p\_A\text{-}plate} = 1.5089$, $n_{e\_p\_C\text{-}plate} = 1.5124$, $n_{o\_p\_C\text{-}plate} = 1.5089$, $n_{e\_n\_A\text{-}plate} = 1.5089$, $n_{o\_n\_A\text{-}plate} = 1.\ 5124$, $n_{e\_n\_C\text{-}plate} = 1.5089$, and $n_{o\_n\_C\text{-}plate} = 1.5124$. The thickness of the polarizer is 210 μm. The A-plate and C-plate with negative $d\Delta n$ can be realized by negative birefringence A-plate and C-plate. We assume the color dispersions of linear polarizer, A-plate, and C-plate are negligible.

On both sides of the absorptive polarizer, the protective Tri-Acetyl-Cellulose (TAC) films exhibit a small birefringence and act as negative birefringence C-plates. The phase change due to the TAC film can be minimized if we laminate a positive birefringence C-plate to the exit protective film. The phase retardation of this C-plate compensates for the adjacent protective film so that the C-plate effect of the linear polarizer is negligible.

## 4.2. Single-wavelength wide-view circular polarizers

A conventional circular polarizer consists of a linear polarizer and a quarter-wave plate. The quarter-wave plate is laminated on the light emerging side of the linear polarizer and its slow axis is oriented at $45^{o}$ with respect to the absorption direction of the polarizer. At normal incidence, the light emerging from the linear polarizer sustains $\pi/2$ phase change from the quarter-wave plate so that it becomes circularly polarized light. However, at oblique angles, the phase change contributed by the $\lambda/4$ plate is different from $\pi/2$ [24-25] so that the produced polarization state becomes elliptical as Figure 4.1(a) illustrates.

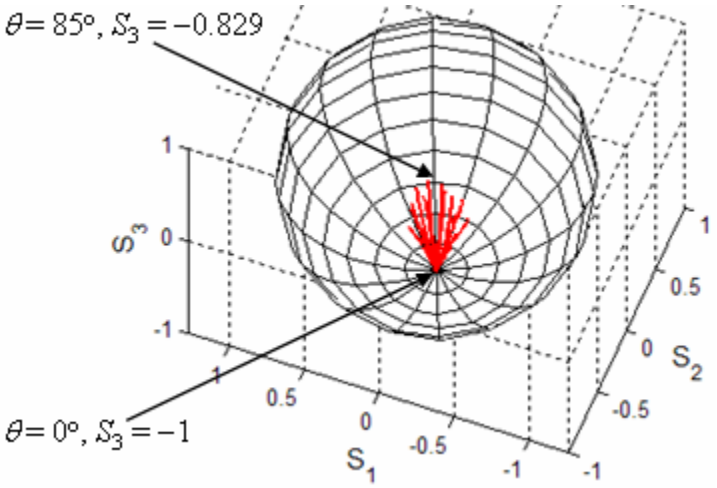


(a)

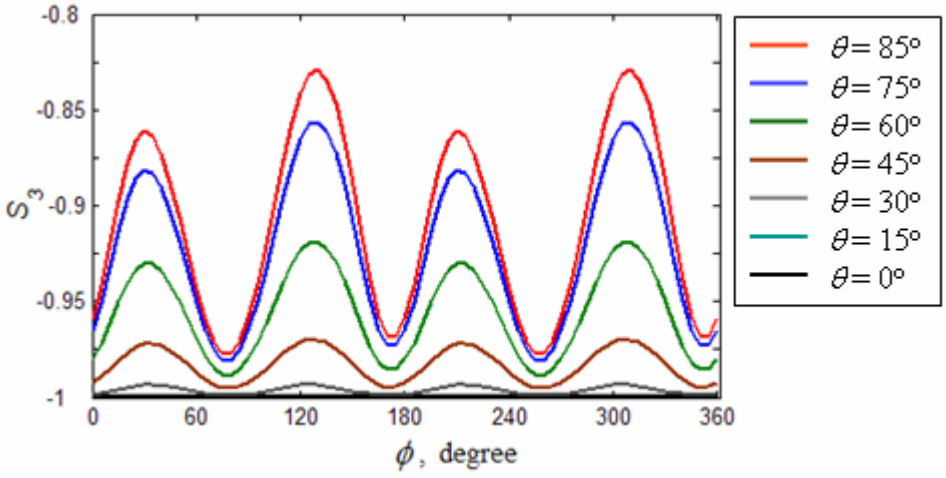


(b)

Figure.4.1: (a) States of polarization produced by a conventional circular polarizer. The red lines show the states of polarization for $\theta = 0^o \sim 85^o$ at each fixed $\phi$, where $\phi = 0^o \sim 360^o$ with $10^o$ interval. (b) $S_3$ of the produced states of polarization at different view angles. $S_3 = -1$ at normal incidence angle and reaches its maximum of $-0.829$ at $\theta = 85^o$, $\phi = 130^o$ and $310^o$. In both figures, $\lambda = 550$ nm.

In Figure 4.1(a), the $S_3$ of the produced polarization increases from –1 to –0.829 ($\Delta\mathbf{P}_{(\lambda/4)-(\mathrm{RCP})} = 0.585$) when the incident angle $\theta$ increases from $0^o$ to $85^o$ at $\phi = 130^o$ and $320^o$. Figure 4.1(b) plots the variation in the produced $S_3$ with respect to the incident angle $\theta$ and the azimuth of incident plane $\phi$. The variation in $S_3$ is relatively small when the incident angle is within $30^o$. Above $45^o$, $S_3$ increases drastically. The peaks of $S_3$ occur at $\phi = 40^o$, $130^o$, $220^o$, and $320^o$.

If a pair of crossed circular polarizers is constructed as Figure 4.2(a) depicts, the polarizer and the first quarter-wave plate form a circular polarizer, and the analyzer and the second quarter-wave plate form a crossed circular polarizer. Figure 4.2(b) plots the iso-transmittance contour of light leakage. Although the light leakage is almost zero at normal viewing direction, it increases to 0.098 at $\theta = 85^o$ because of the resulted elliptical polarization. The light leakage is the strongest at near bisectors ($\phi = 40^o$, $130^o$, $220^o$, and $320^o$) since the produced $S_3$ peaks at these angles, as depicted in Figure 4.1(b).

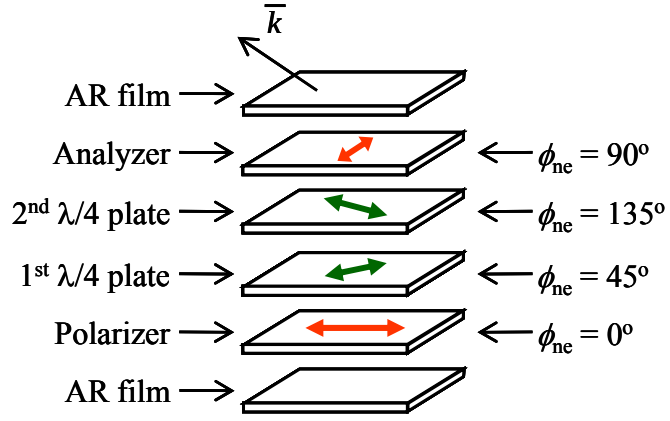


(a)

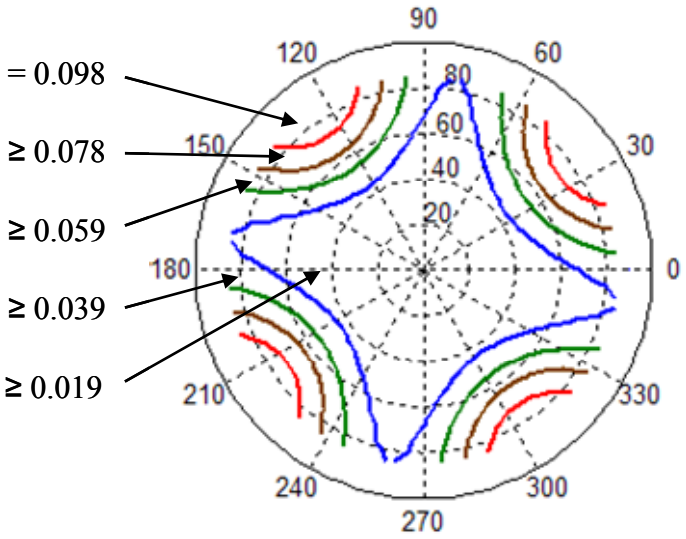


(b)

Figure 4.2: Conventional crossed circular polarizers: (a) device configuration; (b) iso-transmittance contour showing the light leakage at $\lambda$ = 550 nm. Ten-layer anti-reflection film is assumed.

During simulations, an ideal anti-reflection (AR) film is assumed in order to reduce the interference of the air-polarizer surface reflection. The ten-layer anti-reflection film is coated on the air interface of both polarizers. This AR film is designed using genetic algorithm [44-45] and the gradient refractive indices profile is illustrated in Figure 4.3(a). The origin represents the air-AR interface. The transmittance of this ten-layer AR film is greater than 0.97 over the $\pm 85^{o}$ incident cone for $\lambda = 450 \sim 650$ nm as Figure 4.3(b) illustrates.

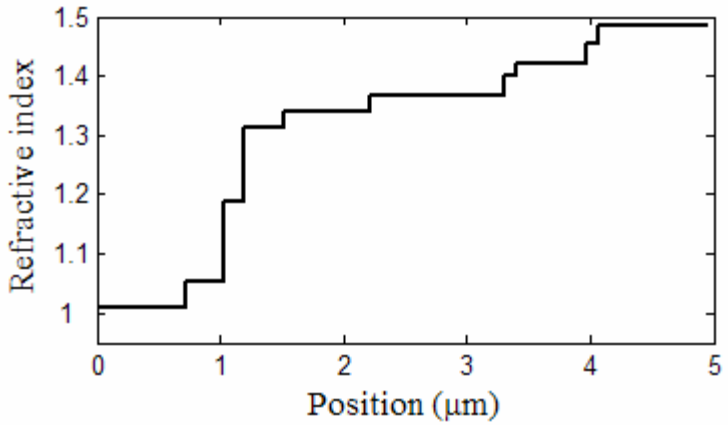


(a)

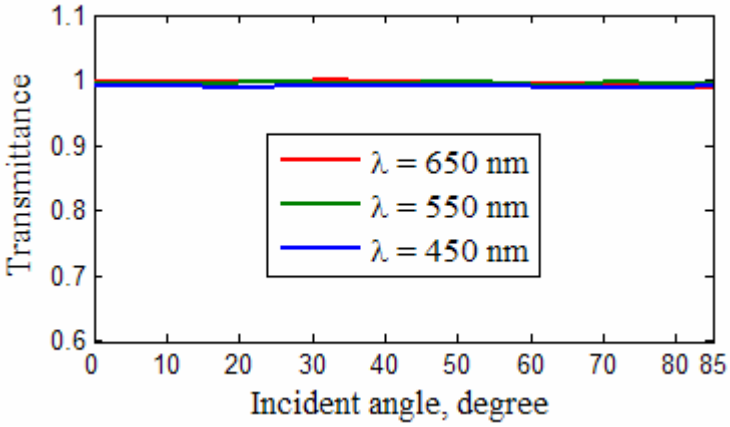


(b)

Figure 4.3: Ten-layer anti-reflection film: (a) refractive indices profile, and (b) transmittance.

To produce circular state of polarization at a large incidence angle, we laminate one uniaxial C-plate to the quarter-wave plate as Figure 4.4 drafts. This positive birefringence C-plate contributes phase retardation at oblique angles [1, 6, 9, 14-16] so that the produced polarization is closer to an ideal circular polarization, while the normal incidence angle performance of conventional circular polarizer is not compromised.

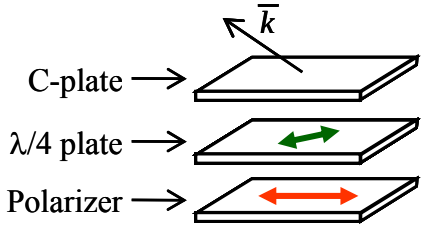


Figure 4.4: Configuration of a wide-view circular polarizer with a linear polarizer, a quarter-wave plate, and a uniaxial C-plate.

Figure 4.5(a) uses Poincaré sphere to demonstrate how the C-plate with $d\Delta n$ = 59.9 nm reduces the $S_3$ of the produced polarization to –0.952 at $\theta$ = 85°. Although the state of polarization emerging from the quarter-wave plate is deviated from an ideal circular polarization, the C-plate reduces the difference by modifying the transmitted $S_2$ and $S_3$.

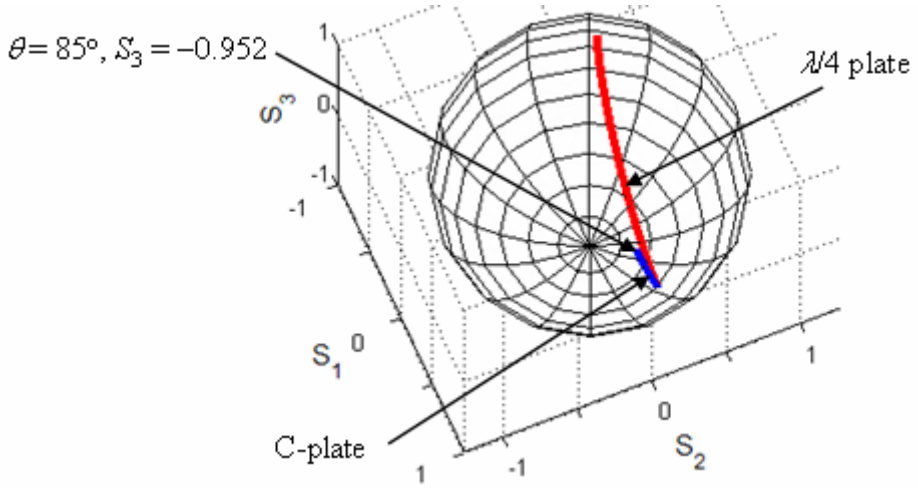


(a)

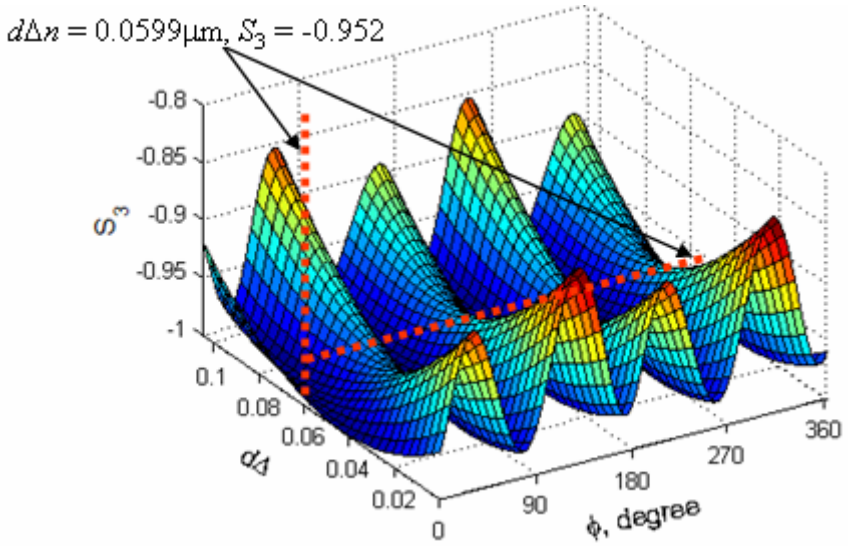


(b)

Figure 4.5: (a) States of polarization inside a wide-view circular polarizer when $d\Delta n$ of C-plate equals 59.9 nm, where $\theta = 85^{o}$, $\phi = 130^{o}$, and $\lambda = 550$nm. (b) Variations in the produced $S_3$ with respect to the $d\Delta n$ of C-plate when $\theta = 85^{o}$. The configuration of this circular polarizer is shown in Figure 4.4.

To find the $d\Delta n$ of this C-plate for minimizing $S_3$ over the ±85° viewing cone, Figure 4.5(b) illustrates that the produced $S_3$ decreases to its minimum when the $d\Delta n$ of the C-plate is gradually increased from 0 to 59.9 nm. Further increasing the $d\Delta n$ of the C-plate increases the produced $S_3$. By exhaustive search we can find when the $d\Delta n$ of the C-plate equals 59.90 nm, the $S_3$ of the produced state of polarization is less than −0.952 ($\Delta\mathbf{P}_{(\lambda/4+1C)-(RCP)} \leq 0.31$) over the entire ±85° viewing cone as Figure 4.6(a) shows. Due to this additional C-plate, the produced $S_3$ remains −1 at normal incidence and slowly increases to −0.952 as the viewing angle increases to 85°, which is significantly reduced in contrast to a conventional circular polarizer. This decreases the light leakage of the crossed circular polarizers to 0.027 over the ±85° viewing cone, as demonstrates in Figure 4.6(b). The peaks of light leakage shift to $\phi$ = 55°, 145°, 235°, and 325° due to the presence of the C-plate. Ten-layer ideal anti-reflection film in Figure 4.3(a) is assumed and coated on the air interface of both polarizers.

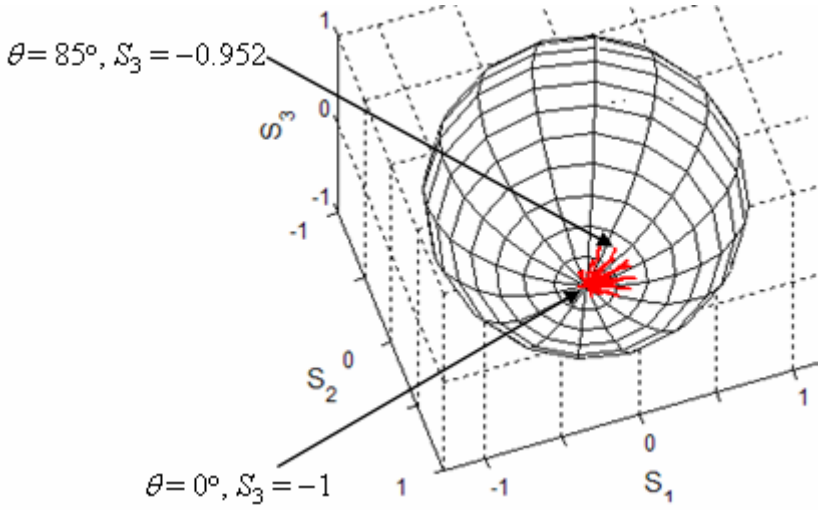


(a)

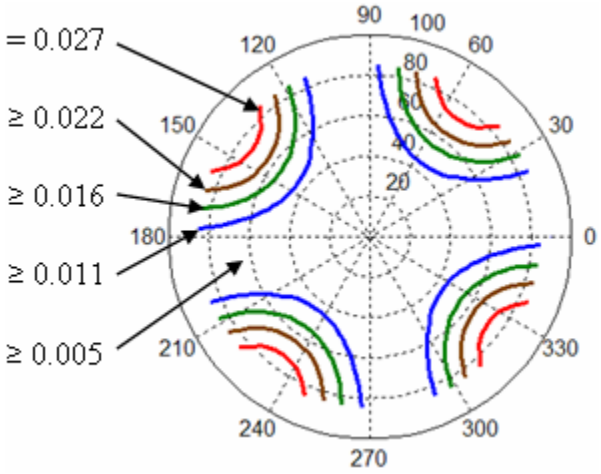


(b)

Figure 4.6: (a) States of polarization emerging from a wide-view circular polarizer when the $d\Delta n$ of C-plate equals 59.9 nm, red lines show the states of polarization when $\theta = 0^{o} \sim 85^{o}$ at each fixed $\phi$, where $\phi = 0^{o} \sim 360^{o}$ with $10^{o}$ interval. (b) iso-transmittance contour showing the light leakage from the crossed wide-view circular polarizers. The configuration of this circular polarizer is shown in Fig. 4. Ten-layer anti-reflection film is assumed and $\lambda = 550$ nm.

Since the C-plate does not change the $S_1$ of the polarization state [16], the produced $S_3$ remains as high as –0.952 at 85$^o$ viewing angle and cannot be further reduced as we observed in Figures 4.5 and 4.6. Whereas all of the three Stokes parameters are changed inside an A-plate [16], to further improve the viewing angle performance we could laminate an extra A-plate to the circular polarizer shown in Figure 4.4 and obtain a new design shown in Figure 4.7. The C-plate is laminated between two A-plates. Over wide incident angles, the combination of these A-plates and C-plate is expect to be equivalent to the quarter-wave plate in the conventional circular polarizer at normal incidence. Due to the presence of the additional A-plate, the azimuthal angle and the $d\Delta n$ of the quarter-wave plate must be redesigned so that the produced state of polarization remains circular at normal incidence. The azimuthal angles of both A-plates as well as the $d\Delta n$ of all A-plates and C-plate are the subject of design. Using genetic algorithm [44-45], by minimizing the cost function

$$\cos t = \max\left\{\sqrt{2\left(S_{3\_(2A+1C)}+1\right)} \mid \left(\theta = 0^0 \sim 85^0, \phi = 0^0 \sim 360^0\right)\right\}, \tag{4.3}$$

where $S_{3\_(2A+1C)}$ is the $S_3$ of the produced state of polarization $\mathbf{P}_{(2A+1C)}$, we obtain the parameters of the phase retardation films. For this design, the azimuthal angles of A-plates are: $\phi_{ne\_A\_1st}$ = 72.36$^o$ and $\phi_{ne\_A\_2nd}$ = 36.84$^o$; the $d\Delta n$ of all retardation films are: $d\Delta n_{\_A\_1st}$ = 89.77 nm, $d\Delta n_{\_A\_2nd}$ = 89.77 nm, and $d\Delta n_{\_C}$ = 106.08 nm.

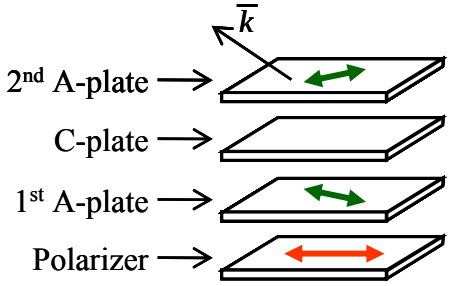


Figure 4.7: Configuration of a wide-acceptance-angle circular polarizer with one linear polarizer, two uniaxial A-plates, and one uniaxial C-plate.

Inside this circular polarizer, all of the $S_1$, $S_2$ and $S_3$ are modified so that the compensations between the retardation films are further improved as Figure 4.8(a) demonstrates. The two A-plates not only reduce $S_3$ to $-1$ but also reduce the transmitted $S_1$ and $S_2$ to zero. On the other hand, the C-plate tempers the transmitted state of polarization to further reduce the viewing angle sensitivity. Therefore, the produced $S_3$ is only slightly increased to $-0.991$ when the viewing angle increases to $85^o$ as depicted in Figure 4.8(b). This is equivalent to having the polarization difference $\Delta\mathbf{P}_{(2A+1C)-(RCP)}$ less than 0.134 over the $\pm 85^o$ viewing cone. The produced $S_3$ remains at $-1$ at normal angle as in the conventional right-handed circular polarizer. For the left-handed circular polarizer using the configuration shown in Figure 4.7, the $d\Delta n$ of all A-plates and C-plate are not changed but the azimuthal angles of the A-plates are the negative of their counterparts in the right-handed circular polarizer.

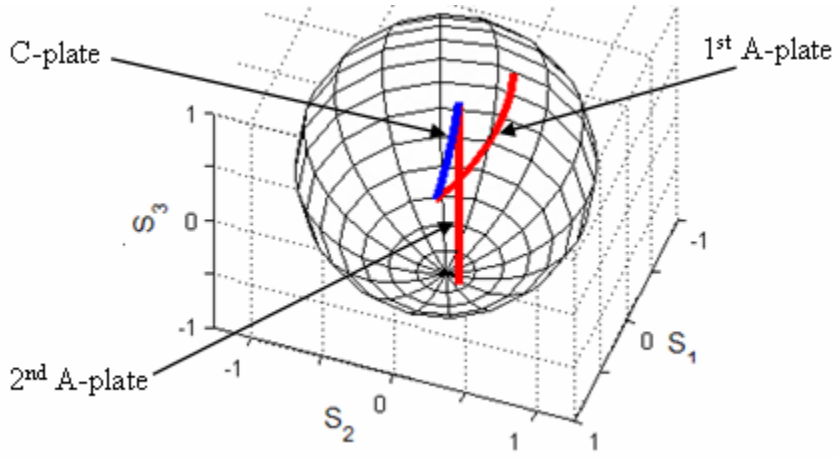


(a)

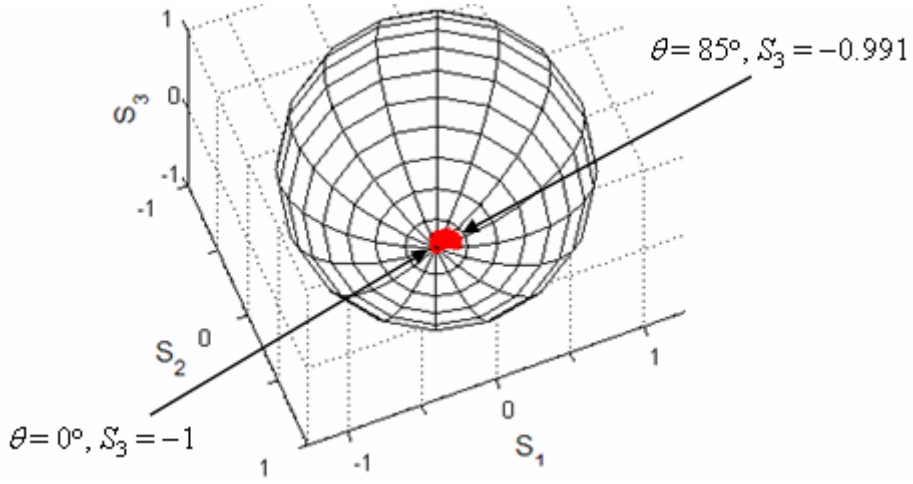


(b)

Figure 4.8: (a) States of polarization inside a wide-view circular polarizer at $\theta = 85^{o}$ and $\phi = 130^{o}$. Red and blue lines show the states of polarization inside the A-plates and C-plates, respectively. (b) State of polarization emerging from a wide-view circular polarizer. Red lines show the states of polarization when $\theta = 0^{o} \sim 85^{o}$ at each fixed $\phi$, where $\phi = 0^{o} \sim 360^{o}$ with $10^{o}$ interval. In both figures, the configuration of the circular polarizer is in Figure 4.7. $\lambda = 550$ nm.

From above discussions, an extra phase retardation film gives an extra degree of freedom to improve the viewing angle of a circular polarizer. By laminating an additional A-plate and a C-plate to the above circular polarizer as Figure 4.9 depicts, the polarization difference between the produced polarization and the desired circular polarization can be further reduced. In this configuration, A-plates are interlaced with C-plates. By minimizing the cost $\sqrt{2\left(S_{3\_(3A+2C)}+1\right)}$ over the ±85° viewing cone using genetic algorithm [44-45], we obtain the design parameters of A-plates and C-plates, where $S_{3\_(3A+2C)}$ is the $S_3$ of the produced state of polarization $\mathbf{P}_{(3A+2C)}$. From this design, the azimuthal angles of A-plates are: $\phi_{ne\_A\_1st} = 78.55^{o}$, $\phi_{ne\_A\_2nd} = -28.71^{o}$, and $\phi_{ne\_A\_3rd} = 42.46^{o}$; the $d\Delta n$ of all retardation films are: $d\Delta n_{\_A\_1st} = 75.69$ nm, $d\Delta n_{\_A\_2nd} = 24.30$ nm, $d\Delta n_{\_A\_3rd} = 128.96$ nm, $d\Delta n_{\_C\_1st} = 106.56$ nm, and $d\Delta n_{\_C\_2nd} = -21.08$ nm.

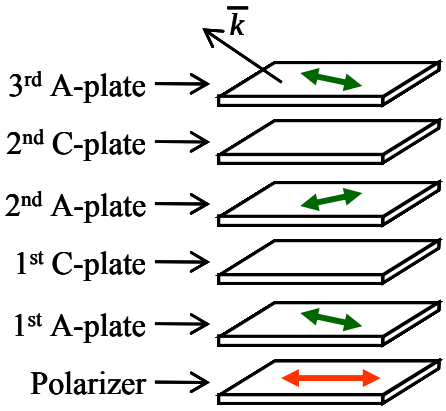


Figure 4.9: Configuration of a wide-view circular polarizer with one linear polarizer, three uniaxial A-plates and two uniaxial C-plates.

The additional A-plate and C-plate significantly reduce the viewing angle sensitivity of the circular polarizer because of the extra compensations between retardation films. As illustrated in Figure 4.10(a), all of the $S_1$, $S_2$ and $S_3$ are subtly modified in the retardation films so that the produced $S_3$ remains less than $-0.999$ ($\Delta\mathbf{P}_{(3A+2C)-(RCP)} \leq 0.045$) over the entire $\pm 85^{o}$ viewing cone, which can be seen in Figure 4.10(b). Variation in the produced $S_3$ is further reduced so that the produced polarization is nearly circular at any incident angle within $\pm 85^{o}$.

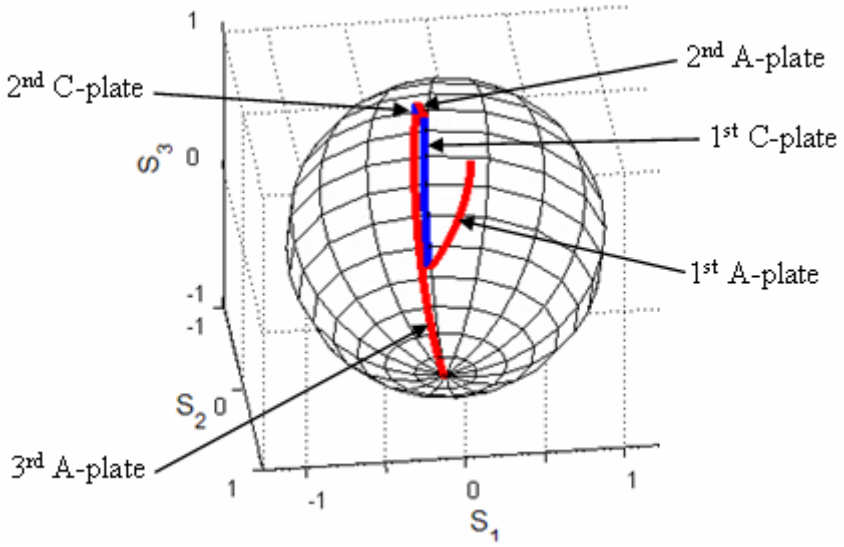


(a)

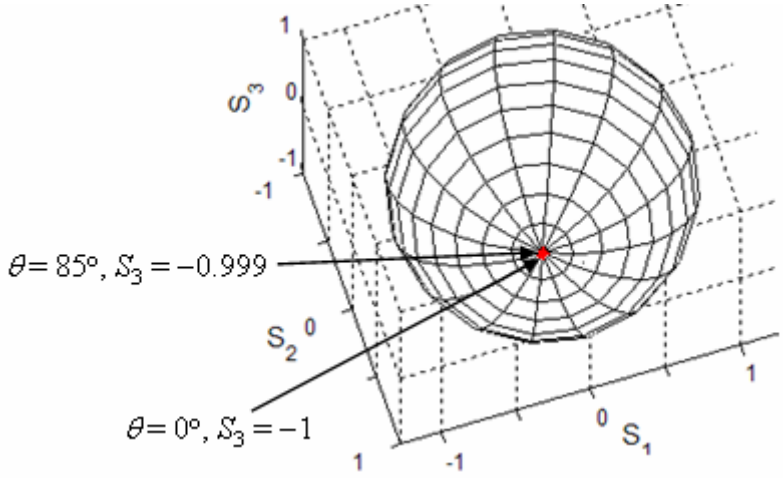


(b)

Figure 4.10: (a) States of polarization inside a wide-view circular polarizer at $\theta = 85^{o}$ and $\phi = 130^{o}$. Red and blue lines show the polarizations inside A-plates and C-plates, respectively. (b) State of polarization emerging from a wide-view circular polarizer. Red lines show the polarizations when $\theta = 0^{o} \sim 85^{o}$ at each fixed $\phi$, where $\phi = 0^{o} \sim 360^{o}$ with $10^{o}$ interval. In both figures, the configuration of the circular polarizer is shown in Figure 4.9. $\lambda = 550$ nm.

Since the produced polarization approaches the ideal circular polarization, the light leakage of the crossed circular polarizers is less than $2.87\times10^{-4}$ over the $\pm85^{o}$ viewing cone as Figure 4.11(a) shows. Although the light leakage is more pronounced at $\phi \sim 10^{o}$, $100^{o}$, $190^{o}$, and $280^{o}$, it is still less than $1.72\times10^{-4}$ at other azimuthal angles when the incident angle is within $\pm85^{o}$. As compared to the case of using conventional circular polarizer, as shown in Figure 4.2(b), our results are significantly improved despite the increased cost.

Figure 4.11(b) depicts the configuration of the crossed circular polarizers. The polarizer and the first three A-plates together with the first two C-plates form a wide-view right-handed circular polarizer. The analyzer and the last three A-plates together with the last two C-plates form a second circular polarizer crossed to the first one. The arrangement of the A-plates and C-plates are reversed for the crossed polarizers so that the state of polarization emerging from the last A-plate is linear along the absorption direction of the analyzer, thus the light leakage is small. The ideal anti-reflection film in Figure 4.3(a) is assumed and coated on the air interface of both polarizers. For a left-handed circular polarizer using the configuration in Figure 4.9, the $d\Delta n$ of all A-plates and C-plates are not changed but the azimuthal angles of the A-plates are the negative of their counterparts in the right-handed circular polarizer.

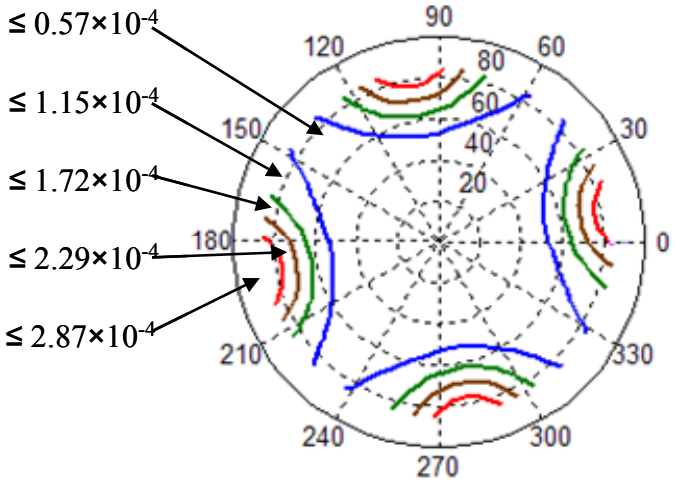


(a)

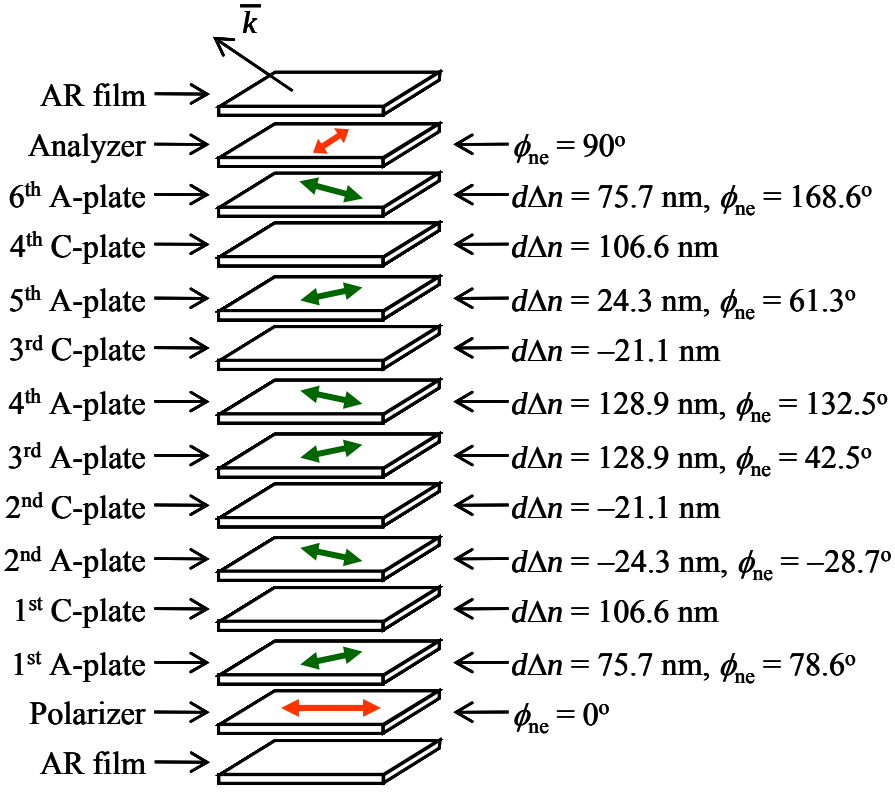


(b)

Figure 4.11: Crossed wide-view circular polarizers: (a) iso-transmittance contour showing the light leakage at $\lambda = 550$ nm; (b) device configuration. The ideal anti-reflection film is assumed.

## 4.3. Broadband wide-view circular polarizers

In the above designs, the produced states of polarization are very close to the ideal circular polarization over a wide viewing cone, however, only at a single wavelength. As the incident wavelength deviates from the designed one, the phase retardations of the A-plates and C-plates will walk off from the designed values. As a result, the produced polarization state is no longer circular as Figure 4.12 demonstrates. In Figure 4.12, the conventional broadband circular polarizer (red line) is indeed quite insensitive to the wavelength in the 450-650 nm spectral range, but only at normal incident angle. All the other three designs (black, blue and green curves) based on a single wavelength are rather sensitive to the wavelength. In this section we will focus on the designs of broadband and wide-view circular polarizers.

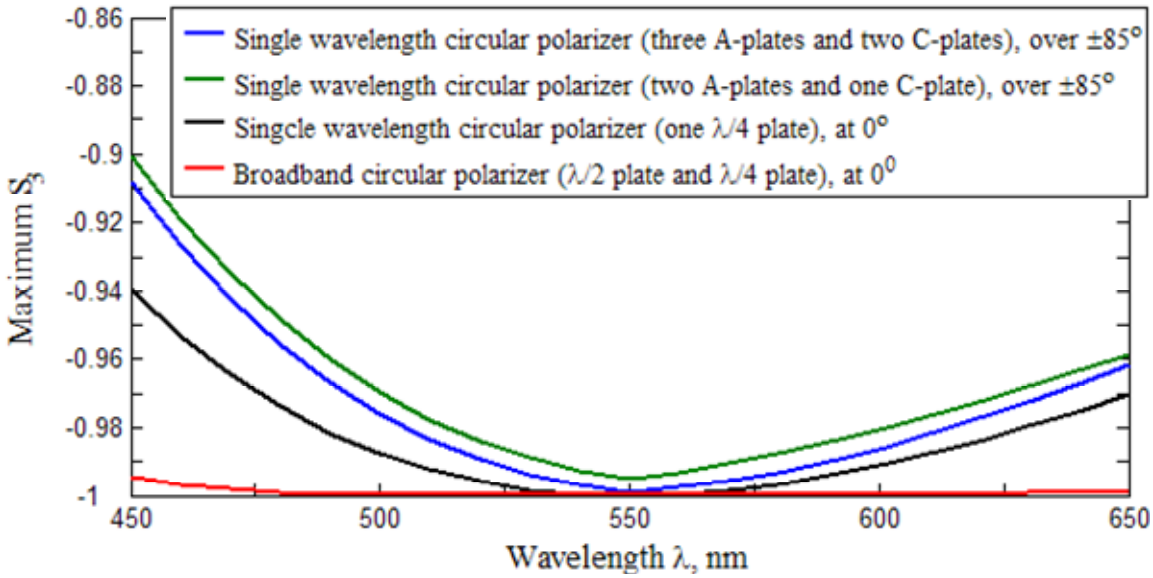


Figure 4.12: The calculated $S_3$ as a function of wavelength for the four types of circular polarizers, as described in the insert. The viewing cone is ±85° for the proposed wide-view circular polarizers, and the viewing angle is 0° for the conventional circular polarizers.

A commonly used broadband circular polarizer is comprised of laminating a half-wave plate between the linear polarizer and the quarter-wave plate as illustrated in Figure 4.13(a) [46, 47]. When the azimuthal angles of the half-wave plate and the quarter-wave plate satisfy the following relationship

$$2\theta_{ne\_\lambda/4} - 4\theta_{ne\_\lambda/2} = 90^0, \tag{4.4}$$

the produced state of polarization is very close to the ideal circular polarization over a broad spectrum at normal incidence as observed from Figure 4.12. However, at oblique angles, the relationship in Equation 4.4 is no longer satisfied on the wave plane and the phase retardations of the half-wave plate and the quarter-wave plate are changed. Thus, the produced polarization is no

longer circular and varies significantly with the incident spectrum [24-25]. As Figure 4.14 shows, the produced $S_3$ from a conventional broadband circular polarizer (black curve) is larger than –0.5 at 85° incident angle over the spectrum of 450 ~ 650 nm. The red line in Figure 4.14 shows the produced $S_3$ from a broadband wide-view circular polarizer that we are going to discuss.

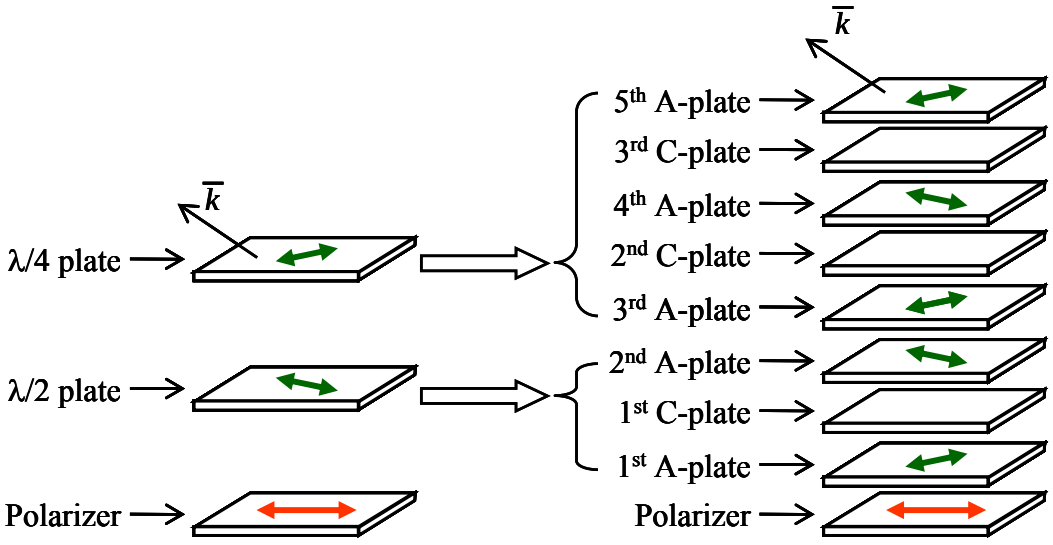


(a) (b)

Figure 4.13: (a) Configuration of a conventional broadband circular polarizer with one linear polarizer, one half-wave plate and one quarter-wave plate. The azimuthal angle of the half-wave plate is 75° with respect to the absorption axis of the polarizer and the azimuthal angle of the quarter-wave plate is 15°. (b) Device configuration of a wide-view broadband circular polarizer with one linear polarizer, five uniaxial A-plates and three uniaxial C-plates.

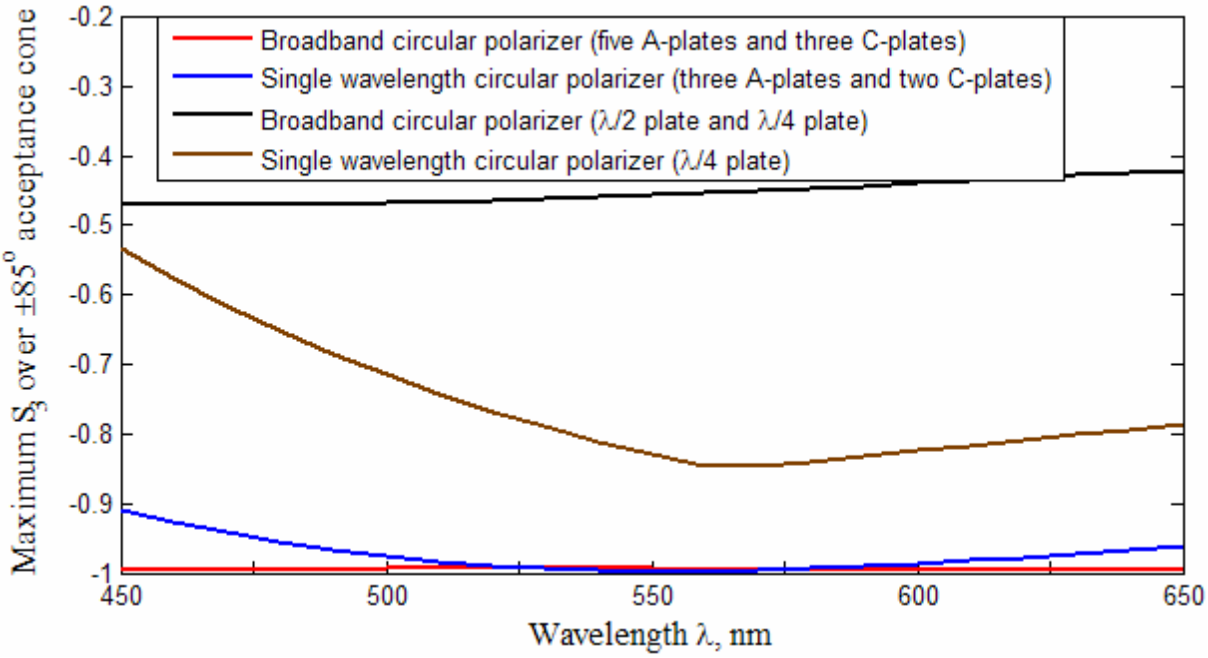


Figure 4.14: The calculated maximum $S_3$ over the $\pm 85^o$ viewing cone as a function of wavelength for the four types of circular polarizers, as described in the insert.

The above designs of single-wavelength circular polarizer show that replacing the quarter-wave plate in the conventional circular polarizer with the combination of A-plates and C-plates significantly reduces the viewing angle sensitivity of the produced state of polarization. Likewise, if both half-wave plate and quarter-wave plate in the conventional broadband circular polarizer can be replaced by multi-layer equivalent plates, then the resulted circular polarizer would be broadband and wide-view. In this case, over wide viewing angle and broad spectrum, the multi-layer equivalent plates should produce similar states of polarization as their single-layer counterparts do at normal incidence.

To design the multi-layer equivalent half-wave plate, we first derive the states of polarization $\mathbf{P}_{\lambda/2}$ emerging from the half-wave plate at $\theta = 0^o$ and $\phi = 0^o \sim 360^o$ for $\lambda = 450 \sim 650$

nm. Then we use the combination of two A-plates and one C-plate to replace the half-wave plate as Figure 4.13(b) depicts. Next, by using genetic algorithm to minimize the cost

$$\cos t = \max\left\{\Delta\mathbf{P}_{(2\text{A}+1\text{C}\_\lambda\_2)-(\lambda/2)} \mid \left(\theta = 0^0 \sim 85^0, \phi = 0^0 \sim 360^0, \lambda = 450\,\text{nm} \sim 550\,\text{nm}\right)\right\}, \quad (4.5)$$

we find the phase retardation film parameters, where $\Delta\mathbf{P}_{(2\text{A}+1\text{C}\_\lambda/2)-(\ \lambda/2)}$ is the polarization difference between the state of polarization $\mathbf{P}_{(2\text{A}+1\text{C}\_\lambda/2)}$ emerging from the equivalent $\lambda/2$ plate and the state of polarization $\mathbf{P}_{\lambda/2}$ emerging from the single-layer half-wave plate. For this multi-layer equivalent half-wave plate, the azimuthal angles of A-plates are: $\phi_{\text{ne\_A\_1st}} = -61.45^{\text{o}}$, $\phi_{\text{ne\_A\_2nd}} = -5.05^{\text{o}}$; the $d\Delta n$ of retardation films are: $d\Delta n_{\text{\_A\_1st}} = -72.95$ nm, , $d\Delta n_{\text{\_A\_2nd}} = -201.90$ nm, and $d\Delta n_{\text{\_C\_1st}} = -103.38$ nm. Using this design, $\Delta\mathbf{P}_{(2\text{A}+1\text{C}\_\lambda/2)-(\ \lambda/2)} < 0.217$ over the entire $\pm 85^{\text{o}}$ viewing cone in the 450 ~ 650 nm spectrum.

With the multi-layer equivalent half-wave plate, the quarter-wave plate in the conventional broadband circular polarizer is replaced by the combination of three A-plates and two C-plates as Fig. 13(b) sketches. By minimizing the cost

$$\cos t = \max\left\{\sqrt{2\left(S_{3\_(3\text{A}+2\text{C}\_\lambda/4)} + 1\right)} \mid \left(\theta = 0^0 \sim 85^0, \phi = 0^0 \sim 360^0, \lambda = 450\,\text{nm} \sim 550\,\text{nm}\right)\right\} \quad (4.6)$$

using genetic algorithm we have the design of the equivalent quarter-wave plate, where $S_{3\_(3\text{A}+2\text{C}\_\lambda/4)}$ is the $S_3$ of the state of polarization $\mathbf{P}_{(3\text{A}+2\text{C}\_\lambda/4)}$ emerging from the multi-layer equivalent quarter-wave plate. For this multi-layer equivalent quarter-wave plate, the azimuthal angles of A-plates are: $\phi_{\text{ne\_A\_3rd}} = 37.61^{\text{o}}$, $\phi_{\text{ne\_A\_4th}} = 2.40^{\text{o}}$, and $\phi_{\text{ne\_A\_5th}} = -46.97^{\text{o}}$; the $d\Delta n$ of retardation films are: $d\Delta n_{\text{\_A\_3rd}} = 90.71$ nm, $d\Delta n_{\text{\_A\_4th}} = 74.71$ nm, $d\Delta n_{\text{\_A\_5th}} = -33.68$ nm, $d\Delta n_{\text{\_C\_2nd}} = 48.09$ nm, and $d\Delta n_{\text{\_C\_3rd}} = -6.04$ nm.

Unlike above single wavelength circular polarizers, the variation in the produced state of polarization over a broad spectrum is similar to the conventional broadband circular polarizer at normal incidence angle. This can be seen in Figure 4.14, in which the red line shows that, over the ±85° viewing cone, the produced $S_3$ is less than –0.963 at $\lambda$ = 450 nm and decreases to –0.995 at $\lambda$ = 530 ~ 650 nm. The wavelength sensitivity is reduced by satisfying the relationship in Equation 4.4 and the viewing angle sensitivity is reduced by the above multi-layer equivalent plates. Thus the light leakage of the crossed circular polarizers is suppressed below $1.7\times10^{-3}$ over the ±85° viewing cone within the 450~650 nm spectral range, as Figure 4.15 depicts.

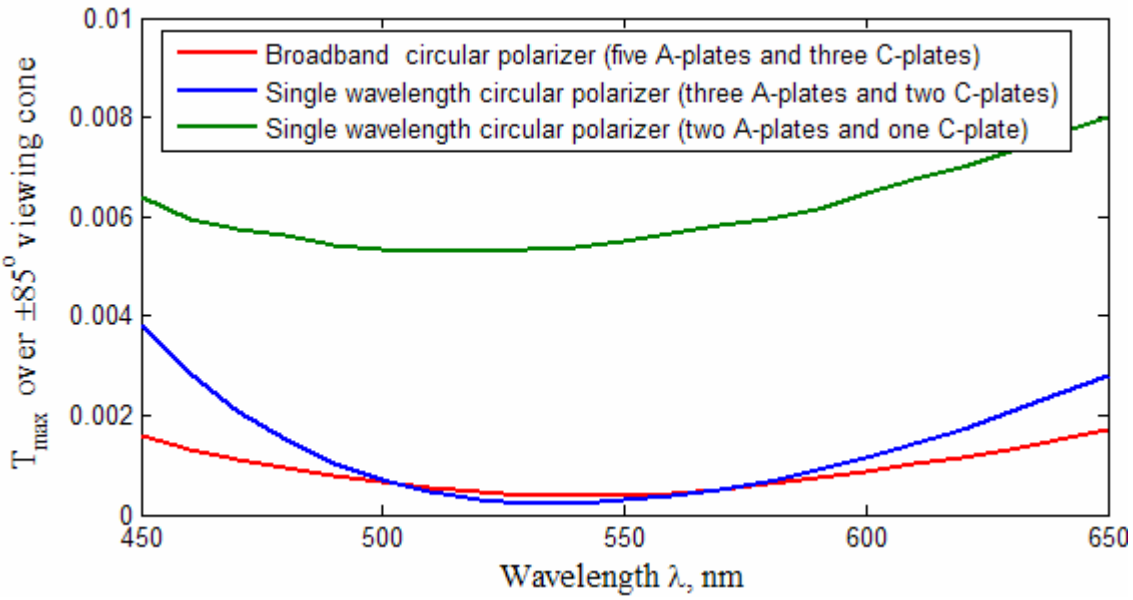


Figure 4.15: The calculated maximum light leakage from three-types crossed circular polarizers over the ±85° viewing cone as a function of wavelength. The ten-layer anti-reflection film is assumed.

In Figure 4.15, with the broadband wide-view circular polarizer, the light leakage of the crossed circular polarizers is not only kept below $1.7\times10^{-3}$ in the visual spectrum but also less than $3.79\times10^{-4}$ at $\lambda = 550$ nm. This is preferred in the liquid crystal displays since human visual system is more sensitive to the green light so that the green color requires a higher contrast ratio. In contrast, using single wavelength circular polarizers the light leakage increases dramatically when the incident spectrum deviates from the designed wavelength.

To form the crossed broadband circular polarizer, the polarizer and the first five A-plates together with the first three C-plates compose a right-handed circular polarizer as Figure 4.13(b) sketches. The analyzer and the other five A-plates together with the other three C-plates form the second circular polarizer. The arrangement of the A-plates and C-plates laminating to the analyzer are in reverse order and the azimuthal angles of the A-plates are at ninety degree with respect to their counter parts laminating to the polarizer. The ideal anti-reflection film in Figure 4.3(a) is assumed and coated on the air interface of both polarizers. For a left-handed circular polarizer using the configuration in Figure 4.13(b), the $d\Delta n$ of all A-plates and C-plate are not changed but the azimuthal angles of the A-plates are the negative of their counterparts in the right-handed circular polarizer.

## 4.4 Design tolerance

Design tolerance is an important concern for display manufacturing. For the design of a single-wavelength circular polarizer shown in Figure 4.9, we calculate the maximum light leakage of the crossed circular polarizers over the $\pm85^{o}$ viewing cone if the $d\Delta n$ of the A-plates

or C-plates varies by ±5%. As depicted in Figure 4.16(a), while the light leakage is insensitive to the errors in the second C-plate, a −5% error in the first C-plate increases the light leakage to $1.43\times10^{-3}$. Figure 4.16(b) depicts the maximum light leakage if the orientations of A-plates vary by ±5%. The light leakage rises to $1.61\times10^{-3}$ with a +5% error in the first A-plate. However, the light leakage is almost invariant when the orientation of the second A-plate varies by ±5%. Thus, for this design, the accuracy in the first A-plate and the first C-plate are more critical.

For the broadband circular polarizer shown in Figure 4.13(b), we calculate the maximum light leakage of the crossed circular polarizers if the $d\Delta n$ of the A-plates or C-plates varies by ±5%. Results are plotted in Figure 4.17(a). Although the light leakage is increased to $1.21\times10^{-3}$ with a +5% error in the first two A-plates and increased to $1.49\times10^{-3}$ with a −5% error in the first C-plate, it is less than $5.58\times10^{-4}$ in all other cases. Figure 4.17(b) shows the maximum light leakage if the orientations of the A-plates are deviated by ±5%. Although a +5% error in the first A-plate increases the light leakage to $1.49\times10^{-3}$, the light leakage is almost invariant with ±5% errors in the second and the third A-plats. The first two A-plates together with the first C-plate compose the equivalent half-wave plate and the other A-plates and C-plates compose the equivalent quarter-wave plate. This circular polarizer is more sensitive to the errors in the equivalent half-wave plate but insensitive to the errors in the equivalent quarter-wave plate. Comparing Figures 4.16 and 4.17, in the least favorable case, the maximum light leakage is still less than $1.61\times10^{-3}$ and $1.49\times10^{-3}$ for the single-wavelength and broadband circular polarizers, respectively.

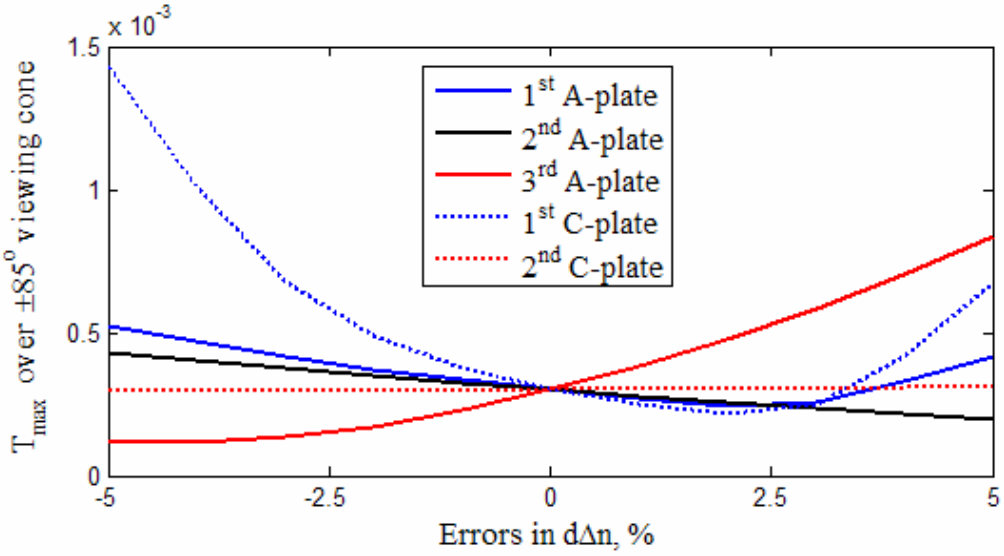


(a)

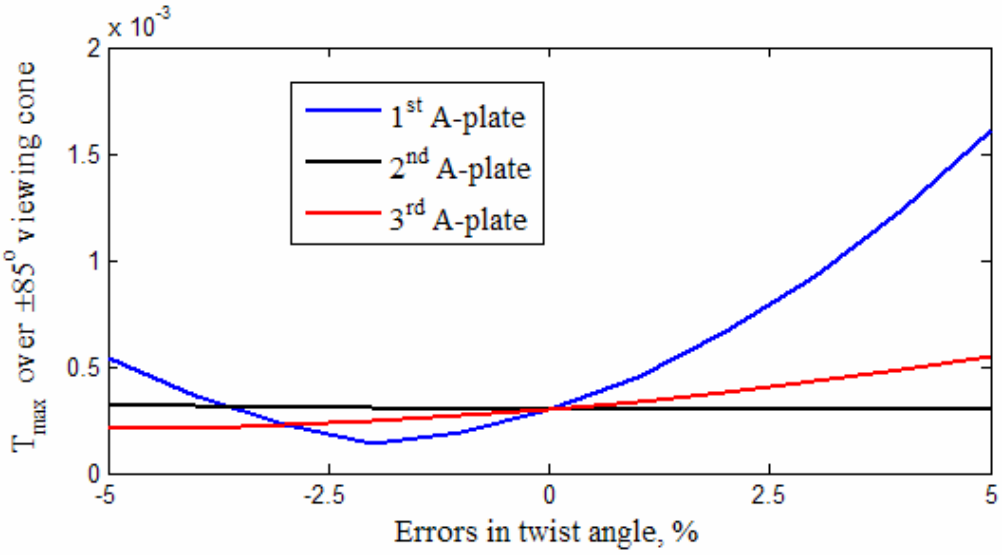


(b)

Figure 4.16: Design tolerance of the wide-view single wavelength circular polarizer shown in Figure 4.9: (a) variations in the $d\Delta n$ of A-plates and C-plates; (b) variations in the azimuthal angles of A-plates. The viewing cone is ±85° and $\lambda$ = 550 nm. Ten-layer anti-reflection film is assumed.

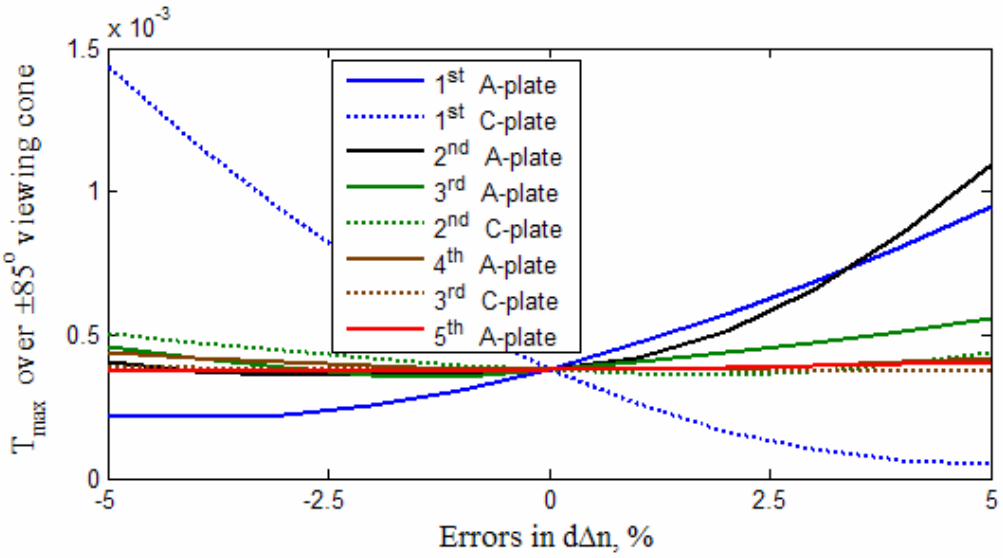


(a)

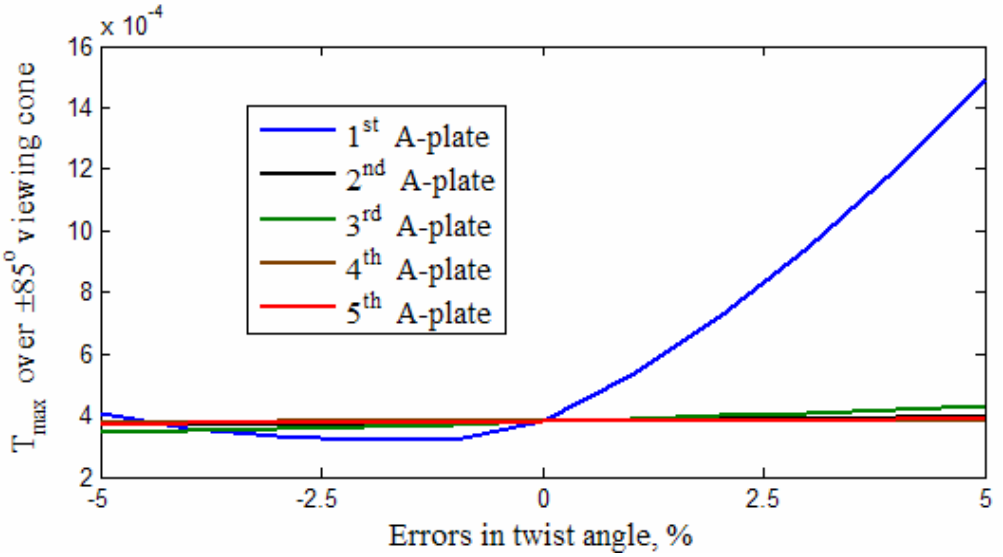


(b)

Figure 4.17: Design tolerance of the wide-view broadband circular polarizer shown in Figure 4.13(b): (a) variations in the $d\Delta n$ of A-plates and C-plates; (b) variations in the azimuthal angles of A-plates. The viewing cone is ±85° and $\lambda$ = 550 nm. Ten-layer anti-reflection film is assumed.

## 4.5. Summary

We demonstrate a novel methodology for designing wide-view circular polarizers. Both single wavelength and broadband circular polarizers are discussed. We use phase compensation techniques to reduce the difference between the produced state of polarization and the desired circular state of polarization over a wide range of viewing angle. The phase retardation film parameters are designed using genetic algorithm. The light leakage from the crossed circular polarizers using the proposed single-wavelength circular polarizer is less than $2.87\times10^{-4}$ over the $\pm85^{o}$ viewing cone at $\lambda$ = 550 nm. Using the proposed broadband circular polarizer, the light leakage is predicted to be less than $1.7\times10^{-3}$ over the $\pm85^{o}$ viewing cone for the visual white light and it is lower than $3.79\times10^{-4}$ at $\lambda$ = 550 nm.

# CHAPTER FIVE: WIDE VIEW LIQUID CRYSTAL DISPLAYS USING CROSSED CIRCULAR POLARIZERS CONSISTING OF UNIAXIAL PHASE RETARDATION FILMS

In addition to high contrast ratio, high and uniform transmittance over wide viewing angles is also highly desired for large screen liquid crystal televisions (LCD TVs). With the increase in the screen size of liquid crystal displays (LCDs), high transmittance effectively reduces the power consumption while the high contrast ratio and uniform transmittance ensure vivid images at flexible viewing positions for the audiences.

A pair of crossed polarizers is of key components in many transmissive mode liquid crystal displays [1]. If a liquid crystal (LC) cell is laminated between two crossed linear polarizers, to achieve maximum transmittance in the bright state the LC directors should be reoriented to the bisectors of the crossed linear polarizers [1-2, 16-17, 24-25]. Vertical alignment (VA) mode has been employed in many LCDs because of its excellent contrast ratio at normal incidence. In a vertical-alignment liquid crystal display (VA-LCD), in order to have uniform image quality over all the azimuthal angles, four domains are formed along the bisectors of the crossed linear polarizers [6, 16-17, 24-25]. However, due to the continuity the LC directors twist continuously from domain to domain so that the boundary areas are formed between domains [1-2, 17-18, 21-22, 24-25]. These boundary areas become dark areas under crossed linear polarizers so that the transmittance of the whole pixel is reduced. Nevertheless, under crossed circular polarizers, the transmittance of LCD only depends on the phase retardation ($\delta$) of the LC layer:

$$T = \sin^2(\delta/2). \tag{5.1}$$

Hence, the azimuthal angles of the LC directors are not necessary to be at the bisectors. As a result, the use of circular polarizers greatly enhances the bright state transmittance [24-25].

However, the light leakage from the crossed conventional circular polarizer is large at wide viewing angles so that the contrast ratio of VA-LCDs would be low [24-25]. To improve the light efficiency without sacrificing the contrast ratio at wide viewing angles, we can apply the wide-view circular polarizers discussed in Chapter 4 to the multi-domain VA-LCDs [26].

## 5.1. Multi-domain VA-LCD using wide-view circular polarizers

Figure 5.1(a) drafts the simplified schematic diagram of such a wide-view VA-LCD using crossed wide-view circular polarizers. Broadband wide-view circular polarizer designed in Chapter 4 is applied to cover the entire visual spectrum. The LC director distributions are simplified into eight domains at every $45^o$ from $22.5^o$ to $337.5^o$ in the bright state as Figure 5.1(b) sketches.

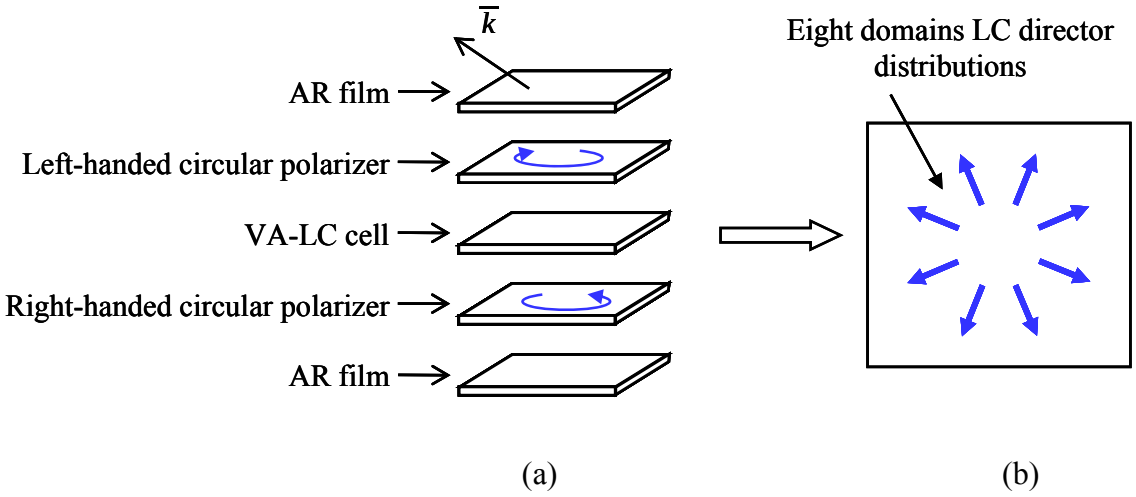


Figure 5.1: (a) Configuration of a high-contrast wide-view VA-LCD with crossed circular polarizers. (b) LC director distributions are simplified into eight domains at every 45$^{o}$ from 22.5$^{o}$ to 337.5$^{o}$ in the bright state. For this design, the light entering the VA LC layer is circularly polarized. In the bright state, eight domains of LC director distributions are formed at every 45$^{o}$ from 22.5 $^{o}$ to and 337.5 $^{o}$ with respect to the absorption direction of the polarizer.

On each side of LC layer, five A-plates and three C-plates are laminated to the adjacent linear polarizer to form a broadband wide-view circular polarizer as illustrated in Figure 5.2. The arrangement of the A-plates and C-plates are reversed on two sides and the azimuthal angles of the A-plates are at ninety degree with respect to their counter parts on the other side. Since the vertical alignment LC layer is not considered in the design of wide-view circular polarizers as we discussed in Chapter 4, to compensate the phase retardation of the LC layer in the dark state, two C-plates with equal thickness are laminated on both sides of the LC layer. The summation of the phase retardations of these two C-plates is the negative of the phase retardation of the LC layer.

We should emphasize that, in the dark state the light at the center of the LC layer is circularly polarized at wide viewing angles.

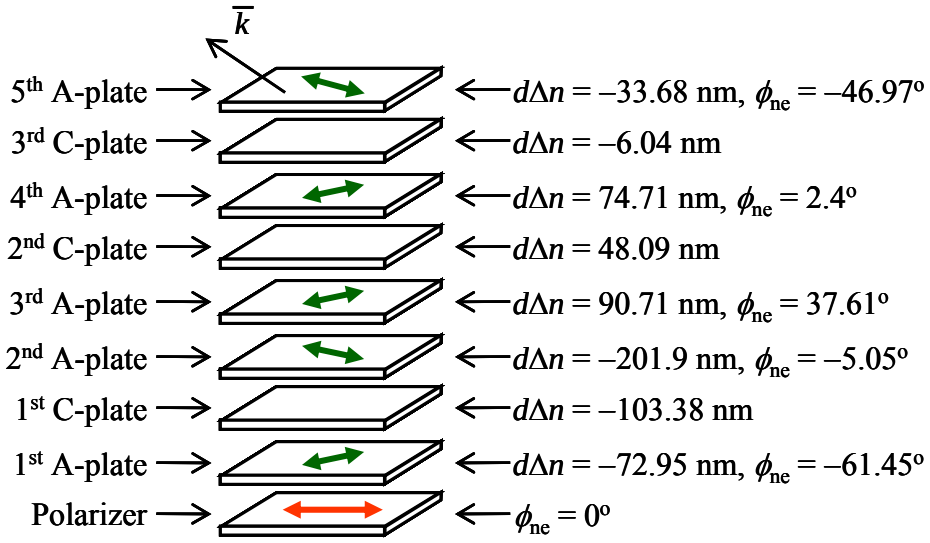


Figure 5.2: Device configuration of a broadband wide-view circular polarizer consisting of one linear polarizer, five uniaxial A-plates and three uniaxial C-plates. The design of this circular polarized is discussed in Chapter 4.

We use the finite difference method to simulate the bright state LC director distributions [31-33] and then use the 4-by-4 matrix method [39] to calculate the transmittance. The employed refractive indices of the polarizers and LC are as follows: $n_{e\_pol}$ =1.5 + $i$×3.251×10$^{-3}$, $n_{o\_pol}$ = 1.5 + $i$×2.86×10$^{-5}$, $n_{e\_LC}$ = 1.5514 and $n_{o\_LC}$ = 1.4737 at $\lambda$ = 550 nm. Here the color dispersion is assumed to be weak and not considered. The thickness of the polarizer is 210 μm and LC cell gap is 4 μm. We also assume the backlight is uniform within the ±85° viewing cone. The color

filters are not considered during calculations. To reduce air-polarizer surface reflection, an ideal anti-reflection film in Figure 5.3(a) is assumed and coated on the air interface of both polarizers.

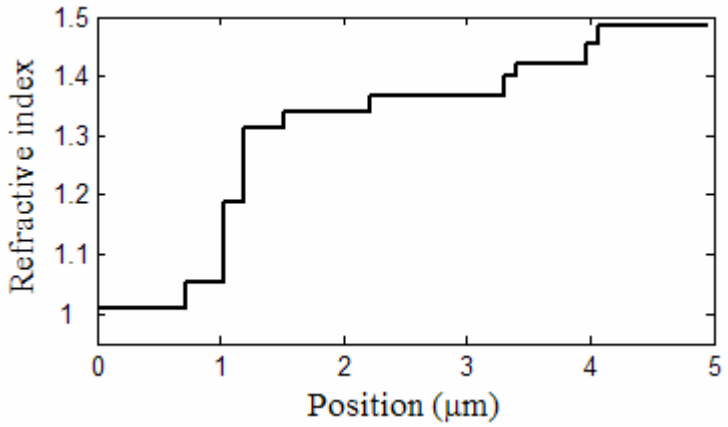


(a)

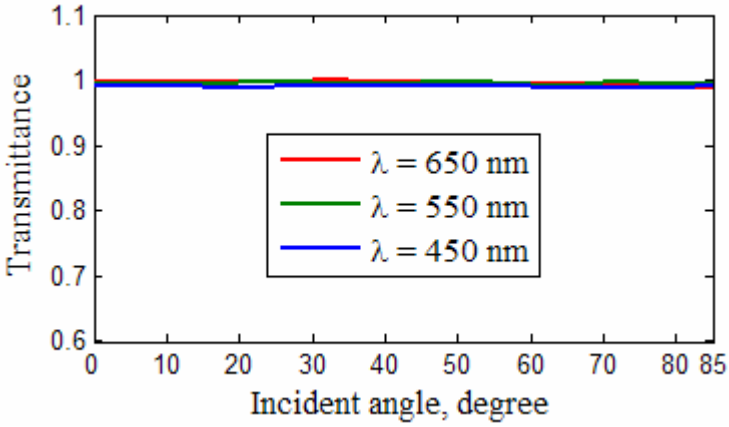


(b)

Figure 5.3: Ten-layer anti-reflection film: (a) refractive indices profile, and (b) transmittance.

5.2. Optical characteristics of a multi-domain VA-LCD using wide-view circular polarizers

Figure 5.4 depicts the optical characteristics of this LCD at $\lambda$ = 450, 550 and 650 nm. The maximum transmittance is higher than 0.34 (maximum transmittance for paralleled linear polarizers is 0.378) at normal viewing angle for the green and blue light, for red it is still ~0.30. The major optical loss comes from the absorption of the dichroic linear polarizers. Over the entire ±85$^{o}$ viewing cone, the minimum bright state transmittance remains ~68% and ~90% of the maximum transmittance for the green and red light, respectively. Further more, in all cases the transmittance is uniform over all the azimuth angles. Among these three colors, the green light has the highest contrast ratio, which is greater than 420:1 over the ±85$^{o}$ viewing cone. Although the contrast ratio is lower for the red light, it is still higher than 115:1 over all the viewing angles.

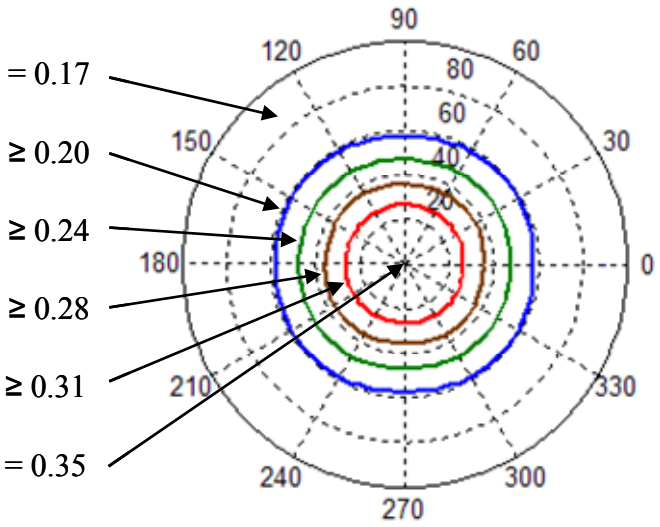


(a)

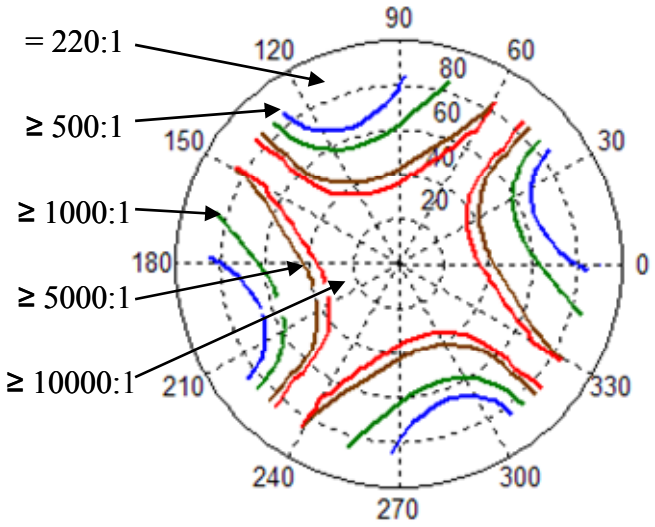
= 220:1
≥ 500:1
≥ 1000:1
≥ 5000:1
≥ 10000:1
90
120
60
80
60
40
20
150
30
180
0
210
330
240
300
270

(b)

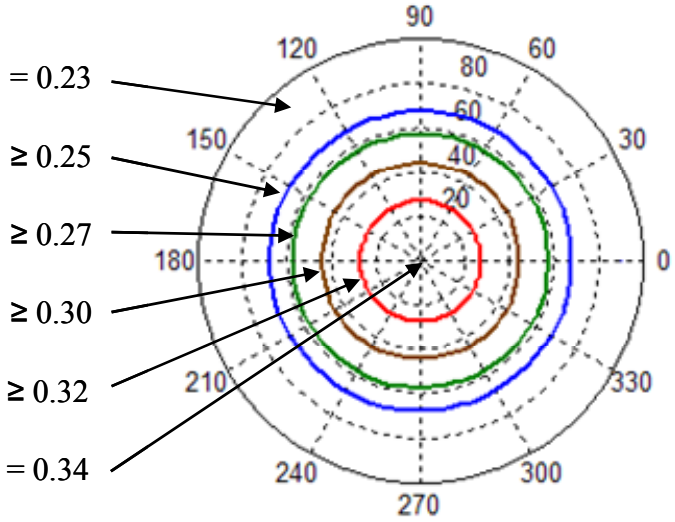
= 0.23
≥ 0.25
≥ 0.27
≥ 0.30
≥ 0.32
= 0.34
90
120
60
80
60
40
20
150
30
180
0
210
330
240
300
270

(c)

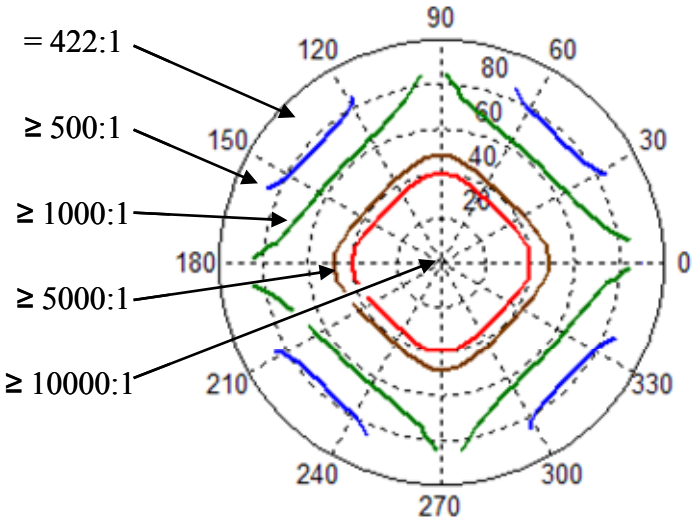
= 422:1
≥ 500:1
≥ 1000:1
≥ 5000:1
≥ 10000:1
90
120
60
150
30
180
0
210
330
240
300
270
80
60
40
20

(d)

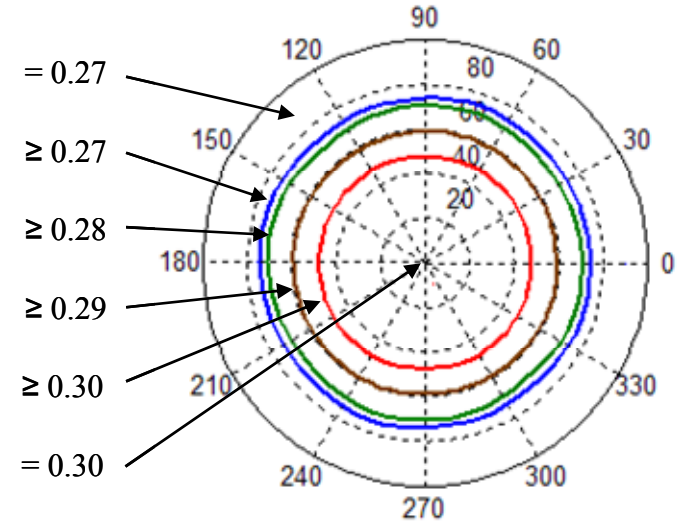
= 0.27
≥ 0.27
≥ 0.28
≥ 0.29
≥ 0.30
= 0.30
90
120
60
150
30
180
0
210
330
240
300
270
80
60
40
20

(e)

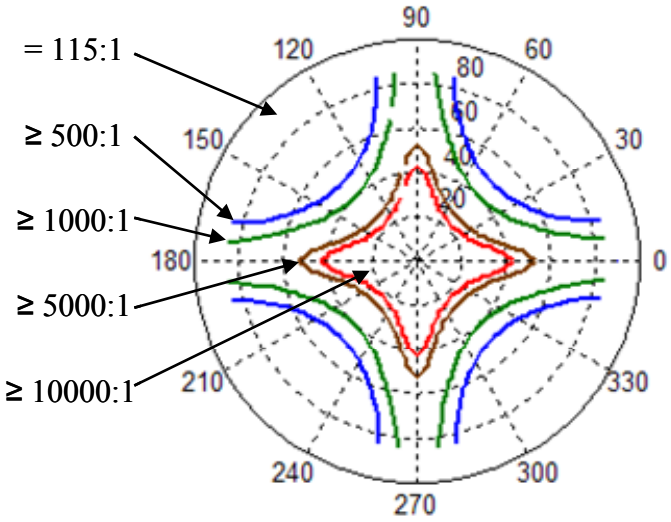


(f)

Figure 5.4: A VA-LCD using crossed broadband wide-view circular polarizers when LC directors form eight domains in the bright state: (a) iso-transmittance contour at $\lambda$ = 450 nm; (b) iso-contrast contour at $\lambda$ = 450 nm; c) iso-transmittance contour at $\lambda$ = 550 nm; (d) iso-contrast contour at $\lambda$ = 550 nm; e) iso-transmittance contour at $\lambda$ = 650 nm; (f) iso-contrast contour at $\lambda$ = 650 nm. The LCD configuration is sketched in Figure 5.1(a) and ten-layer anti-reflection film is assumed.

In a real display panel, the actual contrast ratio could be lowered because the above-mentioned ideal parameters may not be controlled precisely. Moreover, the lower extinction ratio of linear polarizer, imperfect LC alignment, variation and non-uniformity of the compensation film thickness, color dispersions of optical components, as well as the stress birefringence from films and substrates could also reduce the contrast ratio. Other than the above reasons, the actual angular brightness uniformity could also be lowered because of the non-ideal anti-reflection film.

At the same time, some LC directors around the domains' boundaries are not reoriented in the bright state because of the discontinuities between LC directors in different domains [1-2, 17-18, 21-22, 24-25]. This decreases the actual bright state transmittance. Color filters in a real display panel further reduce the actual bright state transmittance.

## 5.3. Summary

In this chapter, we demonstrate a wide view VA LCD with both high contrast ratio and high transmittance over the entire visual spectrum. Applying the wide-view and broadband circular polarizer proposed in Chapter 4, the maximum transmittance of the presented multi-domain VA LCD is predicted to be greater than 90% (0.34 out of 0.378) and the contrast ratio is higher than 420:1 for the green light. Over the entire visual spectrum the maximum transmittance is greater than 81% (0.30 out of 0.378) and the contrast ratio is higher than 115:1. The uniformity of better than 68% in the bright state transmittance is achievable over the $\pm 85^{o}$ viewing cone if the air-interface surface reflection is suppressed.

# CHAPTER SIX: WIDE VIEW AND BROADBAND CIRCUALR POLARIZER CONSISTING OF BIAXIAL PHASE RETARDATION FILMS

Circular polarizer is an important component for optical communications, optical remote sensing, and liquid crystal displays (LCDs) [23-25]. For the direct view liquid crystal displays, vertical alignment (VA) mode has been widely employed because of its excellent contrast ratio. In order to have uniform image quality over all the azimuthal angles, four domains are formed along the bisectors of the crossed linear polarizers [6, 16-17, 24-25] in a vertical-alignment liquid crystal display (VA-LCD). Because of the continuity of liquid crystal, the LC directors twist continuously from domain to domain inside multi-domain liquid crystal displays [1-2, 17-18, 21-22, 24-25] so that the boundary areas are formed between domains. These boundary areas appear dark under crossed linear polarizers and the pixel's transmittance is reduced. Nevertheless, as it was shown in Chapter 5, these dark zones are removed by using a pair of crossed circular polarizers [24-26].

A conventional circular polarizer consisting of a linear polarizer and a uniaxial quarter-wave plate produces circular polarization only at normal incidence. Replacing the uniaxial quarter-wave plate with a biaxial quarter-wave plate only slightly improves the acceptance angle [24-25]. In Chapter 4, a broadband wide-view circular polarizer using the combinations of optimally designed uniaxial A-plates and C-plates significantly widens the acceptance angle, but its device configuration is too sophisticated [26]. As a result, it is difficult to fabricate and the

cost is high. There is an urgent need to develop a simple and low cost wide-view circular polarizer.

Comparing to a uniaxial retardation film, the biaxial film provides an extra degree of freedom so that the device configuration of the wide-view circular polarizer can be simplified [15]. In this chapter, we demonstrate a wide-view circular polarizer consisting of a linear polarizer and two biaxial films [27]. The produced states of polarization are very close to the ideal circular polarization over a wide range of incident angles. Over the entire ±85$^{o}$ viewing cone, the light leakage of the crossed circular polarizers is less than $8.23\times10^{-5}$, provided that the air-interface surface reflections are suppressed.

## 6.1. Design of wide-view circular polarizer

To design a wide-view circular polarizer, we represent the state of polarization with Stokes parameters ($S_1$, $S_2$, and $S_3$) and portray on Poincaré sphere after the orthogonal components of the electric field are solved using the 4-by-4 matrix method [36-39]. If the state of polarization is represented by vector $\mathbf{P} = (S_1, S_2, S_3)$, then the polarization difference between an arbitrary polarization $\mathbf{P}_{(X)} = (S_{1\_(x)}, S_{2\_(x)}, S_{3\_(x)})$ and the right-handed circular polarization $\mathbf{P}_{(RCP)} = (0, 0, -1)$ can be described by [26-27, 41-42]:

$$\begin{aligned}\Delta\mathbf{P}_{(X)-(RCP)} &= \mathbf{P}_{(X)} - \mathbf{P}_{(RCP)} \\ &= \sqrt{\left(S_{1\_(X)} - 0\right)^2 + \left(S_{2\_(X)} - 0\right)^2 + \left(S_{3\_(X)} - (-1)\right)^2} \\ &= \sqrt{2(S_{3\_(X)} + 1)}.\end{aligned} \tag{6.1}$$

As shown in Equation. 6.1, once $S_{3\_(X)}$ descends to −1, $\Delta\mathbf{P}_{(X)-(RCP)}$ approaches zero and the polarization $\mathbf{P}_{(X)}$ becomes the right-handed circular polarization $\mathbf{P}_{(RCP)}$.

In this chapter, the absorptive linear polarizer is modeled as a lossy uniaxial material. We assume the refractive indices of the liner polarizer and the biaxial retardation films are as follows: $n_{x\_pol} = 1.5 + i\times3.251\times10^{-3}$, $n_{y\_pol} = 1.5 + i\times2.86\times10^{-5}$, $n_{z\_pol} = 1.5 + i\times2.86\times10^{-5}$, $n_{x\_film} = 1.\ 5124$, $n_{y\_film} = 1.5089$. The refractive index $n_{z\_film}$ of each biaxial film is determined by its NZ factor, where $NZ = (n_x - n_z)/(n_x - n_y)$ [15]. The linear polarizer has a thickness of 210 μm and its absorption axis is oriented along $0^o$. The design wavelength is $\lambda$=550 nm.

On both sides of the absorptive polarizer, the protective Tri-Acetyl-Cellulose (TAC) films exhibit a small birefringence and act as negative birefringence C-plates. The phase change due to the TAC film can be minimized if we laminate a positive birefringence C-plate to the exit protective film. The phase retardation of this C-plate compensates for the adjacent protective film so that the C-plate effect of the linear polarizer is negligible.

A circular state of polarization is achieved when a quarter-wave plate is illuminated by a linearly polarized light vibrating at $45^o$ with respect to its slow axis [41-42]. If this light is produced by a linear polarizer, the quarter-wave plate together with the linear polarizer forms a conventional circular polarizer. At normal incidence, when the linearly polarized light passes through the quarter-wave plate, the light sustains $\pi/2$ phase change while the magnitudes of its orthogonal components remain equal so that the light becomes circularly polarized. However, at oblique angles the quarter-wave plate contributes other than $\pi/2$ phase change [24-25] and the slow axis is not at $45^o$ with respect to the incoming linear polarization. As a result, the produced polarization state becomes elliptical and a relatively large amount of light leaks through the

crossed circular polarizers. Replacing the uniaxial quarter-wave plate with a biaxial quarter-wave plate reduces the variation in the $\pi/2$ phase change at oblique incident angles. However, the $45^{o}$ angle between the light's vibration direction and the biaxial film's slow axis is not maintained at oblique incidence [15, 16]. Therefore, although the produced polarization is relatively close to the circular polarization, the light leakage of the crossed circular polarizers is still large at wide viewing angles [24-25].

To preserve circular polarization over a wide range of incident angle, we laminate two biaxial retardation films to the linear polarizer as shown in Figure 6.1. Since all of the three Stokes parameters are modified inside a biaxial film, the azimuthal angles and the $d\cdot(n_x - n_y)$ as well as the NZ factors of both biaxial films are the key design parameters. Here the azimuthal angle of biaxial film is the angle between the $n_x$ axis of the biaxial film and the absorption direction of the polarizer as Figure 6.1 shows.

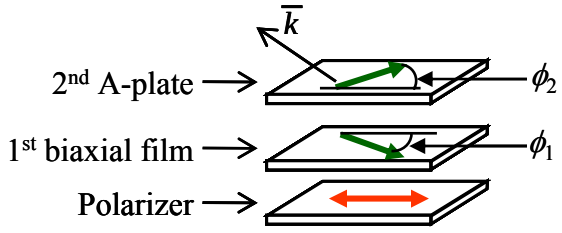


Figure 6.1: Configuration of a wide-view circular polarizer with a linear polarizer and two biaxial films.

We use genetic algorithm [45, 46] to optimize the polarizer design. For a given combination of the above parameters, we first solve the orthogonal components of the electric

field using the 4-by-4 matrix method. Then we find the produced polarization and apply it into the following cost function

$$\cos t = \max\left\{\sqrt{2(S_{3\_(2B)}+1)} \mid \left(\theta_{\text{in}} = 0^0 \sim 85^0, \phi_{\text{in}} = 0^0 \sim 360^0\right)\right\}, \tag{6.2}$$

where $S_{3\_(2B)}$ is the $S_3$ of the produced state of polarization $\mathbf{P}_{(2B)}$. By minimizing the cost function shown in Equation 6.2, we could obtain the optimal design parameters for the biaxial films. For the two biaxial films, their azimuthal angles are: $\phi_1 = 0.68^o$ and $\phi_2 = 46.37^o$; the $d\cdot(n_x - n_y)$ values are: $d\cdot(n_x - n_y)_1 = 264.08$ nm and $d\cdot(n_x - n_y)_2 = 134.13$ nm; and the NZ factors are: $NZ_1 = 0.75$ and $NZ_2 = 0.53$.

Figure 6.2 illustrates the polarization states inside this circular polarizer using Poincaré sphere representation. As Figure 6.2 depicts, the first biaxial film serves as a wide-view half-wave plate so that the light entering the second biaxial film is almost linearly polarized and vibrating at ~45$^o$ with respect to the $n_x$ axis of the second biaxial film. Meanwhile, the second biaxial film performs as a wide-view quarter-wave plate. Therefore, although the polarizations across each biaxial film vary with the incident angle, they compensate each other so that the final polarization remains circular over a wide viewing cone.

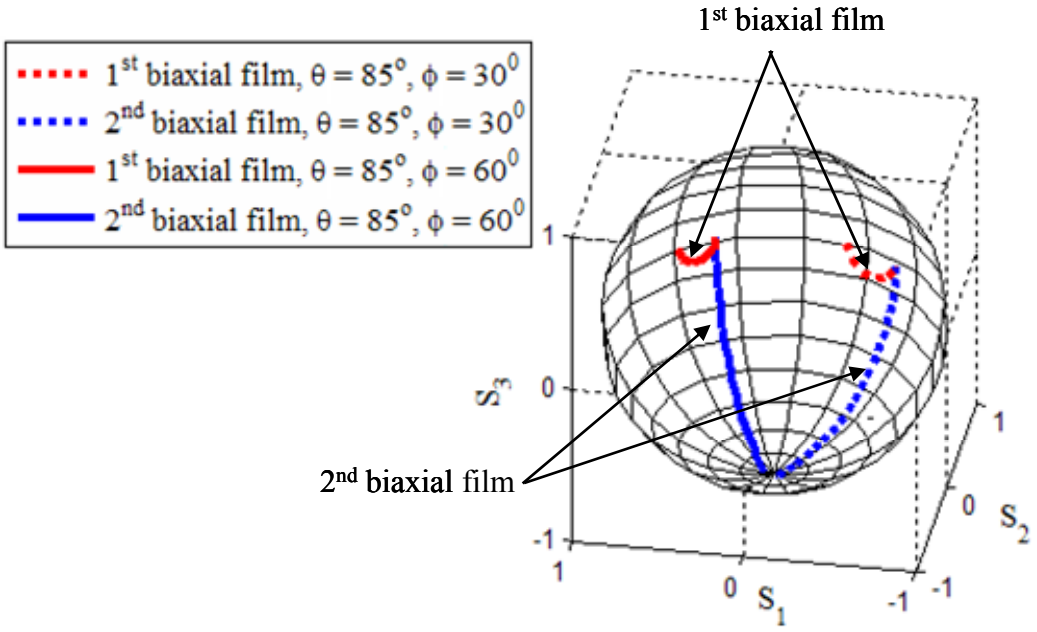


Figure 6.2: States of polarization inside a wide-view circular polarizer at oblique incidence $\theta =$ 85°. Dotted lines and solid line show the polarization states when the azimuths of incident plane $\phi$ are at 30° and 60°, respectively. Red and blue lines show the polarizations inside the first and second biaxial films, respectively.

As demonstrated in Figure 6.3, for the proposed right-handed circular polarizer $S_3$ only increases to −0.997 when the viewing angle increases to 85°. This is equivalent to having the polarization difference $\Delta\mathbf{P}_{(2B)-(RCP)}$ less than 0.078 over the ±85° viewing cone. The produced $S_3$ remains at −1 at normal angle as in the conventional right-handed circular polarizer. For a left-handed circular polarizer using above configuration, the NZ factors and $d\cdot(n_x - n_y)$ of both biaxial films are not changed but the azimuthal angles of the biaxial films are the negative of their counterparts in the right-handed circular polarizer.

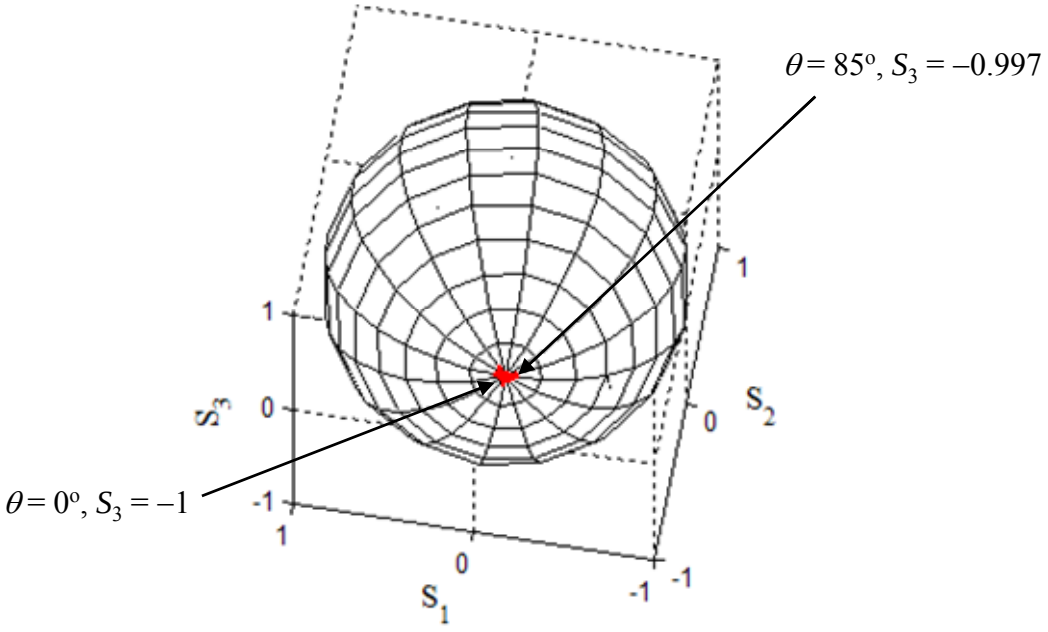


Figure 6.3: State of polarization emerging from a wide-view circular polarizer when $\theta = 0^{o} \sim 85^{o}$ at each fixed $\phi$, where $\phi = 0^{o} \sim 360^{o}$ with $10^{o}$ interval.

## 6.2. Optical characteristics of the designed wide-view circular polarizer

Since the produced polarization approaches ideal circular polarization, the light leakage from crossed circular polarizers can be significantly reduced. Figure 6.4 sketches the configuration of the crossed circular polarizers. The bottom linear polarizer and the first two biaxial films compose a wide-view right-handed circular polarizer. The top analyzer and the last two biaxial films form a second circular polarizer crossed to the first one. The absorption axis of the analyzer and the azimuthal angles of the last two biaxial films are perpendicular to their counter parts in the first circular polarizer.

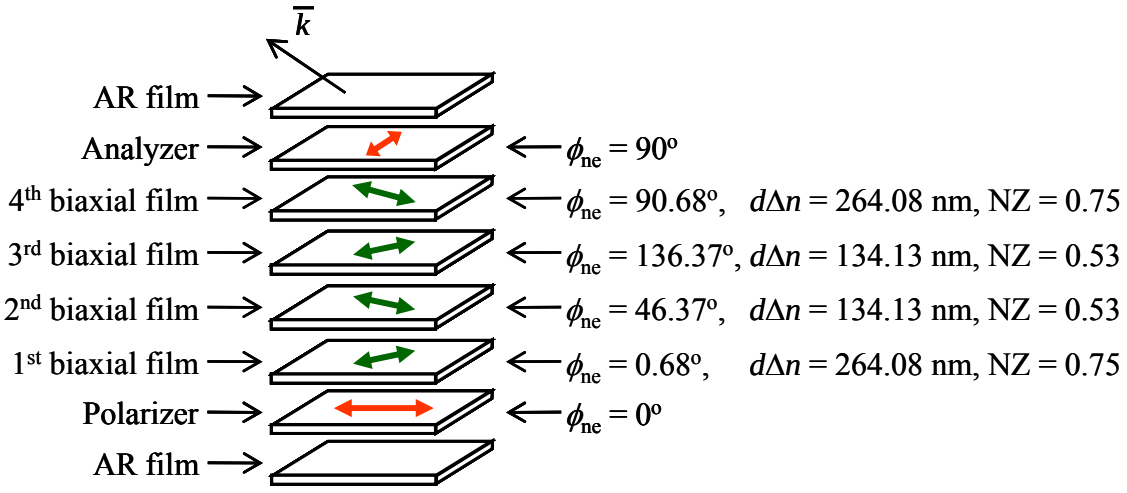


Figure 6.4: Device configuration of the crossed wide-view circular polarizers.

The circular polarization emerging from the first circular polarizer is converted into linear polarization after it passes though the two biaxial films attached to the analyzer. Due to the symmetric configuration of the crossed circular polarizers, this linearly polarized light vibrates along the analyzer's absorption direction. Therefore, the light leakage of the crossed circular polarizers is less than $8.23\times10^{-5}$ over the ±85° viewing cone as Figure 6.5(a) demonstrates.

Besides the light leakage of crossed polarizers, for wide-view LCD applications we also need to know the angular-dependent transmittance when the polarizers are open. Results are plotted in Figure 6.5(b). The maximum transmittance is 0.378 (maximum transmittance for paralleled linear polarizers is 0.378), which occurs at normal incidence. The major optical loss is from the absorption of the dichroic linear polarizers. The iso-transmittance contour shown in Figure 6.5(b) is relatively symmetric. At ±85° viewing cone, the transmittance remains greater than 0.311. Thus, from Figures 6.5(a) and 6.5(b), the calculated extinction ratio (at $\lambda$ = 550 nm) of the circular polarizer remains ~4000:1 at the ±85° viewing cone.

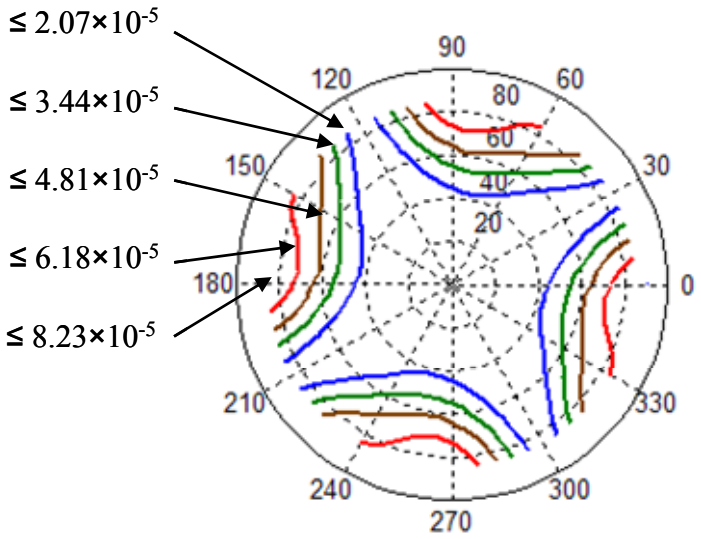


(a)

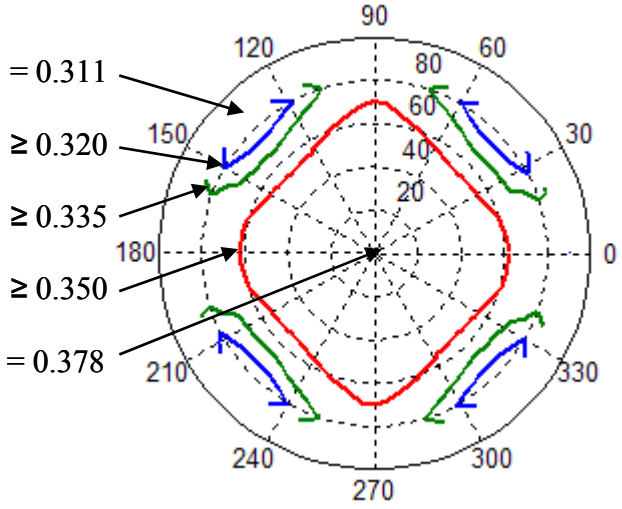


(b)

Figure 6.5: Iso-transmittance contour showing: (a) light leakage of the crossed wide-view circular polarizers, and (b) transmittance of two parallel circular polarizers. $\lambda$ = 550 nm. Ten-layer anti-reflection film in Figure 6.6 is assumed.

In order to reduce the interference of the air-polarizer surface reflection, an ideal anti-reflection (AR) film is assumed during simulations. The ten-layer anti-reflection film is coated on the air interface of both polarizers. This AR film is designed using genetic algorithm and the gradient refractive indices profile is illustrated in Figure 6(a) [44, 45]. The origin represents the air-AR interface. The transmittance of this ten-layer AR film is greater than 0.99 over the ±85$^{o}$ incident cone within the 450 nm ~ 650 nm spectrum as Figure 6.6(b) depicts.

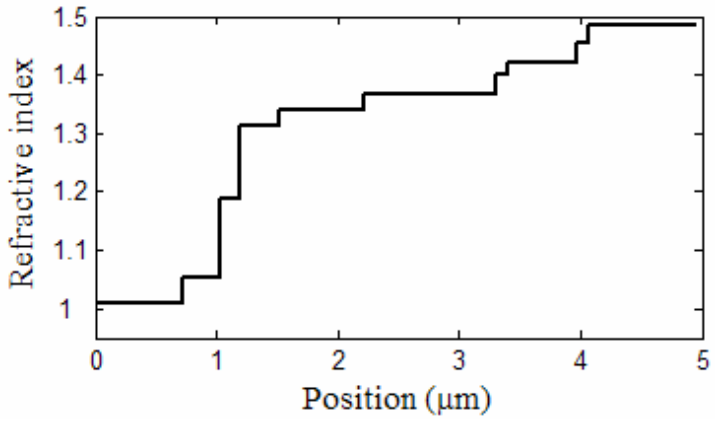


(a)

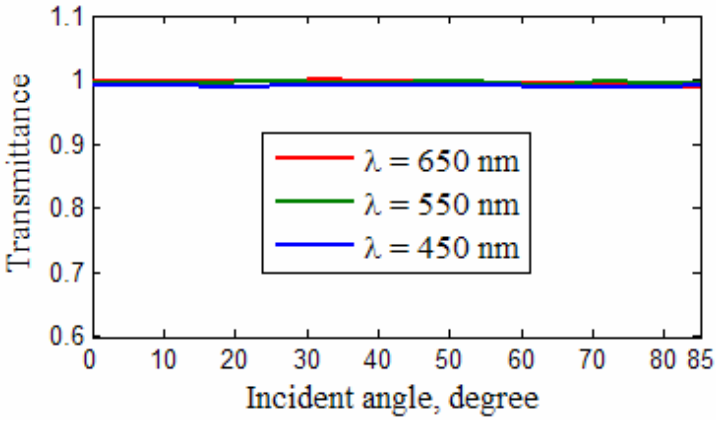


(b)

Figure 6.6: Ten-layer ideal anti-reflection film: (a) refractive indices profile, (b) transmittance.

## 6.3. Spectral bandwidth of the designed wide-view circular polarizer

For some applications such as direct-view LCDs, broad bandwidth is as important as wide viewing angle [1, 3-6, 23-28]. Although the proposed wide-view circular polarizer is designed at a single wavelength $\lambda$ = 550 nm, however, at normal incidence the retardation of the first biaxial film is almost equal to one half of the designed wavelength, i.e., $d\cdot(n_x - n_y)_1$ = 264.08 nm ≈ 550 nm/2 = $\lambda$/2, and the retardation of the second biaxial film is close to a quarter of the designed wavelength, $d\cdot(n_x - n_y)_2$ =134.13 nm ≈ 550 nm/4 = $\lambda$/4. At the same time, the azimuthal angles of the two biaxial films satisfy the following relationship:

$$\begin{aligned} 2\phi_1 - 4\phi_2 &= 2\times(360+46.37) - 4\times(180+0.68) \\ &= 90.02^0 \\ &\approx 90^0 \end{aligned} \quad , \qquad (6.3)$$

which describes the relationship between the azimuthal angles of the half-wave plate and the quarter-wave plate inside a broadband circular polarizer [46]. Therefore, at normal incidence the proposed circular polarizer performs as a broadband circular polarizer so that the light leakage of the crossed circular polarizers is less than $1.64\times10^{-6}$ over the 450~650 nm spectral range, as shown in Figure 6.7. Within the ±60° viewing cone, the light leakage is maintained less than $1.90\times10^{-3}$ over the specified visible spectral range. At ±85° viewing cone, the maximum light leakage reaches $3.92\times10^{-3}$ at $\lambda$ = 450 nm and $1.39\times10^{-3}$ at $\lambda$ = 650 nm. For display applications, the light leakage at blue is more forgiven than green and red because human visual system is less sensitive to blue. Moreover, the blue spectral content is the weakest among the three primary colors.

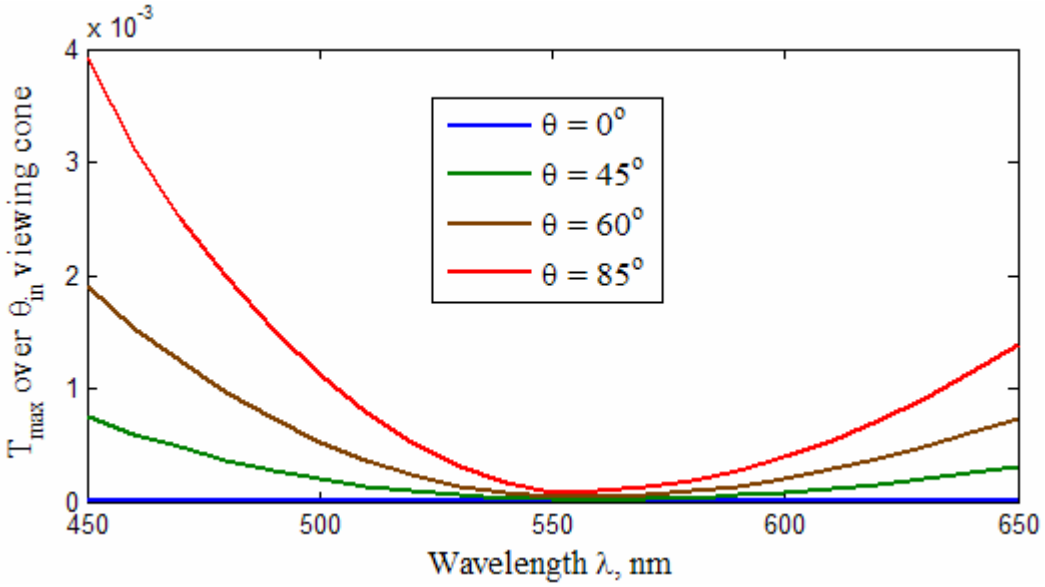


Figure 6.7: The calculated maximum light leakage of the crossed circular polarizers at different viewing angles as a function of wavelength. The configuration of the crossed circular polarizers is in Figure 6.1 and the anti-reflection film in Figure 6.6 is assumed.

## 6.4. Design tolerance

Design tolerance is an important concern from manufacturing viewpoint. For the proposed design of a wide-view circular polarizer, we calculate the maximum light leakage of the crossed circular polarizers over the ±85° viewing cone if the film parameters of the biaxial films deviate from the optimal values by ±5%. The simulation results are plotted in Figure 6.8. First we evaluate the influence of film thickness. The blue line in Figure 6.8 indicates that a +5% deviation in the first biaxial film thickness boosts the light leakage to $4.1\times10^{-4}$. By contrast, the light leakage is quite inert to the errors of the second biaxial film thickness (dashed blue lines). Next, we study how the NZ factor affects the light leakage. As shown by the black solid line in

Figure 6.8, the NZ factor of the first biaxial film plays a significant role. A ±5% deviation causes ~$7.0\times10^{-4}$ light leakage. On the other hand, a +5% error in the NZ factor of the second biaxial film boosts the light leakage to $4.5\times10^{-4}$ (black dashed line). The solid and dashed red lines in Figure 6.8 almost overlap with the blue dashed lines implying the light leakage is almost invariant when the orientations of both biaxial films vary by ±5%. Thus, from this tolerance analysis we find that the accuracy of the first biaxial film parameters is more critical than that of the second biaxial film and the NZ factors of both biaxial films require a higher accuracy.

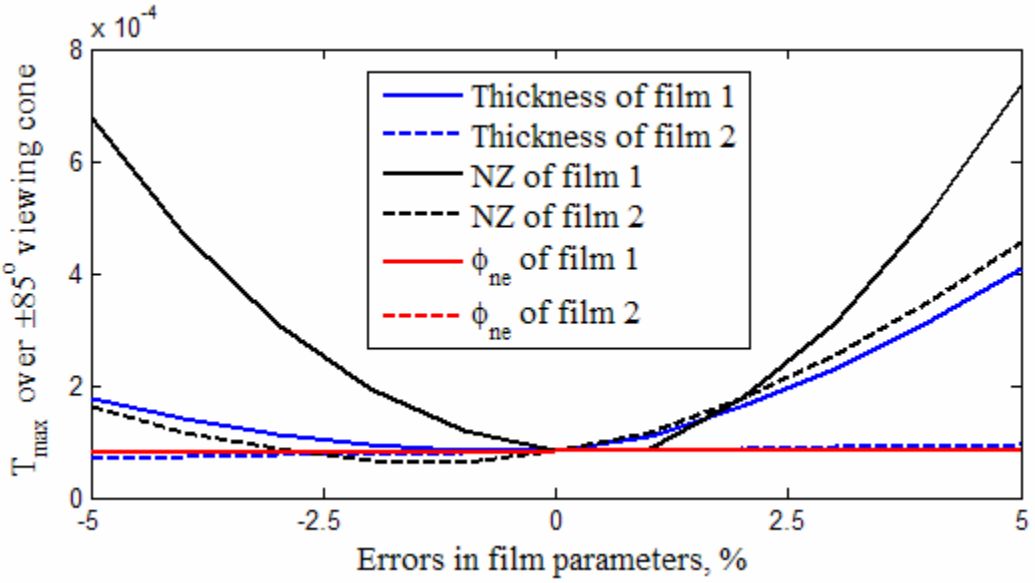


Figure 6.8: Design tolerance of the proposed wide-view circular polarizer. The viewing cone is ±85° and $\lambda$ = 550 nm. Ten-layer anti-reflection film is assumed.

## 6.5. Summary

In this chapter we propose a new wide-view circular polarizer consisting of a linear polarizer and two biaxial films. We use phase compensation techniques to constrain the resultant polarization state to the desired circular polarization over a wide range of viewing angle. The phase retardation film parameters are designed using genetic algorithm. The light leakage from the crossed circular polarizers using the proposed circular polarizer is less than $8.23\times10^{-5}$ over the $\pm85^{o}$ viewing cone at the designed wavelength $\lambda$ = 550 nm. Within the 450~650 nm spectral range, the light leakage of the crossed circular polarizers is kept below $3.92\times10^{-3}$ over the entire $\pm85^{o}$ viewing cone. This simple circular polarizer will find useful application for enhancing the transmittance of the multi-domain vertically-aligned liquid crystal displays.

# CHAPTER SEVEN: WIDE VIEW LIQUID CRYSTAL DISPLAYS USING CIRCUALR POLARIZERS CONSISTING OF BIAXIAL PHASE RETARDATION FILMS

In Chapter 5 we demonstrate a wide-view multi-domain vertical alignment liquid crystal display (VA-LCD), which employs a broadband wide-view circular polarizer using the combinations of optimized uniaxial A-plates and C-plates. Both high transmittance and high contrast ratio are maintained over a wide viewing zone [26]. However, its sophisticated device configuration results in complicated manufacture and high cost. There is an urgent need to develop a simple and low cost wide-view LCD with high transmittance.

Comparing to a uniaxial retardation film, the biaxial film provides an extra degree of freedom so that the device configuration of the wide-view circular polarizer can be simplified [15, 27]. In Chapter 6 we propose a broadband wide-view circular polarizer consisting of a linear polarizer and two biaxial films. The produced states of polarization are very close to the ideal circular polarization so that the light leakage from the crossed circular polarizers is less than $8.23\times10^{-5}$ over the $\pm85^{o}$ viewing cone at the designed wavelength $\lambda$ = 550 nm. In this chapter, we apply this broadband wide-view circular polarizer to a multi-domain VA-LCD. The contrast ratio of the proposed multi-domain VA-LCD is predicted to be higher than 800:1 over the $\pm85^{o}$ viewing cone at $\lambda$ = 550 nm and the calculated bright state transmittance is higher than 88% (out of 37.8%) at normal view. Over the entire visual spectrum the maximum transmittance is higher than 78% (out of 37.8%) and the contrast ratio remains higher than 110:1. The uniformity of

better than 70% in the bright state transmittance is predicted over the ±85$^{o}$ viewing cone if the air-interface surface reflection is suppressed.

## 7.1. Multi-domain VA-LCD using wide-view circular polarizers

Figure 7.1 depicts the simplified schematic diagram of a wide-view VA-LCD using crossed wide-view circular polarizers. The bottom linear polarizer and the first two biaxial films compose a wide-view right-handed circular polarizer. The top analyzer and the last two biaxial films form a second circular polarizer crossed to the first one. The absorption axis of the analyzer and the azimuthal angles of the last two biaxial films are perpendicular to their counter parts in the first circular polarizer. To compensate the phase changes introduced by the vertical alignment LC cell at oblique viewing angles, two negative uniaxial C-plates with equal phase retardations are laminated to the both sides of LC cell. The $d\cdot(n_x - n_y)$ values of both C-plates are –161.67 nm when the $d\cdot(n_x - n_y)$ of the VA LC layer is 341.88 nm. The LC director distributions are simplified into eight domains at every 45$^{o}$ from 22.5$^{o}$ to 337.5$^{o}$ in the bright state.

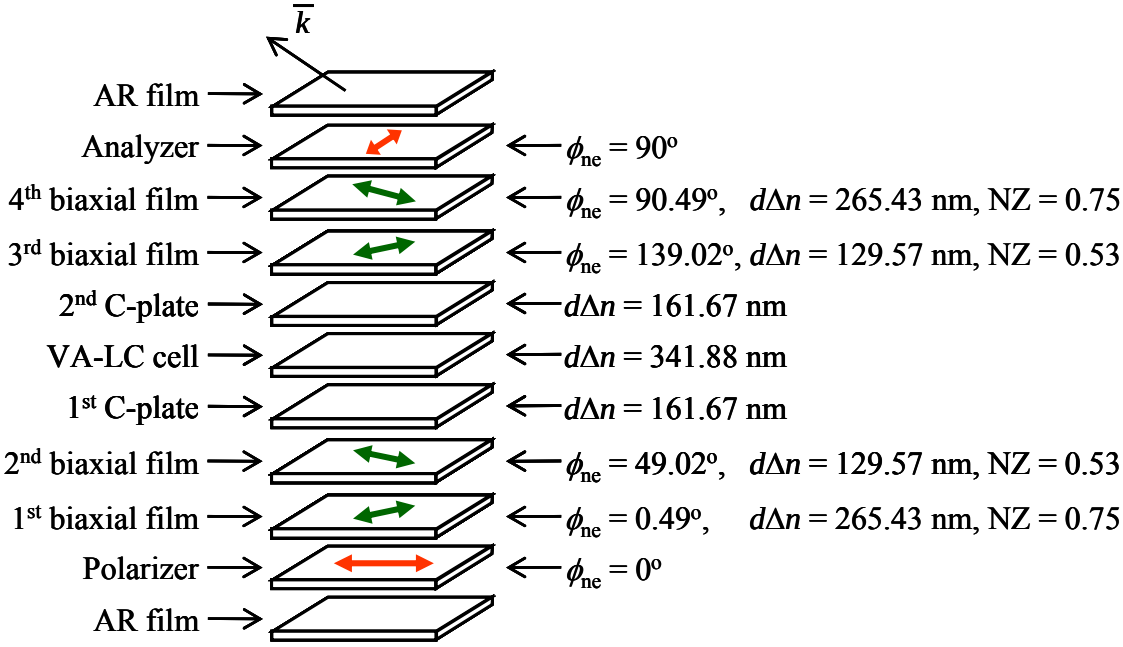


Figure 7.1: Configuration of a wide-view multi-domain VA-LCD with crossed wide-view circular polarizer.

In the dark state, since the phase changes due to the VA-LC layer are compensated by the negative C-plates, the circular polarization emerging from the first circular polarizer reaches the second circular polarizer and is converted into linear polarization after it passes though the two biaxial films attached to the analyzer. Due to the symmetric configuration of the crossed circular polarizers, this linearly polarized light vibrates along the analyzer's absorption direction. Therefore, the dark state light leakage is significantly reduced so that the calculated contrast ratio is higher than 800:1 between ±85° viewing angles as shown in Figure 7.2(a). Since the bright state transmittance is only determined by the phase retardation of the LC layer as we discussed in Chapter 5, the simulated bright state transmittance is higher than 0.333 (maximum transmittance for paralleled linear polarizers is 0.378) at the normal view as Figure 7.2(b) depicts. Furthermore,

if the air-interface surface reflection is assumed to be reduced by an ideal anti-reflection film in Figure 7.3, the bright state transmittance is higher than 0.233 over the entire ±85$^{o}$ viewing cone as demonstrated in Figure 7.2(b).

For direct-view LCDs, broad bandwidth is as important as wide viewing angle [1, 3-6, 23-28]. Although the above wide-view circular polarizer is designed at a single wavelength $\lambda$ = 550 nm, however, at normal incidence the retardation of the first biaxial film is almost equal to one half of the designed wavelength, i.e., $d\cdot(n_x - n_y)_1$ = 265.43 nm ≈ 550 nm/2 = $\lambda/2$, and the retardation of the second biaxial film is close to a quarter of the designed wavelength, $d\cdot(n_x - n_y)_2$ = 129.57 nm ≈ 550 nm/4 = $\lambda/4$. At the same time, the azimuthal angles of the two biaxial films satisfy the relationship $2\phi_1 - 4\phi_2 \approx 90^0$, which describes the relationship between the azimuthal angles of the half-wave plate and the quarter-wave plate inside a broadband circular polarizer [26]. Therefore, over ±85$^{o}$ viewing cone, the contrast ratio of the proposed wide-view LCD remains higher than 110:1 for both blue and red light as Figures 7.2(c) and 7.5(e) illustrate. At the same time, as depicted in Figures 7.2(d) and 7.2(f), the bright state transmittance maintains higher than 0.340 and 0.289 for the blue and red light, respectively.

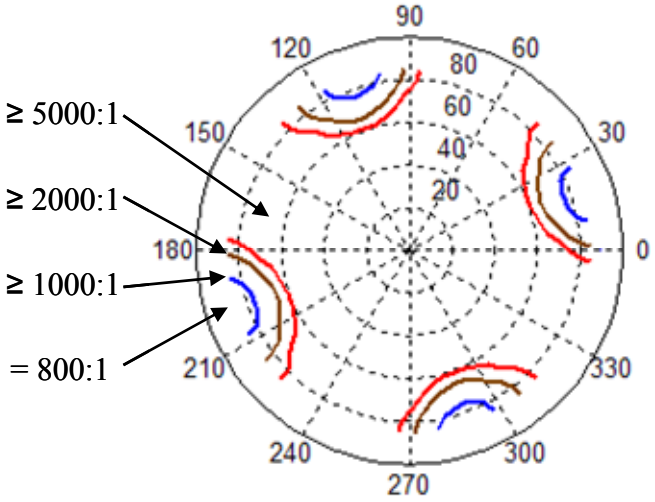
≥ 5000:1
≥ 2000:1
≥ 1000:1
= 800:1
90
120
60
80
60
40
20
150
30
180
0
210
330
240
300
270

(a)

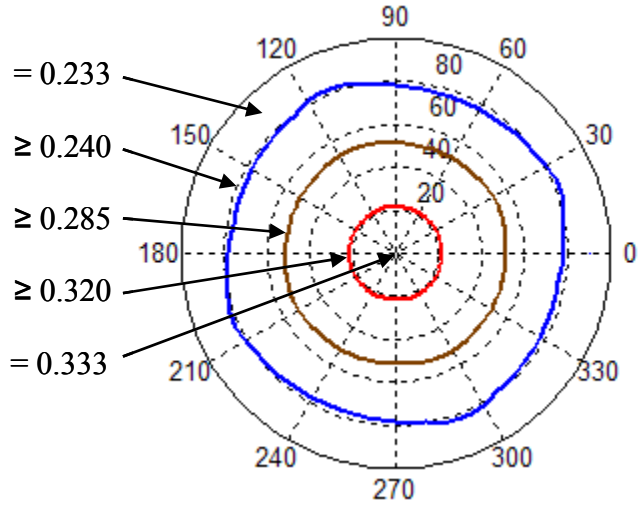
= 0.233
≥ 0.240
≥ 0.285
≥ 0.320
= 0.333
90
120
60
80
60
40
20
150
30
180
0
210
330
240
300
270

(b)

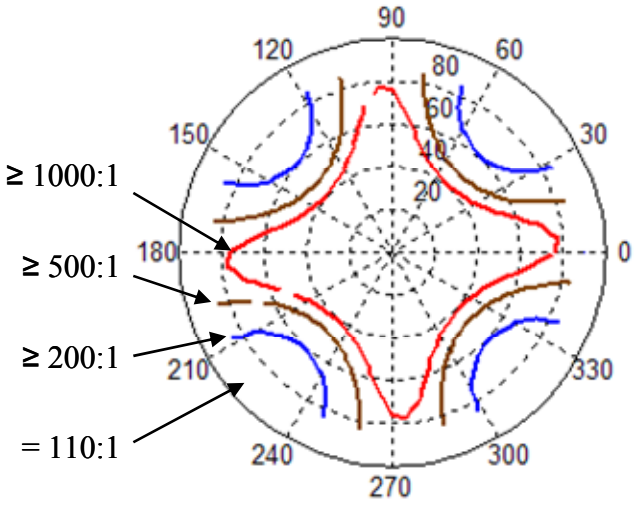
90
120
60
80
60
40
20
150
30
≥ 1000:1
≥ 500:1
180
0
≥ 200:1
210
330
= 110:1
240
300
270

(c)

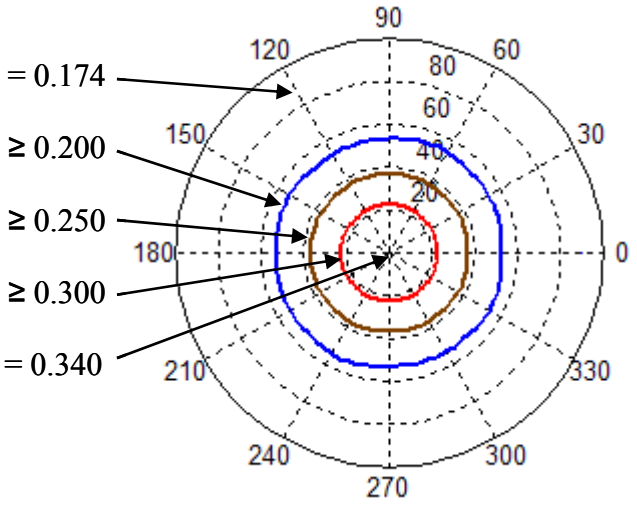
90
120
60
80
60
40
20
= 0.174
150
30
≥ 0.200
≥ 0.250
180
0
≥ 0.300
= 0.340
210
330
240
300
270

(d)

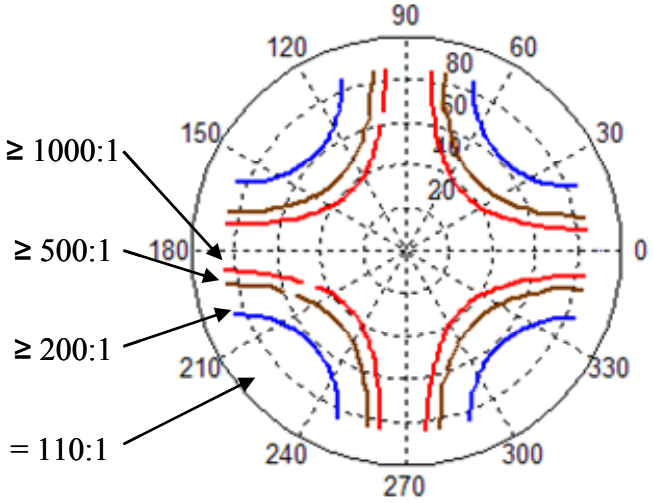


(e)

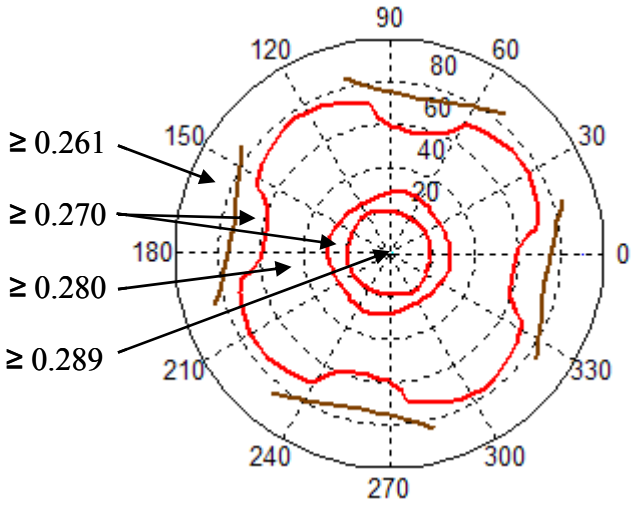


(f)

Figure 7.2: A VA-LCD using crossed wide-view circular polarizers when LC directors form eight domains in the bright state: (a) iso-contrast plot at $\lambda$ = 550 nm; (b) iso- transmittance plot at $\lambda$ = 550 nm; c) iso-contrast plot at $\lambda$ = 450 nm; (d) iso-transmittance plot at $\lambda$ = 450 nm; e) iso-contrast plot at $\lambda$ = 650 nm; (f) iso-transmittance plot at $\lambda$ = 650 nm. Ten-layer anti-reflection film in Figure 7.3 is assumed.

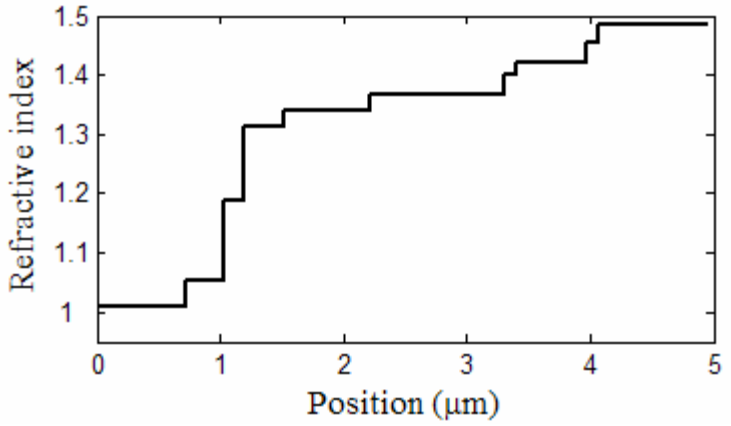


(a)

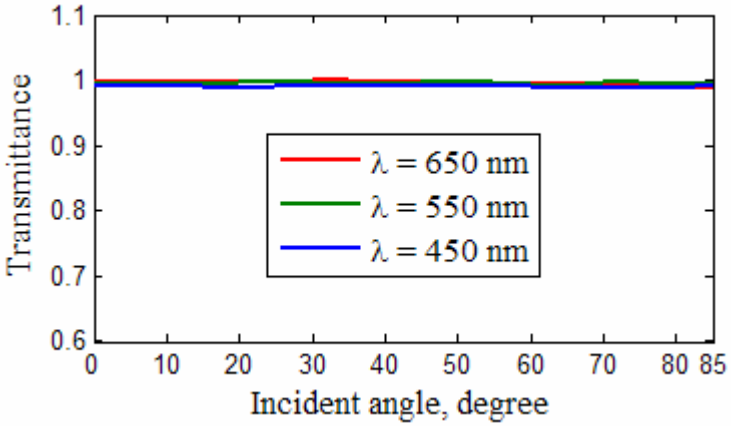


(b)

Figure 7.3: Ten-layer ideal anti-reflection film: (a) refractive indices profile, (b) transmittance.

## 7.2. Design tolerance

Design tolerance is an important concern from manufacturing viewpoint. For the proposed design of a wide-view VA-LCD, we calculate the minimum contrast ratio over the $\pm 85^{o}$ viewing cone if the film parameters of the biaxial films deviate from the optimal values by ±5%. The incident wavelength is 550 nm and the simulation results are plotted in Figure 7.4. First we evaluate the influence of film thickness. The solid line with plus sign markers in Figure 7.4 indicates that a −5% deviation in the first biaxial film thickness reduces the contrast to 400:1. By contrast, the light leakage is quite inert to the errors of the second biaxial film thickness (dashed line with plus sign markers). Next, we study how the NZ factor affects the contrast. As shown by the solid line with triangular markers in Figure 7.4, the NZ factor of the first biaxial film plays a significant role. The contrast ratio decrease to 200:1 with a ±5% deviation. On the other hand, a −5% error in the NZ factor of the second biaxial film decreases the contrast ratio to 300:1 (dashed line with triangular markers). The solid and dashed lines with circle markers in Figure 7.4 illustrate that the contrast ratio is almost invariant when the orientations of both biaxial films vary by ±5%. Thus, from this tolerance analysis we find that the accuracy of the first biaxial film parameters is more critical than that of the second biaxial film and the NZ factors of both biaxial films require a higher accuracy

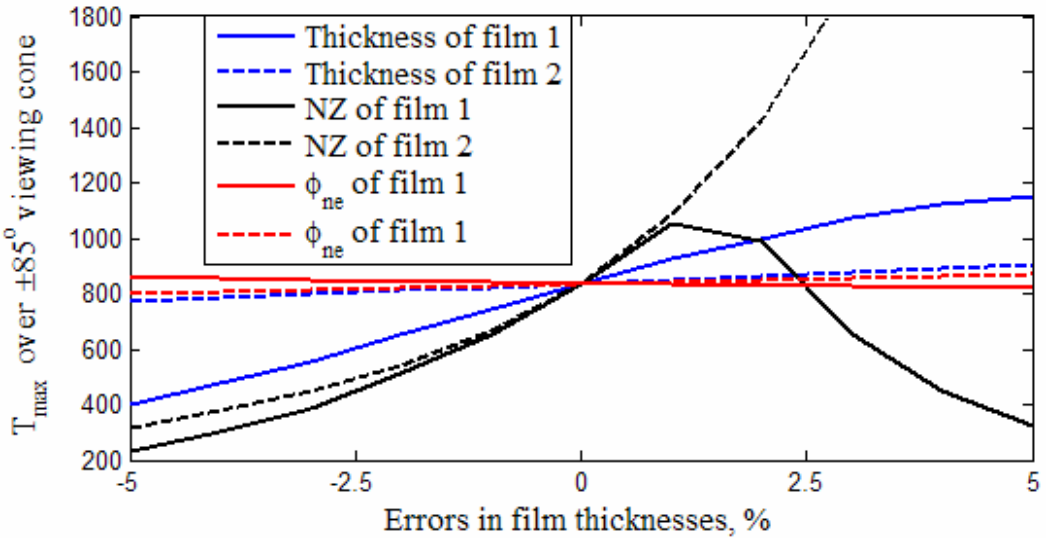


Figure 7.4: Design tolerance of the proposed wide-view VA-LCD. The viewing cone is ±85° and $\lambda$ = 550 nm. Ten-layer anti-reflection film is assumed.

## 7.3. Summary

In this chapter, we demonstrate a wide view VA LCD with both high contrast ratio and high transmittance over the entire visual spectrum. With crossed wide-view circular polarizers, the maximum transmittance of the presented multi-domain VA-LCD is higher than 88% (0.333 out of 0.378) and the contrast ratio is higher than 800:1 for the green light. Over the entire visual spectrum the maximum transmittance is higher than 78% (0.289 out of 0.378) and the contrast ratio remains higher than 110:1. The uniformity of better than 70% in the bright state transmittance is predicted over the ±85° viewing cone if the air-interface surface reflection is suppressed. Furthermore, the configuration of the wide view LCD is simplified by employing the simple configuration wide-view circular polarizer.

# CHAPTER EIGHT: CONCLUSION

In this dissertation, by applying the phase compensation technologies, the polarization states of the light are transferred into the desired states of polarization over a wide range of viewing angles. The dark state light leakages are suppressed and the bright state transmittances are increased. These produce high and uniform transmittance for the liquid crystal displays and ensure high contrast ratio over wide viewing angles.

A wide viewing angle vertical-alignment liquid crystal display (VA-LCD) using crossed linear polarizers is investigated [16]. After analyzing the polarization states inside the uniaxial phase retardation films and the vertical-alignment liquid crystal layer, a design methodology for the wide viewing angle multi-domain VA-LCDs is proposed. With the optimization design, a multi-domain VA-LCD predicts iso-contrast ratio higher than 10,000:1 over the $\pm 85^{o}$ viewing cone.

In addition to high contrast ratio, high and uniform transmittance is also highly desired for the wide viewing angle liquid crystal displays. It was shown that the light efficiency of wide-view LCDs can be improved by the applications of wide-view circular polarizers. Wide viewing angle circular polarizers for both single wavelength and broadband white light are developed using the phase compensation technologies. The produced states of polarization are very close to the ideal circular state of polarization over a wide range of incident angles within the visual spectrum. Therefore, the light leakage from the crossed circular polarizers using the proposed

single-wavelength circular polarizer is less than $2.87\times10^{-4}$ over the ±85° viewing cone at $\lambda$ = 550 nm. Using the proposed broadband wide-view circular polarizer, the light leakage is predicted to be less than $1.7\times10^{-3}$ over the ±85° viewing cone for the visual white light and it is lower than $3.79\times10^{-4}$ at $\lambda$ = 550 nm.

The proposed wide-view circular polarizers guarantee not only high contrast ratio but also high and uniform transmittance over wide viewing angles for wide-view liquid crystal displays. Applying the broadband wide-view circular polarizer to a multi-domain VA-LCD, the maximum transmittance of the presented multi-domain VA-LCD is predicted to be greater than 90% and the contrast ratio is higher than 420:1 for the green light. Over the entire visual spectrum the maximum transmittance is greater than 81% and the contrast ratio remains higher than 115:1. The uniformity of better than 68% in the bright state transmittance is achievable over the ±85° viewing cone if the air-interface surface reflection is suppressed.

To reduce the cost and improve the applicability of the broadband and wide-view circular polarizers, the device configuration of the broadband wide-view circular polarizer is significantly simplified by the application of biaxial compensation films. A broadband wide-view circular polarizer consisting of a linear polarizer and two biaxial phase retardation films is proposed. The produced states of polarization remain close to the ideal circular polarization over a wide range of incident angles within the white light spectrum. The light leakage from the crossed circular polarizers is less than $8.23\times10^{-5}$ over the ±85° viewing cone at the designed wavelength $\lambda$ = 550 nm. Within the 450~650 nm spectral range, this light leakage is kept below $3.92\times10^{-3}$ over the entire ±85° viewing cone.

Applying this simplified broadband and wide viewing angle circular polarizer to a multi-domain VA-LCD, the maximum transmittance is predicted to be higher than 88% and the contrast ratio is higher than 800:1 for the green light. Over the entire visual spectrum the maximum transmittance is higher than 78% and the contrast ratio remains higher than 110:1. The uniformity of better than 70% in the bright state transmittance is predicted over the $\pm 85^{o}$ viewing cone if the air-interface surface reflection is suppressed.

# REFERENCES


1. D. K. Yang and S. T. Wu, *Fundamentals of Liquid Crystal Devices*, (Wiley, New York, 2006).
2. S. Chandrasekhar, F. R. S, *Liquid Crystals*, (Cambridge University Press, 1992).
3. E. Lueder, *Liquid crystal displays: addressing schemes and electro-optical effects*, New York: Wiley, 2001.
4. S. Kim, "AMLCD manufacturing technology," Soc. Inf. Display Seminar Lecture Notes **1**, M-4 (2003).
5. I. Miller, "LCD television," Soc. Inf. Display Seminar Lecture Notes.**1**, M-7 (2004).
6. R. Lu, X. Zhu, S. T. Wu, Q. Hong, and T. X. Wu, "Ultra wide view liquid crystal displays," J. Display Tech. **1**, 3-14 (2005).
7. S. T. Wu, "Design and fabrication of phase-matched compensation films for LCDs," Soc. Inf. Display Tech. Digest **27**, 21 (1996).
8. K. Ohmuro, S. Kataoka, T. Sasaki and Y. Koike, "Development of super-high-image-quality vertical-alignment-mode LCD," Soc. Inf. Display Tech. Digest **28**, 845 (1997).
9. S. T. Wu, "Film compensated homeotropic liquid crystal cell for direct view display," J. Appl. Phys. **76**, 5975 (1994).
10. P. Bos and K. Koehler/Beran, "The π-cell: a fast liquid crystal optical switching device," Mol. Cryst. Liq. Cryst. **113**, 329 (1984).

11. Y. Saitoh, S. Kimura, K. Kusafuka, and H. Shimizu, “Optimum film compensation of viewing angle of contrast in in-plane-switching-mode liquid crystal displays,” Jpn. J. Appl. Phys. **37**, 4822-4828 (1998).
12. T. Ishinabe, T. Miyashiita, and T. Uchida, “Novel wide viewing angle polarizer with high achromaticity,” Soc. Inf. Display Tech. Digest **31**, 1094-1097 (2000).
13. M. Koden, “Wide viewing angle technologies for TFT-LCD,” Sharp Technical Journal **2**, 1 (1999).
14. K. Ohmuro, S. Kataoka, T. Sasaki, and Y. Koike, “Development of super-high-image-quality Vertical-Alignment-Mode LCD,” Soc. Inf. Display Tech. Digest **28**, 845-848 (1997).
15. J. Chen, K. H. Kim, J. J. Jyu, J. H. Souk, J. R. Kelly, and P. J. Bos, “Optimum film compensation modes for TN and VA LCDs,” Soc. Inf. Display Tech. Digest **29**, 315-318 (1998).
16. Q. Hong, T. X. Wu, X. Zhu, R. Lu, and S. T. Wu, “Extraordinary high-contrast and wide-view liquid crystal displays,” Appl. Phys. Lett. **86**, 121107 (2005).
17. S. H. Hong, Y. H. Jeong, H. Y. Kim, H. M. Cho, W. G. Lee, and S. H. Leea, “Electro-optic characteristics of 4-domain vertical alignment nematic liquid crystal display with interdigital electrode,” J. Appl. Phys. **87**, 8259-8263 (2000).
18. A. Takeda, S. Kataoka, T. Sasaki, H. Chida, H. Tsuda, K. Ohmuro, T. Sasabayashi, Y. Koike, and K. Okamoto, “A super-high image quality multi-domain vertical alignment LCD by new rubbing-less technology,” Soc. Inf. Display Tech. Digest **29**, 1077-1080 (1998).

19. Y. Tanaka, Y. Taniguchi, T. Sasaki, A. Takeda, Y. Koibe, and K. Okamoto, ”A new design to improve performance and simplify the manufacturing process of high-quality MVA TFT-LCD panels,” Soc. Inf. Display Tech. Digest **30**, 206-209 (1999).
20. N. Koma, R. Nishikawa, and K. Tarumi, “Development of a simple process to fabricate high-quality TFT-LCDs,” Soc. Inf. Display Tech. Digest **27**, 558-563 (1996).
21. S. H. Lee, S. L. Lee, and H. Y. Kim, “Electro-optic characteristics and switching principle of a nematic liquid crystal cell controlled by fringe-field switching,” Appl. Phys. Lett. **73**, 2881 (1998).
22. S. Kataoka, A. Takeda, H. Tsuda, Y. Koike, H. Inoue, T. Fujikawa, T. Sasabayashi and K. Okamoto, “A new MVA-LCD with jagged shaped pixel electrodes,” Soc. Inf. Display Tech. Digest **37**, 1066-1069 (2001).
23. T. H. Yoon, G. D. Lee, and J. C. Kim, “Nontwist quarter-wave liquid crystal cell for a high-contrast reflective display,” Opt. Lett. **25**, 1547-1549 (2000).
24. Y. Iwamoto, Y. Toko, H. Hiramoto, and Y. Iimura, “Improvement of transmitted light efficiency in SH-LCDs using quarter-wave retardation films,” Soc. Inf. Display Tech. Digest **31**, 902-905 (2000).
25. T. Ishinabe, T. Miyashita and T. Uchida, “Design of a quarter wave plate with wide viewing angle and wide wavelength range for high quality reflective LCDs,” Soc. Inf. Display Tech. Digest **32**, 906-909 (2001).
26. Q. Hong, T. X. Wu, X. Zhu, R. Lu, and S. T. Wu, “Designs of wide-view and broadband circular polarizers,” Opt. Express **13**, 8318-8331 (2005).
27. Q. Hong, T. X. Wu, R. Lu, and S. T. Wu, “A Wide-view circular polarizer consisting of a linear polarizer and two biaxial films,” Opt. Express **13**, 10777-10783 (2005).

28. Q. Hong, T. X. Wu, R. Lu, and S. T. Wu, "A wide-view multi-domain VA-LCD with high transmittance and high contrast," Soc. Inf. Display Tech. Digest **37**, 736-739 (2006).

29. G. Panasyuk and D. W. Allender, "Approximate description of the three dimensional director and electric field in a liquid crystal display at a high voltage," J. Appl. Phys. **87**, 49 (2000).

30. H. J. Yoon, J. H. Lee, M. W. Choi, J. W. Kim, O. Kwon, T. Won, S. H. Yoon, "Comparison of numerical methods for analysis of liquid crystal cell: in-plane switching," Soc. Inf. Display Tech. Digest **34**, 1378-1381 (2003).

31. D. W. Berreman, "Numerical modeling of twisted nematic devices," Phil. Trnas. R. Soc. Lond. A **309**, 203-216 (1983).

32. J. E. Anderson, P. J. Bos, C. Cai, and A. Lien, "3-dimensional modeling of ridge-fringe field LCDs," Soc. Inf. Display Tech. Digest **30**, 628-631 (1999).

33. J. E. Anderson, C. Titus, P. Watson, and P. J. Bos, "Significant speed and stability increases in multi-dimensional director simulations," Soc. Inf. Display Tech. Digest **34**, 906-909 (2003).

34. M. V. K. Chari and S. J. Salon, *Numerical Methods in Electromagnetism*, (Academic Press, San Diego, 2000).

35. W. H. Hayt, Jr. J. A. Buck, *Engineering Electromagnetics*, (McGraw-Hill Higher Education, New York, 2001).

36. D. W. Berreman, "Optics in Stratified and Anisotropic Media: 4 x 4-Matrix Formulation," J. Opt. Soc. Am. **62**, 502 (1972).

37. A. Lien, "A detailed derivation of extended Jones matrix representation for twisted nematic liquid crystal displays," Liquid Crystal, **22**, 171 (1997).

38. A. Lien, “Extended Jones matrix representation for the twisted nematic liquid-crystal display at oblique incidence,” App. Phys. Lett. **57**, 2767 (1990).

39. Y. Huang, T. X. Wu, and S. T. Wu, “Simulations of liquid-crystal Fabry-Perot etalons by an improved 4×4 matrix method,” J. Appl. Phys. **93**, 2490-2495 (2003).

40. I. Moreno, P. Velásquez, C. R. Fernández-Pousa, M. M. Sánchez-López, and F. Mateos, “Jones matrix method for predicting and optimizing the optical modulation properties of a liquid-crystal display,” J. Appl. Phys. **94**, 3697 (2003).

41. S. Huard, *Polarization of Light*, (Wiley, New York, 1997).

42. C. Brosseau, *Fundamentals of Polarized Light: A statistical Optics Approach*, (Wiley, New York, 1998).

43. Q. Hong, T. X. Wu, and S. T. Wu, “Optical wave propagation in a cholesteric liquid crystal using the finite element method,” Liq. Cryst. **30**, 367-375 (2003).

44. R. L. Haupt and S. E. Haupt, *Practical Genetic Algorithms*, (Wiley, Hoboken, 2004).

45. A. Osyczka, *Evolutionary Algorithms for Single and Multicriteria Design Optimization*, (Springer-Verlag, New York, 2002).

46. S. Pancharatnam, “Achromatic combinations of birefringent plates,” Proc. Ind. Acad. Sci. A **41**, 130-144 (1956).

47. S. T. Wu and D. K. Yang, *Reflective Liquid Crystal Displays*, (Wiley, New York, 2001).